Measurement of neutron production from an ^{18}O target for the production of radioactive-ion beams at iThemba LABS

PHUMLANI ZIPHO NGCOBO

A thesis submitted to the University of Cape Town in requirements for the degree of Doctor of Philosophy

Supervisors:

Prof. A. Buffler
Department of Physics,
University of Cate Town, Rondebosch, 7700, Cape Town

Dr. R. A. Bark
Radioactive Ion Beam Project
iThemba LABS PO Box 722, Somerset West, 7129, Cape Town

October 2018

ABSTRACT

iThemba LABS, in the South African Isotope Facility (SAIF) project, proposes to produce radioactive ion beams by the fission of uranium. A natural way to fission uranium is to use high-intensity proton beams from a cyclotron. However, neutron-induced fission gives enhanced production of neutron-rich fission fragments compared to proton-induced fission, thus there is a need to find efficient ways of producing neutrons from protons. Beryllium targets have been suggested, but increasing the proton beam current to achieve higher fission rates could lead to cooling problems. Cooling might be achieved in a natural way by using enriched water as a converter, but ^{16}O is a poor neutron converter compared with ^{9}Be. An alternative would be to use water enriched in ^{18}O. With no data available for ^{18}O above 25 MeV, this necessitated the measurement of neutron yields from the $^{18}O(p,xn)$ reactions between 30 and 66 MeV. Quasi-monoenergetic neutron spectra were therefore measured at proton energies of 66; 54; 42 and 30 MeV on a 2.03 mm thick $H_2{}^{18}O$ water target using the time of flight (ToF) technique at 0˚ and 16˚. Neutron energy spectra from a ^{7}Li (2.5 ± 0.5 mm thick) target were also measured at the same energies to validate the $H_2{}^{18}O$ measurements. The spectra deduced at these energies were used to simulate the neutron fluence spectra from a stopping-length $H_2{}^{18}O$ target and were compared with the measured neutron fluence spectra from a thick target of 40.0 ± 0.1 mm at 0˚ and 16˚, using a proton beam of 62 MeV.
The neutron differential cross sections, $d\sigma(E)/d\Omega$ for the $^{18}O(p,n)$ reactions at 66; 54; 42 and 30 MeV were derived and compared to those of $^{7}Li(p,n)$ and $^{9}Be(p,n)$. The cross sections of ^{7}Li and ^{9}Be are higher than those of ^{18}O between 20 MeV and 50 MeV at 0°. At above 60 MeV, the ^{7}Li target produces double the amount of neutrons produced by ^{18}O and ^{9}Be targets, but importantly ^{18}O produce neutrons more than ^{9}Be. The $^{18}O(p,xn)$ neutron cross sections ($d^2\sigma(E)/d\Omega dE$ in mb/MeV/sr) from the thick stopping-length target (40 mm) were compared to the corresponding cross sections of ^{9}Be thick stopping-length target (24.1mm). Conclusively, on average, the ^{18}O neutrons cross sections are half those of ^{9}Be.

DECLARATION

I, the undersigned, hereby declare that the work contained in this thesis is my own original work and that I have not previously in its entirety or in part submitted it at any university for a degree.

11/05/2018

Signed by candidate

…… ……..……

Phumlani Zipho Ngcobo Date

ACKNOWLEDGEMENTS

TRUE NOBILITY is not being better than others but being better than you used to be. It has been always about finding my ‘true‟ self and again this work takes me closer to that. I acknowledge the divine Creator, the source of all life, for my existence.

To Dr Robert Bark, I dedicate my research life to you, having supervised me for my masters and this current doctoral work.

I thank Professor Andy Buffler for all the efforts to get the core of this experimental done with distinction. The help I got from Mr Dieter Gedurd and the rest of the iThemba LABS Neutron Group.

Thanks to all Masters, PhD students, Postdoctorals based at iThemba LABS for all the support and giving me courage. I am grateful to the staff of iThemba LABS that helped with administrative side of things. You have all made it possible.

I thank the Ngcobo family - eSiphofini, amaQadi onke, abogogo nabomkhulu, my mother Desma Delisiwe and uncle Fakazi Nkos’phile, for the wisdom and words of inspiration. Gratitudes to my kids, Mfundo and Zolunga. Thanks to my fiancé Thuthukile Khumalo and our future kids, for the support on the last days of this work.

To all my friends I cannot count here, for believing in me and the words of encouragement through the darkest times of this work. Most of you called me a “Dr” long before.

To the Department of Science & Technology and National Research Foundation, receive my gratitudes for funding this work and affording me an opportunity to live a comfortable life as a student in the mother city, Cape Town.

To the anonymous examiners who contributed and improved this thesis, I am truly grateful.

DEDICATION

To the late Amos Mphiwa Xulu and his family, for being a symbol of what education can do to a person. I was born in the same village called iMpaphala with the Xulu family and attended the same UCCSA church. On his retirement, Mr Xulu having served the KZN Dept of Education as a Circuit Inspector, he volunteered to teach at my high school. Sadly, when I was in matric, he passed on in December 1996, before my matric results were published. This PhD work is yours mkhulu. *May your soul rest in peace*.

CONTENTS

CHAPTER 4: DATA ANALYSIS

CHAPTER 5: RESULTS & DISCUSSIONS

LIST OF FIGURES

LIST OF TABLES

CHAPTER 1: INTRODUCTION

1.1 iThemba LABS facility and the South African Isotope Facility (SAIF) project

The iThemba Laboratory for Accelerator--based Sciences (LABS) is a national research facility situated in the Western Cape and Gauteng provinces in South Africa. It supports research in nuclear and material sciences, and research in radiotherapy based on neutron and proton beams, and supplies hospitals in South Africa and abroad with radioisotopes for medical diagnostics. The k = 200 separated-sector cyclotron (SSC) accelerator is central to the operations of this multidisciplinary facility.

There is a growing appetite within nuclear physics research to study neutron-rich nuclides, to further the understanding of nuclear forces and the origin of the elements. These nuclides cannot be adequately studied using stable beams, therefore, iThemba LABS proposes to produce neutron-rich radioactive-ion beams (RIBs) using the Isotope Separation Online (ISOL) method [Ba12].

The proposal [Ba12] for iThemba LABS was that a commercial 70 MeV negative-ion cyclotron, allowing simultaneous extraction of two H^- beams, be installed both for the production of radioactive-ion beams and for the simultaneous production of medical isotopes. A phased development of the RIB facility would see two phases implemented progressively [Ba12]. Phase 1 would realise a development of a 70 MeV negative-ion cyclotron with two radioisotope production stations. Phase 2 would add two RIB production stations for nuclear and materials research, see Figure 1. Note the location of the cyclotron, beamlines and the two RIB target stations.

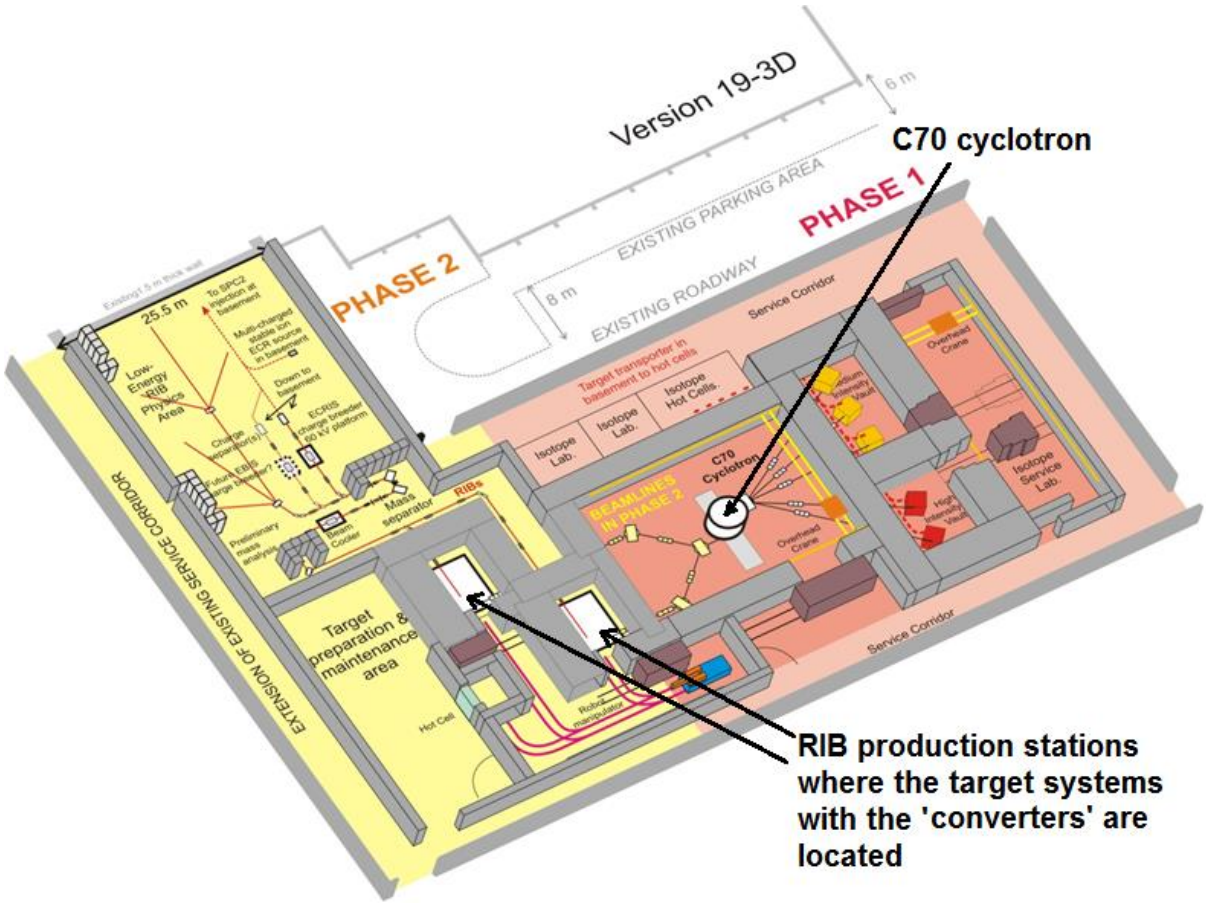

Figure 1: *Schematic of the iThemba LABS Radioactive Ion Beams (RIB) Project development [Ba12].*

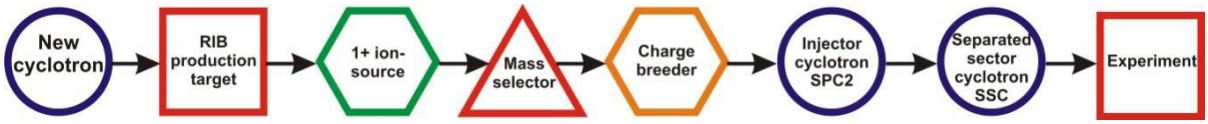

Figure 2: *The ISOL method and the stages in the production of RIBs at iThemba LABS [Ba12].*

Figure 2 shows the stages of the RIB production being considered for iThemba LABS. The ISOL technique begins with the production of neutron-rich radioactive isotopes in a target, in this case, uranium-238. Normally the target is thick enough to stop the reaction products so that isotopes of interest can be collected and then effused, by heating of the target, into an ion-source for ionisation [Du06]. These isotopes would then be mass-analysed to select the nuclei of interest (forming a beam), which may either be transported to low-energy experimental areas or re-accelerated to the required energy.

There is an existing solid-pole injector cyclotron (SPC2) used to provide heavy ions and polarised protons for injection into the SSC. Therefore, for post-acceleration, the radioactive ion beam could be directed through SPC2. Prior to injection, the RIB ions must have their charge-state increased with a possible use of a charge-breeder. The final charge-state of ions will determine the beam energy in the SSC [Ba12].

1.2 Production of neutron-rich RIBs at iThemba LABS

iThemba LABS proposes to manufacture neutron-rich beams by fissioning uranium -238. The nuclear species to be produced are indicated in Figure 3. These are of considerable interest to the nuclear physics community as these unstable beams have not been studied in as much detail as stable nuclei. Studying these neutron-rich nuclei will contribute to the understanding of the nuclear force and the origins of elements that make up the universe.

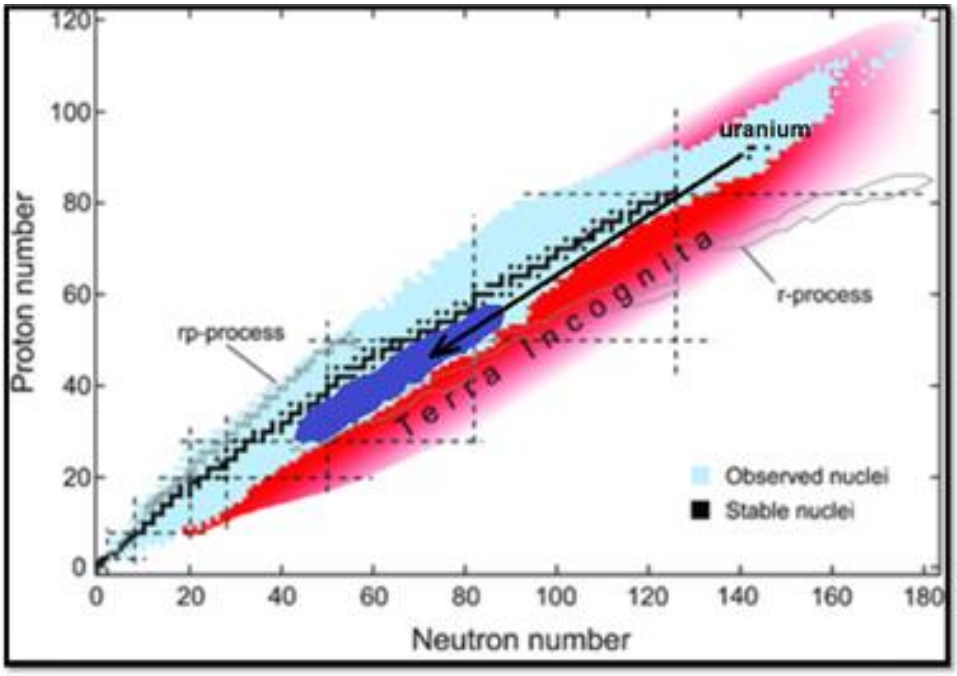

Figure 3: *Nuclear chart showing the region of interest of nuclei (dark blue) to be produced at iThemba LABS using radioactive ion beams.*

The interest is to enhance the production of neutron-rich fission fragments. It is well known that neutron-induced fission results in enhanced production of neutron-rich fission fragments [Ho08]. Monte Carlo simulations comparing the proton and neutron-induced fission yields on uranium carbide were done for studies relating to the Holifield RIB Facility at Oak Ridge National Laboratory [Ho08].

Figure 4 shows that the neutron-induced production of tin isotopes is enhanced for *A*>128 by more than three orders of magnitude compared to the proton-induced direct reaction (p, f).

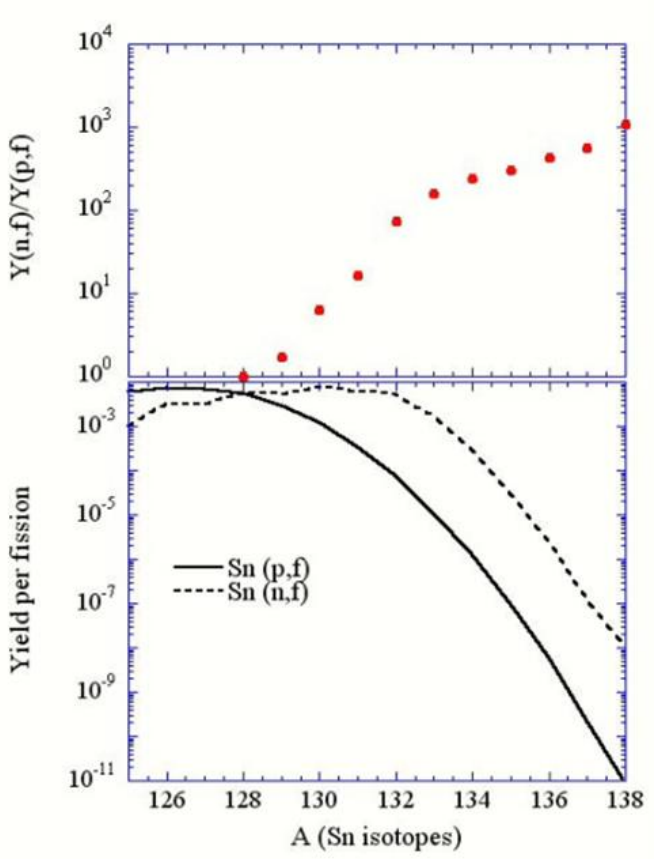

Figure 4: *Yields of Sn isotopes from proton-induced fission by 70 MeV protons (solid line), compared to the yields of Sn isotopes yields from neutron-induced fission (dashed line). The upper plot gives ratios of the yields [Ho08].*

Given the proposed proton accelerator for the RIB project, neutron-induced fission would require a method to "convert" protons into neutrons so that it is neutrons and not protons that probe the uranium carbide (UC_x) target. The symbol UC_x is used to refer to uranium carbide. This conversion of protons to neutrons is known as the "converter" method as opposed to the direct reaction method [Ba12].

The SPIRAL II project at GANIL, France, which also proposes the ISOL method for RIB production is expected to use the "converter" method in order to generate about 10^{14} fissions/s, using an intense deuteron beam from a linear accelerator (LINAC). Figure 5 shows the layout of SPIRAL II, including the carbon converter together with the UC_x target system, to be located in the RIB production station. In a similar fashion, the process of selecting and studying neutron-rich nuclei would follow the stages of the ISOL technique as explained earlier.

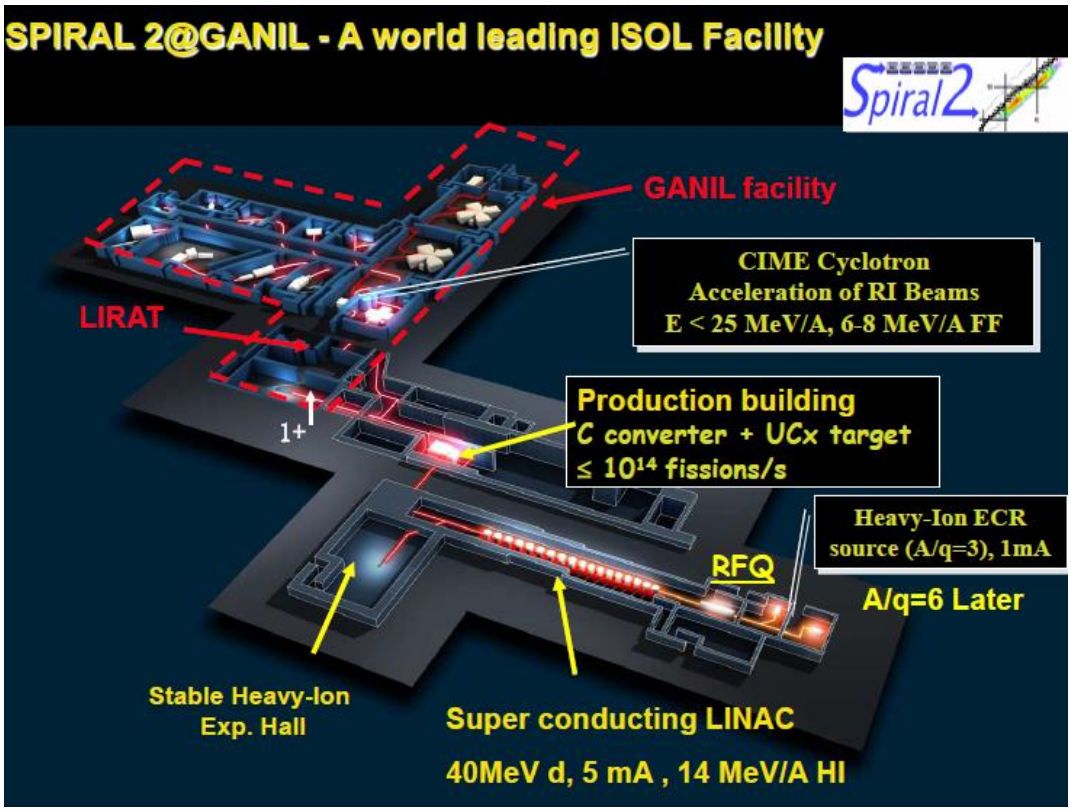

Figure 5: *View of the SPIRAL2 project at the ISOL facility at GANIL for the production of exotic species in the mass range from A = 60 to A = 140 [Ke08].*

1.3 Converter target to optimise iThemba LABS neutron-rich isotopes

The so-called “converter” method is the one in which a high-power primary beam is dumped on to a well-cooled neutron production target. The resulting neutrons, having a power deposition much smaller than that of the primary beam, then travel through a secondary target of uranium carbide (UC_x) material. The radioactive-ion production mechanism is neutron-induced fission (n,f), and at iThemba LABS the neutrons would be produced in (p,xn) reactions in the converter target. The main advantages of this method are the higher primary beam power that can be used, and perhaps more importantly, the higher yield of very neutron-rich fission fragments [Ho08].

In the case of iThemba LABS, for the proton-to-neutron “converter” method to achieve a fission rate comparable to international standards, the intensity of neutrons produced should be greater than 10^{13} neutrons/second [Ba12]. To use neutrons for fission at iThemba LABS, the problem becomes one of finding the most efficient way of producing neutrons and intercepting them in the uranium target. This project will explore the possibility and effectiveness of proton induced reactions on ^{18}O, in the form of water, as a converter target to produce neutrons.

This project thus aims to determine:

a) whether ^{18}O is suitable for use as a converter for proton beams, and
b) the energy and angular distributions of the emitted neutrons from $^{18}O(p,xn)$ reaction.

1.4 Finding a suitable stable nucleus for proton-to-neutron yields

Ridikas and Mittig [Ri98] showed that when bombarding target nuclei with protons, the neutron yields are similar for most nuclei but more favourable for very light (beryllium) and very heavy (tantalum to uranium) nuclei [Ri98]. With reference to the curves in Figure 6, it is noteworthy that for light nuclei there is a higher neutron yield when using deuterons rather than protons, but iThemba LABS is acquiring a proton accelerator for simultaneous production of radionuclides for medical purposes, therefore the performance of deuterons is not considered. According to the measurements at GANIL, ^{9}Be performs with the highest neutron yields in the light nuclei category, with about 0.1 neutrons produced per proton at 80 MeV [Ho08]. Over the years, using the reaction $^{9}Be(p,n)^{9}B$ for neutron production for various applications has become common, see for an example [Jo92], [Mo10], [Lo77]. High energy intense neutrons may be produced depending on the energy of the incoming proton beam and beryllium thickness. Neutron therapy at iThemba LABS uses a beryllium target with thickness optimised for the production of highly intense neutrons from proton beams [Jo92].

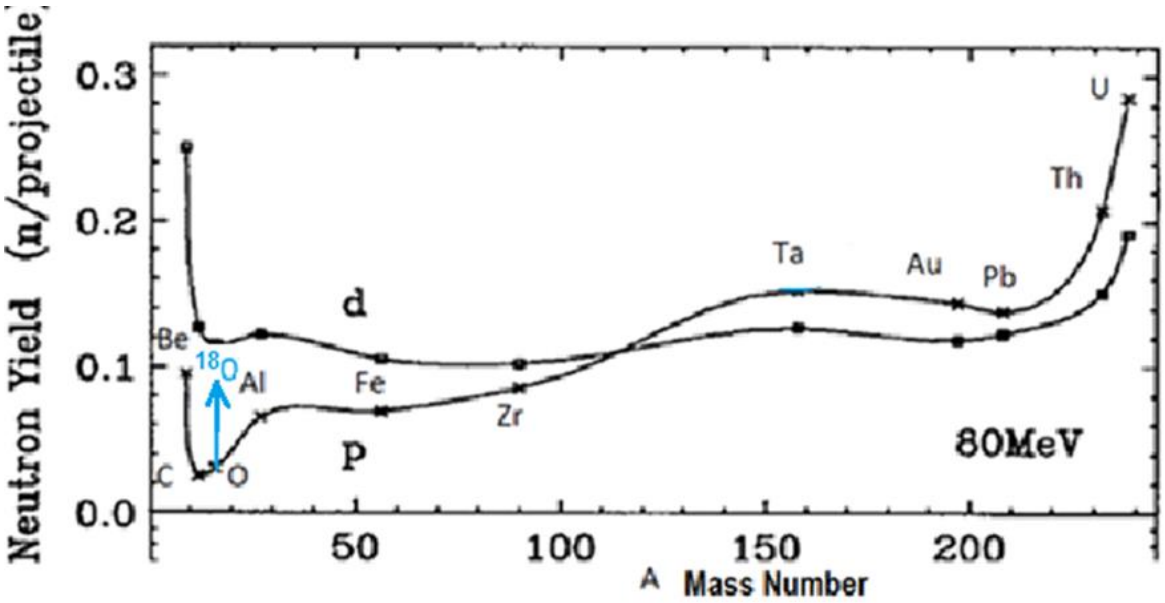

Figure 6: *The neutron yields induced by 80 MeV protons (p) are compared to 80 MeV deutrons (d) for stopping length targets. Results compiled by Ridikas & Mittig at GANIL [Ri98]. The arrow (blue) shows the predicted performance of ^{18}O compared to ^{16}O according to the ALICE/ASH code.*

1.5 Fast neutrons required for ^{238}U fission

In order to produce high yields of the neutron-rich isotopes, the aim of the RIB project at iThemba LABS is to fission natural uranium, essentially ^{238}U, rather than ^{235}U as in a reactor. Figure 7 shows that ^{238}U(n,f) cross sections (CM frame) are significant above 1 MeV [Yo06], [You06]. ^{238}U(n,f) cross sections steadily increase and reach maximum 1.7 barns at about 50 MeV and decrease to about 1.5 barns at 70 MeV [To14].

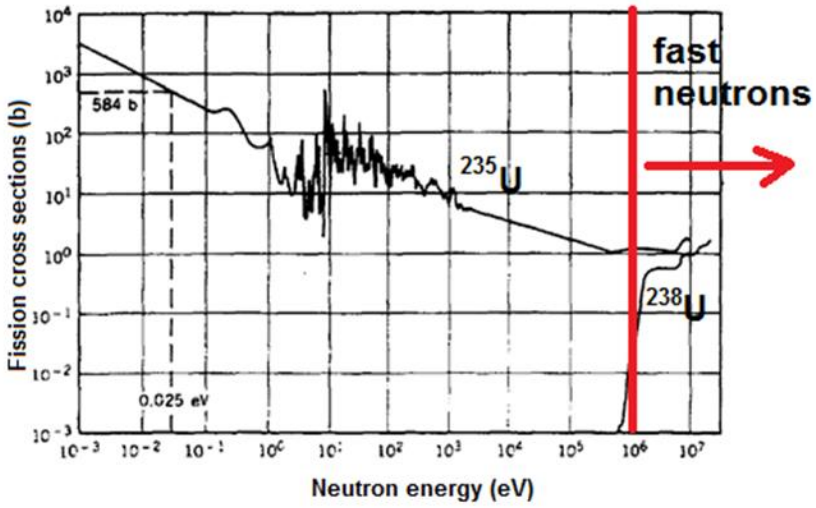

Figure 7: *Cross sections (CM frame) for neutron-induced fission of ^{238}U [Yo06], [You06].*

For this reason, light nuclei are preferred over heavy nuclei which produce high neutron yields at lower energies. This phenomenon is illustrated in Figure 8 which shows that beryllium has higher neutron yield than uranium in the high energy region above 10 MeV.

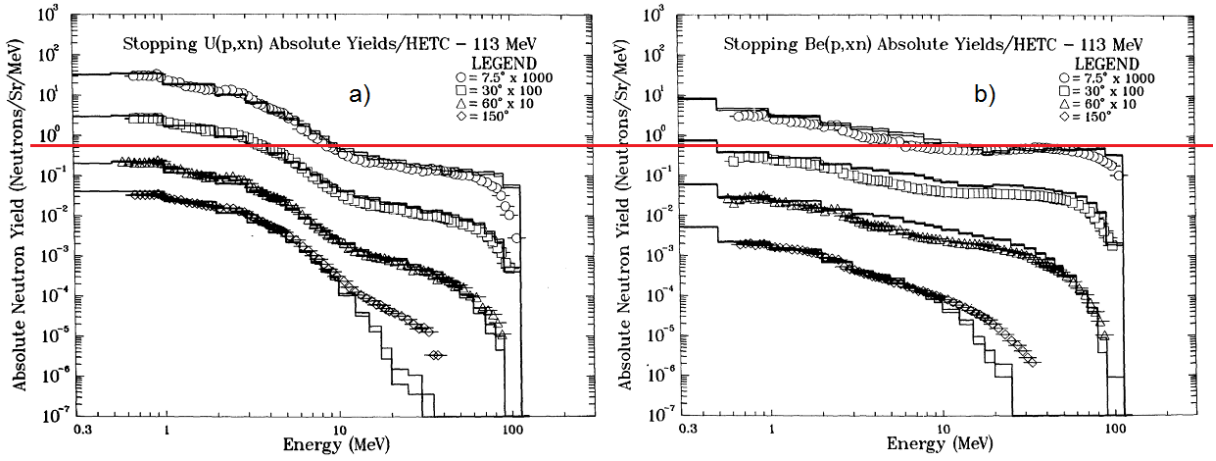

Figure 8: *Absolute neutron yields measured for stopping length targets at a proton energy of 113 MeV for a) uranium, and b) beryllium. The solid lines are calculations using the High Energy Transport Code (HETC) [Me89]. The red line illustrates that beryllium produces more high energy neutrons compared to uranium.*

1.6 Properties of neutrons favour ^{9}Be but have challenges in practical applications

Beryllium is an ideal target to produce neutrons with the desired properties through the ^{9}Be(p,xn) reaction. These neutrons are intense and of high energy [Lo77]. However Be suffers some drawbacks, for example, its thermal properties, such as its melting point and thermal conductivity, make it physically difficult for the envisaged applications using high beam current, which means high power deposition into the converter, leading to heating challenges [Ba12]. Beryllium is also toxic and thus poses a safety threat when working with. The use of $H_2{}^{18}O$-water is also of interest because cooling might be achieved in a natural way, by for example using water as a converter target as water can be circulated to facilitate cooling as opposed to solid targets like $Al^{18}O_3$ and $Si^{18}O_2$. Oxygen-16 is, unfortunately, a poor converter (see Figure 6), but it could be possible to use enriched water ($H_2{}^{18}O$, 97% enrichment in ^{18}O) for the RIB converter target. Yet another possibility is to use $D_2{}^{18}O$.

1.7 Research aim and objectives

Preliminary calculations of neutron production from ^{16}O and ^{18}O using proton energies between 20 MeV and 70 MeV were undertaken using the ALICE/ASH code. The choice of these energies is because the planned cyclotron will produce 66 MeV protons to bombard a target that contains ^{18}O, therefore the aim is to understand the spectrum of neutrons produced. The ALICE/ASH code evolved from the ALICE code which was originally developed by Blann [Bl82] to calculate the interaction of nucleons and nuclei with target nuclei at energies up 300 MeV [Br06]. The code now has models that contain many nuclear reaction mechanisms like pre-compound nucleon emission, fast gamma-ray emission; equilibrium particle emission as well as the fission process.

The results of neutron emission calculations from oxygen isotopes are shown in Figures 9 and 10. Oxygen-18, through the (p,n) and (p,2n) reactions, results in yields of neutrons higher than those of ^{16}O [Br06].

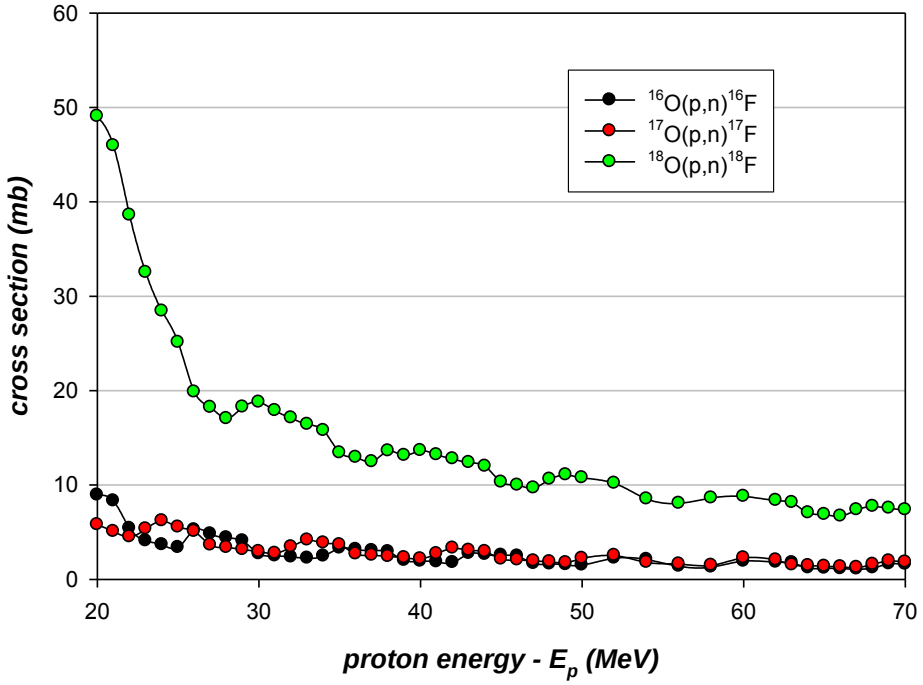

Figure 9: *The neutron production (p,n) cross sections (CM frame) of the three oxygen isotopes calculated using ALICE/ASH code are compared for proton energies between 20 MeV and 70 MeV.*

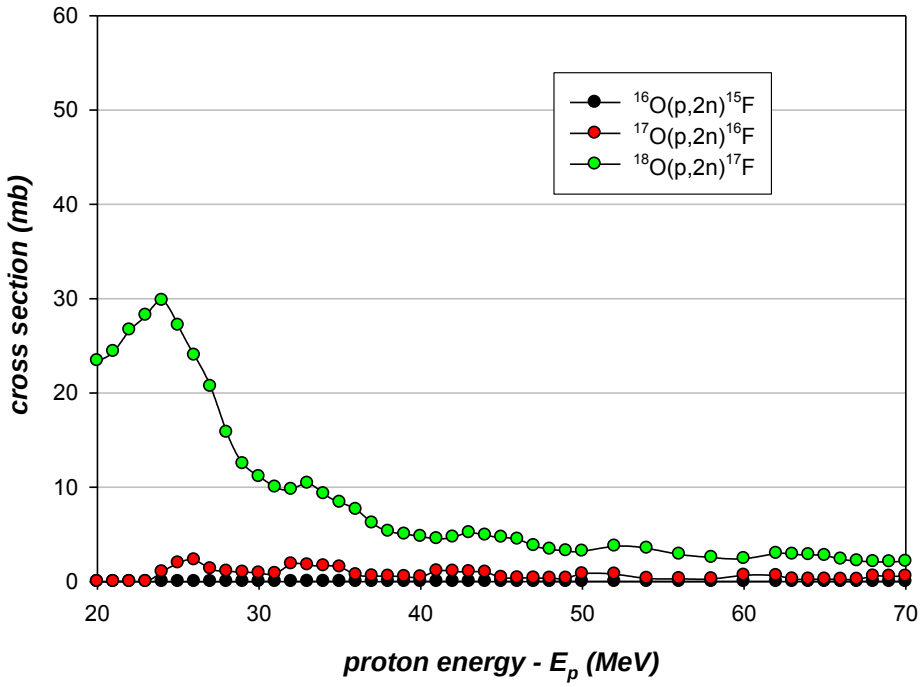

Figure 10: *The neutron production (p,2n) cross sections (CM frame) for the three oxygen isotopes calculated using ALICE/ASH code are compared for proton energies between 20 MeV and 70 MeV.*

From Figure 10, the $^{18}O(p,n)^{18}F$ reaction cross sections simulated with ALICE/ASH code show a decrease from about 20 millibarns at 30 MeV to just above 5 millibarns at 70 MeV.

The ^{18}O (p,2n) cross sections decrease from about 10 millibarns at 30 MeV to about 2.5 millibarns at 70 MeV.

The summed, neutron weighted, neutron production cross sections, shown in Figure 11, suggest that ^{18}O could produce as much as five times as many neutrons as ^{16}O (0.03 neutrons/proton) suggesting that ^{18}O (5 x 0.03 ~ 0.15 neutrons/proton) could be as good as ^{9}Be (~0.1 neutrons/proton) when used as a converter [Br06], [Ri98].

Therefore, the research objective is to measure, experimentally, the actual energy spectrum and angular distributions of the emitted neutrons from ^{18}O(p,xn) reactions in comparison to those from ^{7}Li(p,xn) and ^{9}Be(p,xn) reactions. This will determine if in practice we can design a secondary uranium target to intercept these neutrons and produce a higher yield of neutron-rich isotopes than from a direct reaction of protons on uranium.

The next section will look into the means of using Monte Carlo codes to test the suitability of ^{18}O-water as a target. We look into their reliability, accuracy and thus the necessity for an experimental measurement.

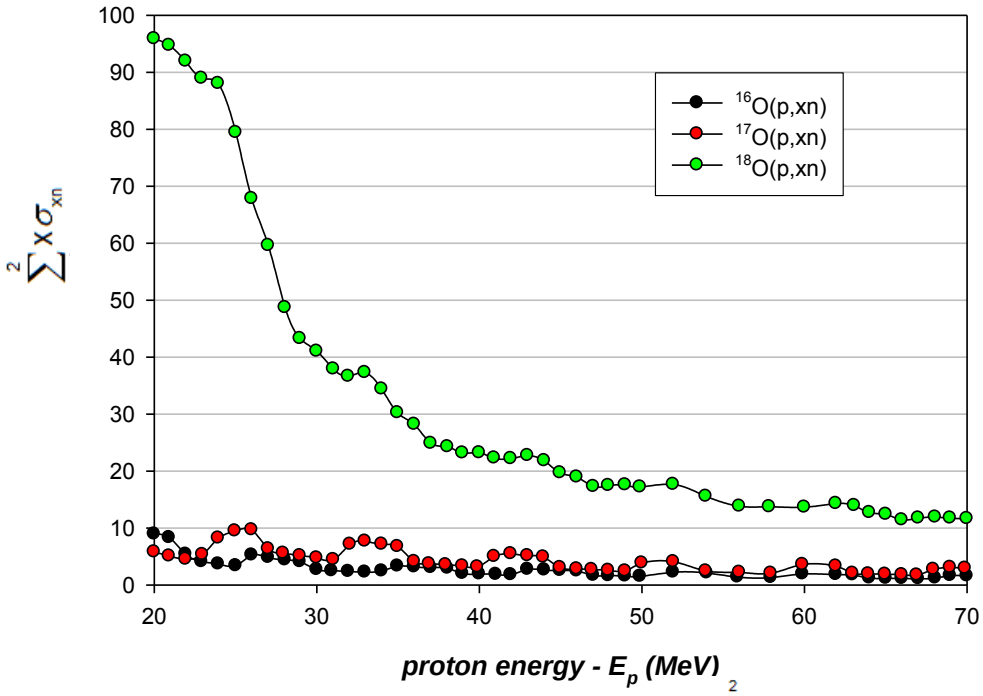

Figure 11: *The total neutron production cross sections ($\sum_{x=1}^{2} x\sigma_{xn}$), in CM frame, for the three oxygen isotopes are compared for proton energies between 20 MeV and 70 MeV.*

1.8 The comparison of MCNPX 2.6.0 and FLUKA2011.2b code calculation to the experimental data.

Another approach to estimating the suitability of a target/projectile combination is to use Monte Carlo Codes such as MCNPX (for Monte Carlo Neutral Particle eXtended) [Pe08] or FLUKA (for FLUktuierende KAskade) [Fe05]. With the MCNPX 2.6.0 code, source term specification is much simpler, as the user simply models the primary beam of incident, monoenergetic, mono-directional protons. The MCNPX code uses cross section tables and nuclear models that contain (p,nX) and (p,γX) cross sections, i.e. the cross sections for nuclear reactions with protons in the entrance channel and neutrons and ionising photons in the exit channel. That is, the production of neutrons and ionising photons are generated by the code, using information in cross section libraries and nuclear reaction models. There are available benchmark validations that have been done before. MCNPX is appropriate for high-energy sources which we will be investigating, and for their activities and related radiations they produce. It is regularly updated, so its cross sections and other physics properties are updated in the built-in data cards and its accuracy is improved. The structure of the MCNPX input file is provided in more detail in the MCNPX manual [Pe08].

FLUKA 2011.2b is the code for simulations of particle transport of about 60 different particle types and their interactions with matter. The code was designed to cater for a range of applications from low energies of the order of 100 eV up to very high energies of the order of TeV. FLUKA undergoes a continuous improvement of the built-in physical models by validating it with evaluated experimental data. Therefore FLUKA is capable of simulating, with an acceptable uncertainty, the interaction and transportation of particles of interest in this work, since we are transporting protons and neutrons in the intermediate energies between 10 and 66 MeV. More in-depth information on nuclear models and its capabilities are available in the FLUKA manual [Fe05]. Such codes have the advantage of being able to include the target geometry, thereby accounting for factors such as energy loss of the beam in the target and attenuation of neutrons in the target. Furthermore, the codes also account for other reaction processes such as those due to secondary reactions.

However, such codes have their limitations. MCNPX uses libraries which do not include data for ^{18}O, for example Figure 12 illustrates a large discrepancy in neutron yield for protons on Li, between MCNPX, FLUKA and the experiment [Am77]. Appendix 4 shows the MCNPX input file that were tallied and has the user input details. The Cell and Surface cards define the geometry and material composition of the target, the SDEF card defines the proton beam, the Physics card defines the physics selected to transport particles of interest. The Tally card and NPS defines the proton beam current and the number of source protons transported.

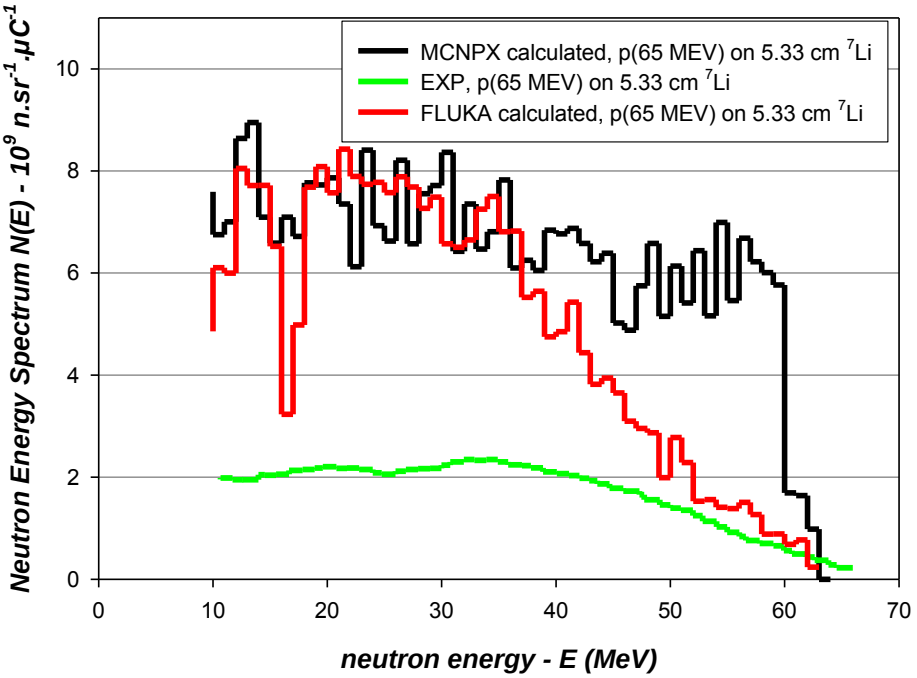

Figure 12: *The neutron energy spectra of 65 MeV protons on 5.33 cm thick ^{7}Li at 0˚ calculated using MCNPX and FLUKA compared to Amols' experimental neutron energy spectra of 65 MeV protons on 5.33 cm thick ^{7}Li at 0˚ [Am77].*

Hence there is a need to measure the neutron yields from a ^{18}O-water target.

1.9 Thesis Outline

The aim of this work is to measure neutron energy spectra at 0° and 16° produced by the bombardment of thin targets of $H_2{}^{18}O$ with proton beams of energies at 66, 54, 42 and 30 MeV respectively. Therefore, this thesis begins with Chapter 1 which give details of the background of the production of neutron-rich isotopes around the world and iThemba LABS in particular. Chapter 1 also outlines the research aims and objectives, which is the production of neutrons on an $H_2{}^{18}O$ thick target if the proton beam energy of 66 MeV is used.

Also, to measure the neutron energy spectra from a stopping length thickness for 62 MeV proton beam at 0° and 16°. Chapter 1 also discusses codes used to validate experimental work. In Chapter 2, the neutron facility at iThemba LABS that was used for this work is discussed. Chapter 3 is the experimental procedure from the experimental setup, data collection through to data reduction. Chapter 4 is data analysis, which includes data validation and comparison of the preliminary results to the similar previous work. Chapter 5 presents all the results measured in this work and discusses them. The neutron spectra produced from thin targets of $H_2{}^{18}O$ are presented and compared to well-known fast neutron producers like ^{7}Li and ^{9}Be. This work also benchmarks ^{18}O as a neutron "converter" by comparing experimental neutron production yields from thick targets of $H_2{}^{18}O$ to that of ^{9}Be. Chapter 6 draws into the conclusion about the work, evaluates results and makes appropriate recommendations within the context of whether ^{18}O, bombarded by protons, is a high neutron flux producer.

CHAPTER 2: FAST NEUTRON FACILITY AT iTHEMBA LABS

The present measurements were carried out using the existing fast neutron beam facility at iThemba LABS. Therefore, in this section an overview of the laboratory, the neutron facility and operation is provided. The specifics of the current experiment are described in Chapter 3.

2.1 The layout of major facilities at iThemba LABS.

Figure 13 illustrates how the proton beam is delivered from the SSC, at energies between 30 MeV and 200 MeV, to the four experimental facilities shown in the diagram. These facilities are the following:

i) The (K600) spectrometer is used for the investigation of nuclear structure as well as various reaction mechanism studies. Amongst others, it allows measurements of inelastic proton or alpha scattering as well as transfer reactions such as the (p,t) reaction, at very small angles, including zero degrees.

ii) The F-line is where an array of HpGe ɣ-ray detectors is situated. This array is called AFRODITE (AFRican Omnipurpose Detector for Innovative Techniques and Experiments) and is comprised of up to 9 “clover” detectors. It is where experiments involving ɣ-ray spectroscopy and nuclear structure studies are conducted.

iii) The A-line is where a 1.5 m diameter scattering chamber is situated. It is used for high precision measurements of angular distribution of charged particles emitted in different nuclear reactions.

iv) The fast-neutron facility is used, typically, to produce quasi-monoenergetic and continuous distribution neutron beams from reactions such as ^{7}Li(p,xn); ^{9}Be(p,xn) and ^{nat}C(p,xn) for physics, metrology and other applications,.

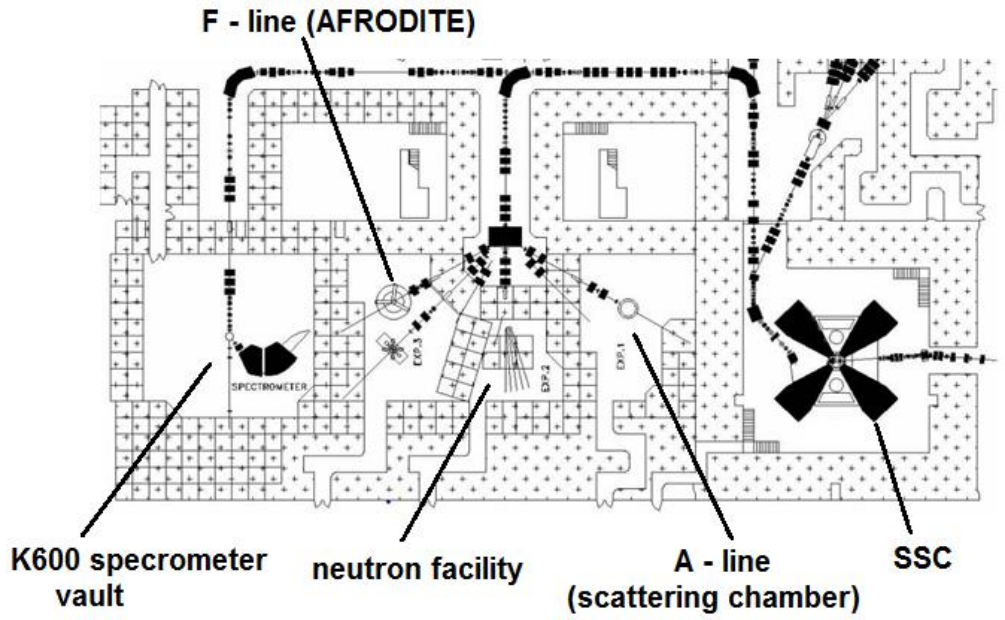

Figure 13: *Layout of beamlines to the four major experimental facilities at iThemba LABS.*

2.2 Neutron facility at iThemba LABS

The fast neutron beam facility at iThemba LABS was used for this work. Figure 14 shows details of the layout of the facility. A pulsed proton beam from the SSC is transported to the target chamber where neutrons are produced. The target chamber is equipped with the target ladder where targets are positioned, as described in Chapter 3. The neutrons produced are shaped by square collimators of 10 cm x 10 cm to form neutron beams at angles of 0°, 4°, 8°, 12° and 16. Figure 14 shows NE213 detectors placed at 0° and 16°, and an NE102 detector at 0° in the experiment area. A NE102 scintillator is used to monitor the neutron rate and thus the beam stability [Mo10].

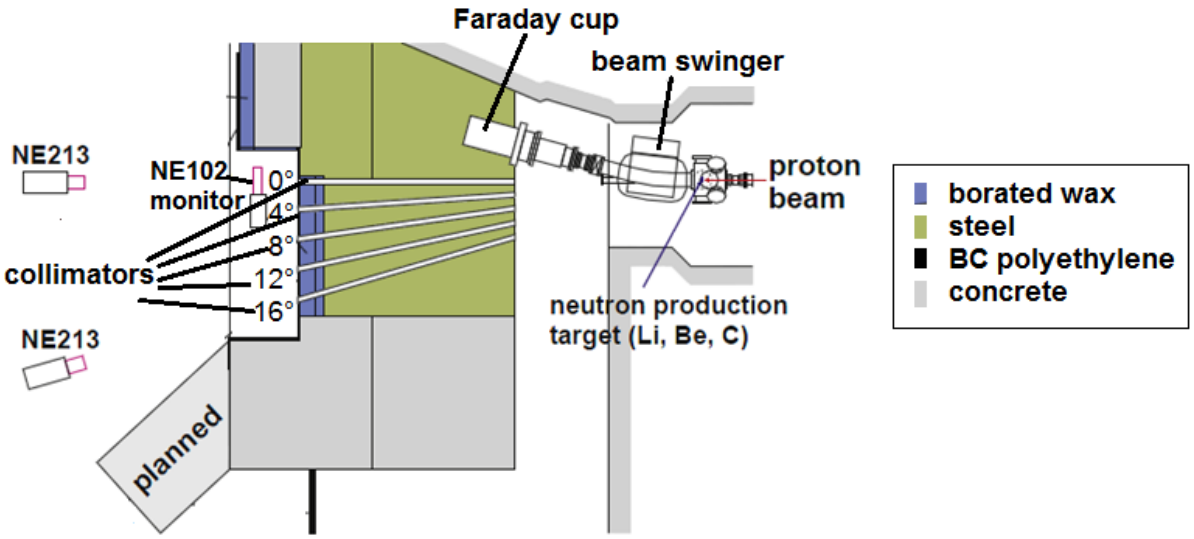

Figure 14: *Schematic diagram of the iThemba LABS neutron facility showing the layout of the detector positions with respect to the target. It shows the collimators at 0°, 4°, 8°, 12° and 16° and the shielding, making this facility suitable for fast neutron measurements.*

Behind the target chamber is a beam swinger (magnetic dipole) that drives the proton beam towards the beam dump for the safe stopping of the beam, and for beam current monitoring.

2.2.1 The cyclotron beam

The SSC is capable of delivering a pulsed proton beam with beam energies between 30 and 200 MeV. The frequency of the beam bunches depends on the cyclotron Radio Frequency (RF), e.g. for 66 MeV, the SSC delivers proton beam bunches at 16.374 MHz. It is possible to reduce this frequency in a limited way with a pulse-selector before injection into the SSC. A 1:5 pulse selection reduces the beam frequency to 3.275 MHz and beam bunches are separated by 305.37 ns.

2.2.2 Target chamber, beam swinger and current integration

The target chamber houses the target holder (target ladder), see Figure 16, with four target spaces. There are two standard spaces occupied by a ruby (used for beam focusing) and an empty frame which is necessary to confirm that no beam halo is striking the target frame.

The standard ruby (a quartz viewer) is used for aligning the beam, especially at low currents [No11]. This ruby target has a small hole in the centre which allows protons to pass through. It is viewed remotely from the SSC control room with a camera to view scintillations caused by the proton beam on the ruby to guide the focusing of the beam to the centre of the target.

The empty frame is an empty circular slot of 20 mm diameter which is used for a “target out run” to observe the background spectrum. The proton beam width is adjusted such that the halo of the beam does not intercept the target holder, so as to produce a clean spectrum. Therefore, during a “target out run”, a well-focused beam should produce a background spectrum with nearly no counts as protons go through without activating any components. The time-of-flight spectrum is confirmed to be clean if there are nearly no counts between the neutron peak and the prompt γ-ray peak (see section 3.1.2).

The third space is reserved for a lithium target which is typically used to produce neutrons. The reaction of ^{7}Li(p,xn) is widely used as a source of neutrons in various applications in basic nuclear physics research; for medical programmes as well as technological applications [Mo10], [Lo77]. Lithium as a source of neutrons is thus well-studied, hence it is used as a reference in this work.

A fourth space is available on the ladder. For this work, it accommodated the $H_2{}^{18}O$ targets.

When thin targets are used, by definition they do not stop protons and so these protons and other stray protons scattering from beamline components, are deflected away by the bending magnet (beam swinger) towards the beam dump, where the beam current is measured and integrated using a Faraday cup [No11]. From the current integration, the total charge of the proton beam is measured. The use of the Faraday cup for beam current measurement depends on other parameters that may change over time due to perturbations that arise from the beamline and target assembly components. Beam current fluctuations, spectral distributions and time structure of the beam are monitored by continuously observing the neutron flux using the NE102 monitor detector.

2.2.3 Collimators for measurements at 0° and 16°

The target area is closed off and shielded from the measurement area. The neutrons are collimated into a beam using the square steel collimators at 0˚ and 16˚. The beam formation ensures that neutrons reach the detector through its front window as it is positioned coaxially to the neutron beam as shown in Figure 14. To ensure a clean neutron beam with no charged particles from the target chamber, an absorber material (a graphite block) is placed in the entrance of the collimators [Ha11]. The collimators at 4°, 8° and 12° are presently closed off and therefore measurements were only made at angles 0° and 16°.

2.2.4 Absorption of background neutrons

In the measurement area, background neutrons must be addressed. According to Mosconi *et al.* [Mo10] the source of background neutrons are those scattered off the walls in the passage between the target vault and detection area. To address these scattered neutrons, Adam *et al*. [Ad10] studied the most suitable configuration to absorb and reduce these neutrons. Recommendations from this study, such as using borated polyethylene in the doors separating the target area from the neutron measurement area have since been implemented in the structural shielding.

2.3 Transforming the ToF spectrum into an energy spectrum

A pulsed beam makes possible the use of the Time-of-Flight (ToF) technique to derive the neutron energy. The cyclotron RF signal is used to start a clock and a detector signal is used as a stop. The velocity can be obtained from the flight path and the time-of-flight distance using equation (1).

$$v = \frac{d}{t_{ToF}} \qquad (1)$$

The kinetic energy can then be obtained by substituting the velocity into equation (2).

$$E_n = m_0 c^2 \left(\beta - 1\right) \qquad (2)$$

with

$$\beta = \frac{1}{\sqrt{1 - \left(\frac{v}{c}\right)^2}}$$

where m_0 *is the mass of a neutron; c is the speed of light; d is the distance from the centre of the target to the centre of the detector; and* t_{ToF} *is the time it takes for a neutron to travel from the target to the detector.*

The only variable for each particle reaching the detector is t_{TOF}. The time-of-flight technique works on the assumptions that (i) the fast neutrons will reach the detector before slow neutrons, from a previous bunch, reach the detector; (ii) neutrons will travel straight from the target to the detector with minimum interaction with components along the path e.g. the energy loss resulting from neutrons passing through the detector window is negligible [Wo91]; and (iii) the response of all electronic equipment remains linear during the measurements.

The energy resolution ΔE_n, associated with the particular detector, can be obtained considering the case of the target thickness being very small compared to the distance *d* and can be estimated using equation (3)

$$\Delta E_n = \left[\left(1 + \frac{E_n}{m_0 c^2} \right) \left(2 + \frac{E_n}{m_0 c^2} \right) E_n \right] \frac{\Delta t_\gamma}{t} \qquad (3)$$

where Δt_γ is the time resolution of the γ-ray peak in the ToF spectrum.

2.3.1 Dimensions of the D-vault facility

The vault has up to 11 m of available length for flight paths in the direction of the beam (0°) with space to allow different detectors to be placed. At the angle 16° the positioning of the detector is limited to 8 m available flight path. This limitation at 16° also requires the detector at 0° to be placed 8 m from the target.

This chapter looked at the neutron facility at iThemba LABS, and the next chapter will consider the technique used during the experiment.

CHAPTER 3: EXPERIMENTAL PROCEDURE

3.1 The neutron experiment & data collection

The general experimental setup of the D-line facility was detailed in Chapter 2. In this section the specifics of the present measurements are described.

3.1.1 Targets for measurement: thin ^{7}Li, $H_2{}^{18}O$ and thick $H_2{}^{18}O$

All the targets that were used in the measurements at different energies are listed in Table 1.

Table 1: Summary of targets used in this experiment.

E_p (MeV)	Target	Thickness (mm)
66, 54, 42, 30	^{7}Li	2.5 ± 0.5 (1σ)
66, 54, 42, 30	$H_2{}^{18}O$	"thin" 1.9 ± 0.1 (1σ)
62	$H_2{}^{18}O$	"thick" 40 ± 1 (1σ)

Lithium-7, with a well-known ToF spectrum, was run as a reference to confirm the setup before the ^{18}O measurements. Later, ^{7}Li target data was also used to validate the data analysis procedure of ^{18}O. The thickness of ^{7}Li target was 2.5 ± 0.5 mm. The uncertainties quoted in this work all correspond to one sigma confidence limits.

The ^{18}O target used was in the form of ^{18}O-water which is readily available as it is used by the iThemba LABS Radioisotope Production Department for the production of ^{18}F. This ^{18}O-water has a density of 1.11g/mL at 20°C and an isotopic purity of 97 atom % ^{18}O, normalised with respect to hydrogen [Si18]. The target was designed by Prof. Paul Papka at iThemba LABS. Figure 15 shows the 3-D CAD drawing of the thin water target. Plastic (Kapton) windows, separated by 1.0 mm, were used to enclose the water and create a water target. The Kapton windows were 12 μm thick, to minimise the energy loss of the proton beam. Including both sides, the total was 24 μm, so that the windows were accountable for < 1% of the nominal target thickness. Calculations using the SRIM2008 code [Zi08] suggested that for proton energies between 30 and 70 MeV, the energy loss due to these plastic windows averaged at about 0.04% [Zi08] and thus no correction was deemed necessary. SRIM is a software package used to estimate the stopping and range of ions in matter. The fundamental physics of the software is discussed in detail in the book titled "SRIM – Stopping and Range of Ions in Matter" [Zi09]. SRIM is more reliable for proton ions and also improvements have been added on to its data packages based on the experimental data

[Zi10]. For protons in particular, SRIM values are within 5% of the experimental values for about 9000 iterations (statistical data points) [Zi10]. For these calculations, 99999 iterations were defined.

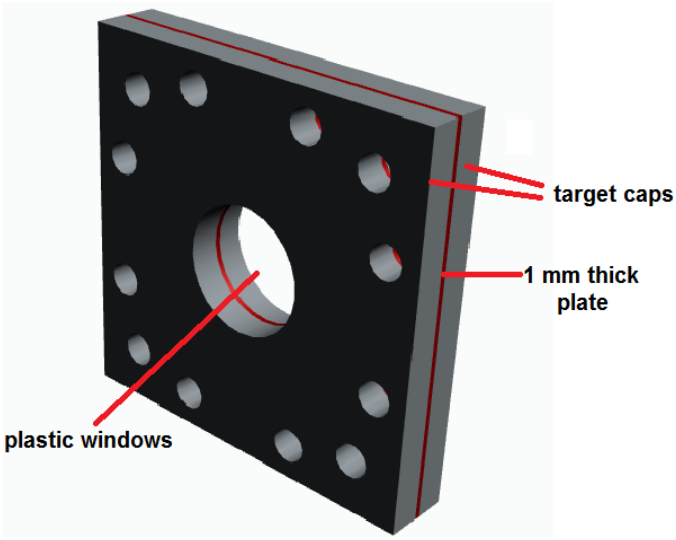

Figure 15: *The stainless steel caps used for holding together with plastic windows. This was used for 1 mm nominal thickness of ^{18}O - water target (which expanded to 1.9 ± 0.1 mm under vacuum).*

Figure 16 shows how the thin target shown in Figure 15 was mounted on the target ladder.

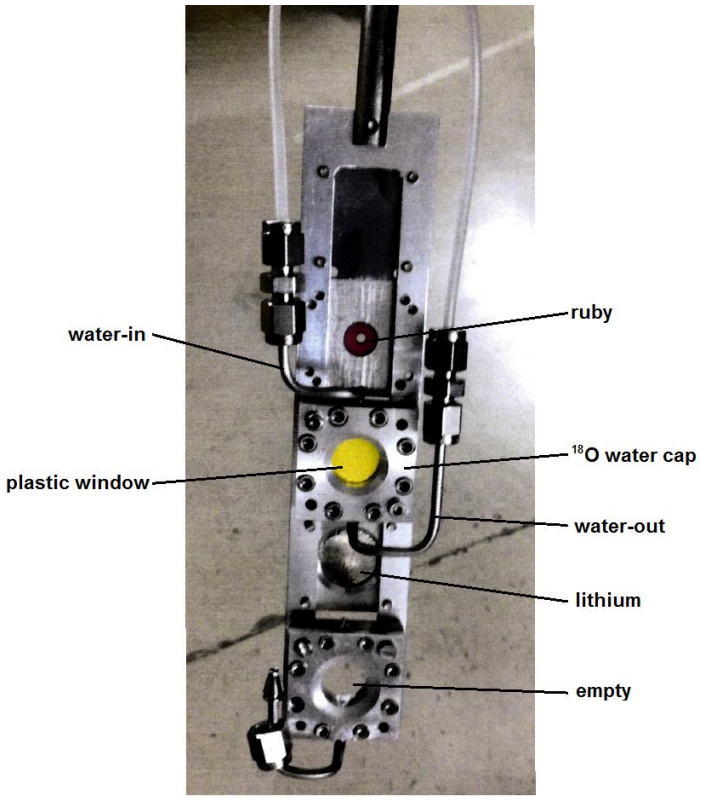

Figure 16: *A photograph of the target ladder. It shows four target frames and where the 18O-water target was placed.*

The Kapton windows bulge due to the pressure difference between the target and the vacuum in the target chamber. The target itself was pumped down to a pressure in the region of 10 mbar, so as not to provide too large a pressure difference with the vacuum. However, it was necessary to ascertain the thickness of the $H_2{}^{18}O$ target under these conditions. The target was bench-tested in air, by pressurizing it with water to 10 and 20 mbar above atmospheric pressure. A direct measurement with a micrometer gave a thickness of approximately 2.0 mm. However, it was difficult to be confident that the micrometer did not press the windows and reduce the thickness.

A better technique, which did not affect the thickness of the target during the measurement, involved shining a laser on the target. The idea is to shine the laser on the flat target before it bulges and mark the position of a reflected beam on a screen. The principle is that as the pressure changes and the windows bulge, the angle of reflection of the laser changes and thus the position on the screen shifts. The shift in position could then be used to estimate the change in thickness of the target. A geometrical relationship was developed relating the variables to a change in target thickness, see Appendix 2. The total thickness of the target was determined to be 1.9 ± 0.1 mm.

It was necessary to calculate the mean projectile energy and energy loss in the target so as to understand its effects on the broadness of the monoenergetic neutron peak. The thicknesses of the thin $H_2{}^{18}O$ targets were calculated to achieve a good time resolution in the ToF spectrum and, therefore, a good energy resolution of the monoenergetic peak in particular, as it also depends on the thickness of the target. Calculations with the SRIM2008 code [Zi08] suggested that for proton energies between 30 and 70 MeV, protons would not lose more than 2.0 MeV in the thin water target before the first primary reaction, avoiding broadening of the neutron peak, and thus achieving an acceptable energy resolution of the energy spectrum.

For the design of the thick water target, protons of 66 MeV were envisaged. The stopping length of 66 MeV protons in water was calculated to be 36 mm using SRIM2008 [Zi08]. A thickness of 40 mm ensured a complete stop of protons in the target. Figure 17 shows the 3-D diagram of the copper tube of 40 mm depth that was mounted onto the caps. The tube was filled with ^{18}O-water and was closed by a thin plastic window on the end through which the protons entered.

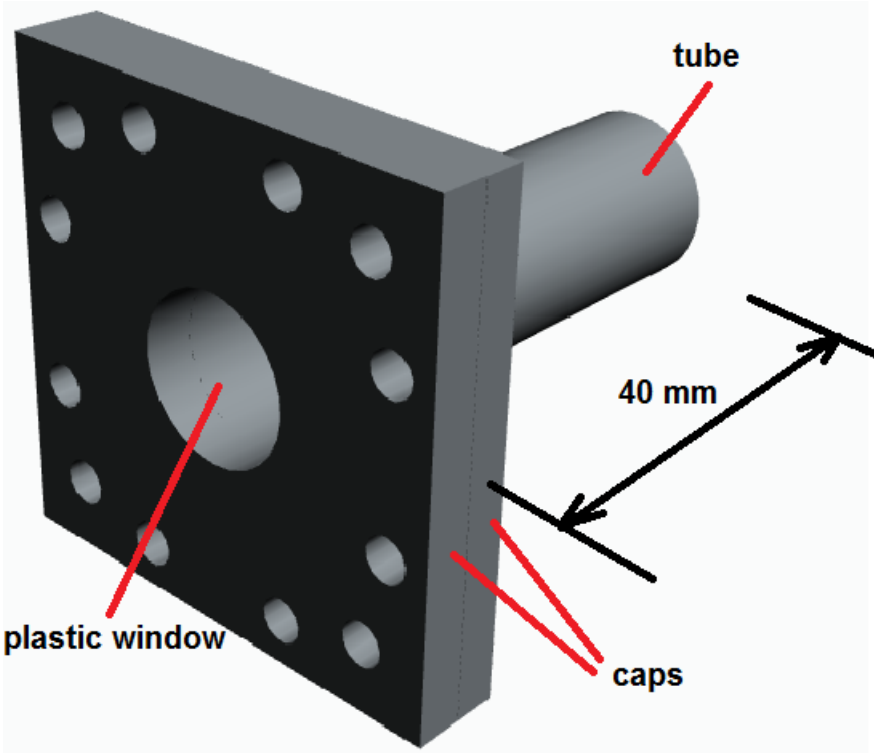

Figure 17: *The stainless steel caps used for the thick target of ^{18}O water. The 40 mm copper cylinder was used to hold ^{18}O water and the plastic window was used on the side of the incident protons.*

For operational reasons the actual proton energy used in our measurement was 62 MeV with a stopping length of 32 mm. The target used was 40 mm thick, therefore this extra 8 mm target of water would have induced self-absorption and scattering of neutrons, for which corrections would be made.

3.2 Neutron detection

NE102 and NE213 detectors were used in this work. Detection requires neutrons to interact with the detector material (hydrocarbon) to produce recoil charged particles. During the interaction, neutrons transfer their energies to particles which then recoil. Neutrons can have a wide energy range; optimising their detection needs a detector material that will be sensitive to that specific neutron energy range. The properties of neutron detectors based on the recoil proton from the neutron-proton (n-p) interaction proton recoils have been studied in great detail [Kn00]. The energy range of interest for this work is between 8 MeV and 66 MeV, hence the use of the liquid scintillator detector, NE213. The operation of the detectors is described in the next sections, including the discrimination of neutrons from gamma-rays.

3.2.1 Fast neutron detection using light nuclei and scintillator material

The signal produced by the recoil proton from the n-p interaction is normally observed by using a scintillating material that is rich in hydrogen such as a plastic or an organic liquid [Kr88]. This scintillator serves two purposes, that of being a proton target for neutrons as well as a detector for the recoiling charged particles. The produced neutron energy spectrum can be distorted by any nonlinearity of the scintillator to the energy deposited and the detector energy resolution. Therefore, laboratories around the world are still developing different detectors for various energies with many options including a combination of detectors so as to improve their efficiencies and energy resolutions [Kn00].
The primary solvent in the organic liquid scintillator, NE213, is xylene ($C_2H_4(CH_3)_2$, to which naphthalene ($C_{10}H_8$) and the wavelength shifter 1,4-bis(5-phenyloxazol-2-yl) benzene or POPOP are added. Naphthalene is used to effect quenching in the detector, enhancing the slow component of the light output [Ts83]. It also improves the uniqueness of the scintillation signals from different types of charged particles producing ionisation in the detector, which improves the pulse shape discrimination (PSD) [Bu69]. Neutron measurements are conducted in a field that contains inevitable ɣ-rays from either the neutron source or surroundings. It is thus necessary to separate neutron events from ɣ-ray events inside the detector. In the hydrocarbon detector the ionisation is caused either by electrons produced by incoming ɣ-rays, or heavy charged particles like protons produced by H(n,n')H reactions. Especially at lower energies, other heavy charged particles such as deuterons, tritons and alphas are produced from C(n,d); C(n,t) and C(n,α) reactions respectively. The ionisation in the hydrocarbon solvent gives rise to an electron excitation that emits light (scintillates) when it eventually decays. At energies less than about 12 MeV, the n-p scattering is the dominant neutron interaction in hydrocarbon media but at energies higher than 12 MeV, interactions with the carbon component become increasingly important [Br79].

Another important feature in a scintillator detector, especially in the time-of-flight (ToF) technique, is the time resolution. The absolute time resolution is derived from the FWHM of the prompt ɣ-ray peak obtained using a Time to Amplitude Converter (TAC). This time resolution includes the time resolution broadening contributed by the width of the pulsed proton beam bunches.

3.2.2 Operating the NE213 detector

The detector used in this work is an aluminium cylinder cell of 5.08 cm diameter and 10.16 cm height, filled with NE213 liquid scintillator [Kn00]. It was placed at 8 m from the target, coaxial with the oncoming neutron and ɣ-ray beam. An incoming neutron or γ-ray interacts with hydrogen and carbon atoms of the scintillator. The properties of NE213 allow the characteristic scintillation emission to take place depending on the charged particle inducing the scintillation. Charged particles and uncharged particles emit characteristic light flashes when this interaction takes place. These flashes are converted into a signal for further processing, which requires the signal to be amplified, hence the detector is coupled to a model XP2020 photomultiplier tube (PMT) by means of a light guide. This photomultiplier is a 12-dynode stage system operated at a high cathode voltage of -1750 V with the anode at ground potential for all the experiments with neutron beams. Figure 18 shows the geometry of the NE213 detector coupled to a photo multiplier tube (PMT) which has two anode outputs and one dynode output. These signals are transmitted from the vault to the electronic modules and the data acquisition (DAQ) system in the data room. The detector as shown is gain stabilised using a built-in LED PIN diode glued onto the light guide and near the scintillator, combined with a feedback system.

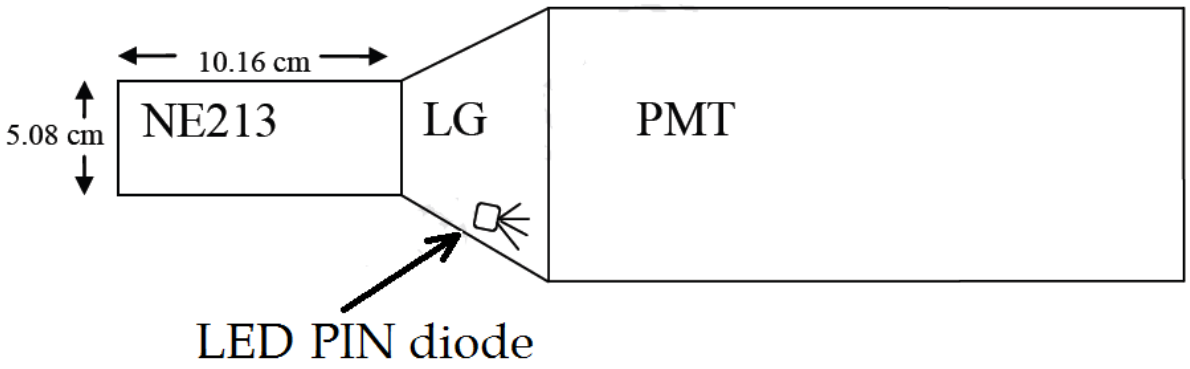

Figure 18: *The schematic diagram of the NE213 detector showing the dimensions of the scintillator and the position of the gain stabilising LED and the light guide (LG) that optically couples the active part of the scintillator to the photomultiplier tube (PMT).*

The system adjusts the gain of the PMT and keeps the changes in gain to a minimum. Gain drifts in the photomultiplier are normally brought about by variations in the detector count rate, changes in temperature, and changing magnetic fields around the detector [Mo10].

3.2.3 The Response Function of NE213

The response function of a scintillator to a particular type and energy of incident particle is defined as the pulse height spectrum resulting from all interactions of that particle in the scintillator. This function will depend on three components, σ) the energy of the incident particle; (2) the type of interactions induced by the incident particle and their cross sections, and (3) type, size, shape and geometry of the detector. The neutron may interact with hydrogen, resulting in a recoil proton through n-p scattering, and also, heavier charged particles from neutron-induced interactions with carbon-12. Typical pulse height (*h*) spectra resulting from these interactions are shown in Figure 19. The proportion of these components differs for different incident energies depending on the competing nuclear reactions. This section describes some theory behind the detection of particles using the energy they deposit into the detector.

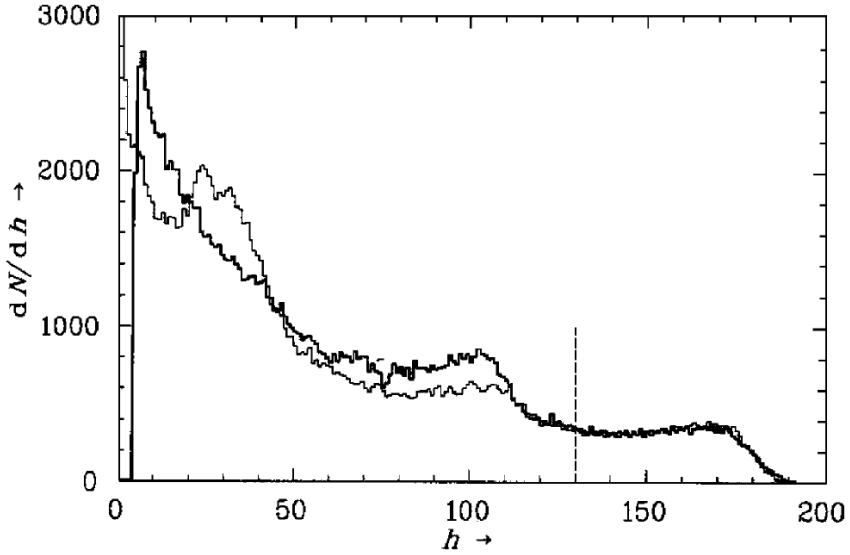

Figure 19: *The response of an NE213 scintillator to 46 MeV neutrons. The upper pulse height region h > 130, is associated with the detection of n-p scattering events only. It shows good agreement between the measured response functions (thick line) and the calculated response function (thin line). The region h < 130, includes the contribution of n-C interactions to the detector response [Br02].*

The description using a semi-empirical model of the non-linear response to charged particles of organic scintillators was proposed by Birks [Bi64]. The model describes the non-linearity to be a result of quenching effects in the detector medium and that it is determined by the specific energy loss (energy deposited per unit length) dE/dx along the ionisation trails of the particles. This specific energy loss of a given type of particle determines the scintillation light output per unit path length, dL/dx given by equation (4),

$$dL/dx = \frac{A\left(dE/dx\right)}{1 + kB\left(dE/dx\right)} \qquad (4)$$

where *A* is the absolute detector efficiency; *kB* is a parameter relating the density of ionization centres to dE/dx.

Organic scintillators have a considerable drawback when proton recoils produced by high energy neutrons are considered. For example 100 MeV protons have a stopping range of about 9 cm in a liquid scintillator. Thus, large volumes of the detector are required to limit the escape of recoil protons that have long ranges [Kl02]. Escaping particles have pulse shapes that appear to be nearly similar to the pulse shapes of Compton scattered electrons. The effect of escaping recoil protons is the “wall-effect” or “edge-effect” which decreases the neutron/ɣ-ray discrimination capability for the highest energy proton recoils [Na01]. The attempt to limit particle escapes by the use of large detector dimensions increases the probability of multiple neutron scattering events within the detector, which is not desired. The geometry and dimensions of the detector is a compromise taking into account these competing factors.

3.2.4 Pulse Shape Discrimination (PSD)

There is a need to identify whether the signal was caused by a neutron or a ɣ-ray. PSD takes advantage of the different scintillation decay times in liquid organic scintillators depending on whether the ionisation is induced by neutrons or ɣ-rays. The scintillation decay is the sum of the relative intensity of fast and slow components, see Figure 20. This scintillation in some organic scintillators is dependent on the type of the interacting charged particle.

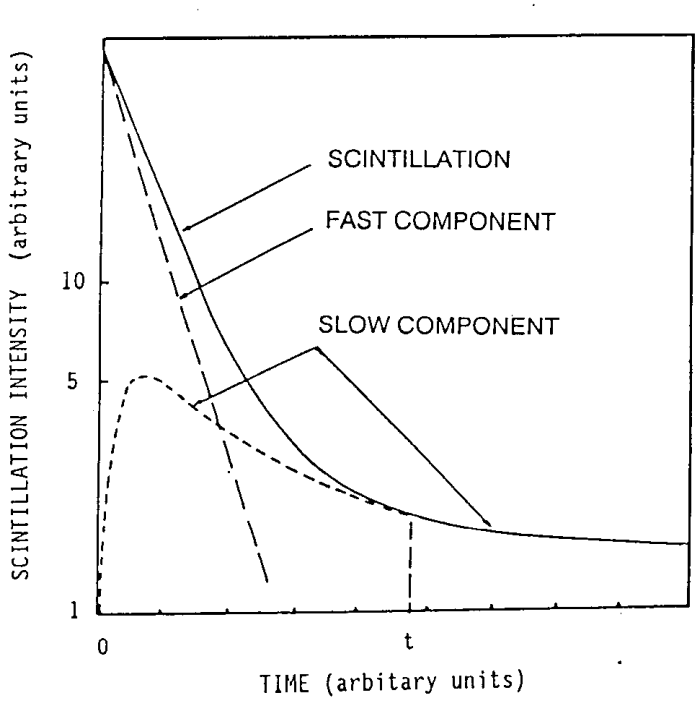

Figure 20: *The representation of a scintillation decay fast (f) and decay slow (s) component.*

The scintillation decay signal (containing a combination of fast and slow components) is expressed mathematically as

$$N = Ae^{\left(-t/t_f\right)} + Be^{\left(t/t_s\right)} \qquad (2)$$

N = is the number of photons emitted at the time t

A,B = relative magnitudes of the fast and slow light output

t_f = fast time decay constant

t_s = slow time decay constant

Electrons, generated by ɣ-rays, have a quickly changing ionisation density, which characterises them as the fast component of the decay. By contrast, recoil protons and other heavier charged particles generated by fast neutrons interacting with hydrogen and carbon are associated with the slow component of the decay.

Two methods are involved in neutron / ɣ-ray discrimination, i.e. zero crossover and charge integration. The zero-crossover method is used in this work, which in essence distinguishes light pulses produced by neutrons and ɣ-rays interacting with the detector according to where the fall time of the pulse crosses the zero level in pulse height. A Pulse Shape Discriminator 2160A module [Sp74], developed at FAST ComTec in Germany, was used in this work. The operation of the electronic circuit inside the unit takes the pulse from the anode and integrates and differentiates it in a preamplifier so as to produce a bipolar pulse.

To enhance the distinct pulses from neutrons and gamma rays, the differentiated signal is processed in a high-gain amplifier. The zero-crossing point of the output pulse, see Figure 21, is related to the particle type, with neutrons crossing zero later than ɣ-rays. This time difference is measured relative to a constant fraction timing signal also derived from the anode pulse (see section 3.2.5).

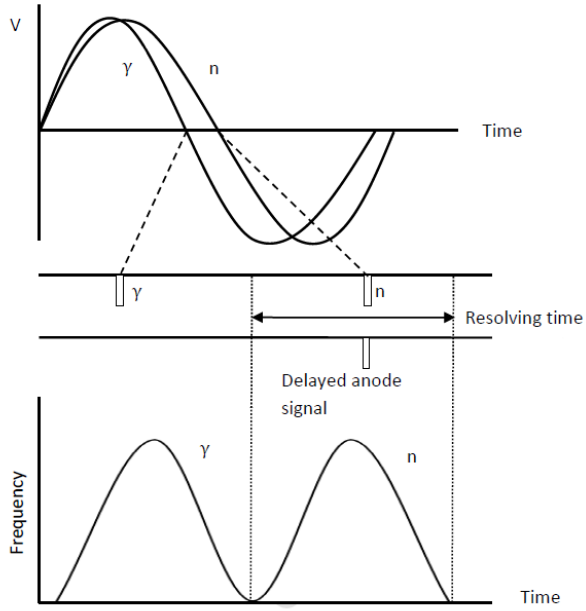

Figure 21: *An illustration of the pulse shape discrimination using the zero-crossing point of a gamma ray and a neutron signal [Co86].*

Recent technological advances, for an example by Comrie *et al*. [Co15], have been made to digitally discriminate gamma-ray events from neutrons. This digital discrimination is achieved by implementing algorithms in the code, the process known as software-implemented constant fraction discrimination (or digital CFD) [Co15]. Figure 22(a) shows digitised pulses from charged particles when neutrons and gamma-rays interact with the detector. The integrated pulses for these events are shown in Figure 22(b). The slow component in these pulses is characteristic of the ionising particle and stimulated by the high ionisation density. This makes it possible to discriminate between different particles that even deposit the same energy in the detector.

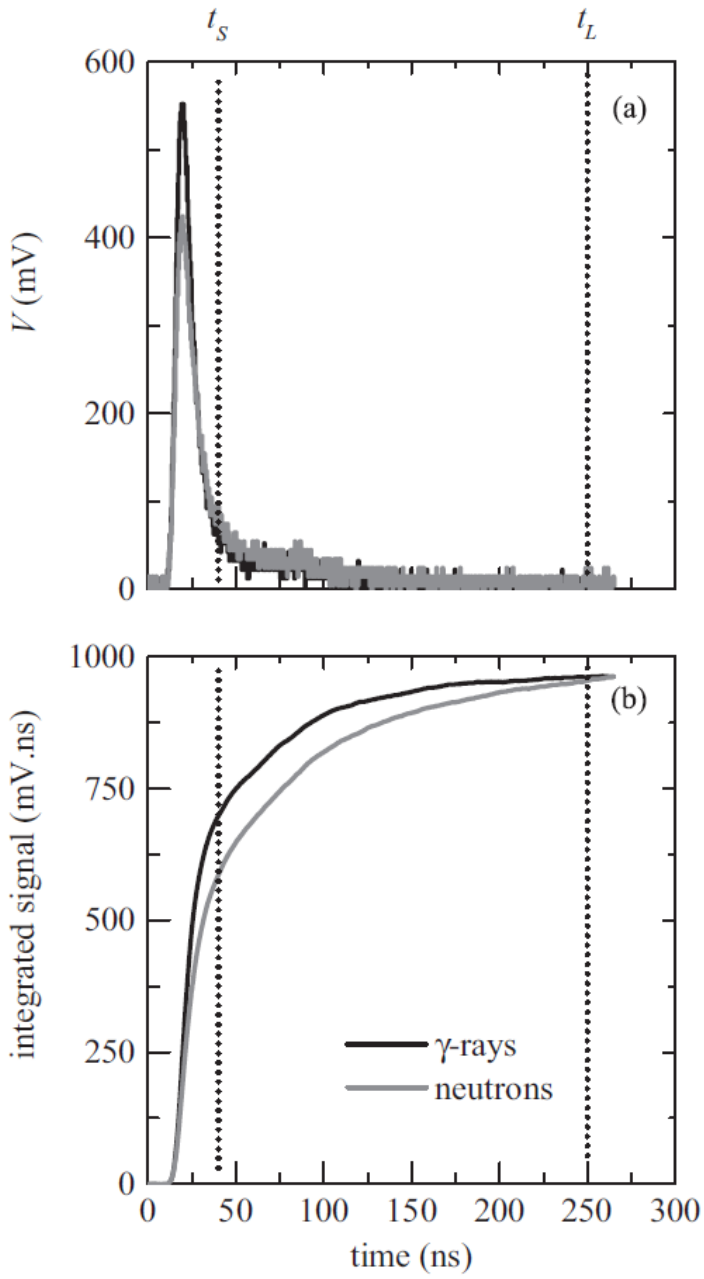

Figure 22: *Typical digitised (a) pulses and (b) pulse integrals for events arising from neutron and gamma-ray interactions in the EJ301 scintillator. The pulses were selected to have the same total integral and are shown after baseline subtraction. Integration times t_S and t_L are indicated [C015].*

3.2.5 NE213 detector electronics setup

Table 2 provides abbreviations used in the circuit diagrams of electronic module connections.

Table 2: Below are abbreviations used for the electronic modules of the NE213 / NE102 detector assembly.

PA	Pre-Amplifier
DA	Delay Amplifier
CFD	Constant Fraction Discriminator
UCO	Universal Coincidence
DLA	Delay Line Amplifier
GDG	Gate and Delay Generator
HV	High Voltage
PSD	Pulse Shape Discriminator
TAC	Time to Amplitude Converter
TFA	Timing Filter Amplifier
TSCA	Timing Single Channel Analyser
RF	Radio frequency
LED	Light Emitting Diode
L (NE213 diagram)	Pulse Height parameter
L (NE102 diagram)	Pulse Height parameter
S	Pulse Shape parameter
T	Time-of-Flight parameter

Figure 23 below shows the signal processing circuit diagram for the NE213 detector. The dynode signal is used to process the energy deposited (pulse height parameter *L*) by the particle in the detector. The anode signal from the PMT is divided into two and used for processing of (1) the particle identification (pulse shape parameter *S*), and (2) the time-of-flight parameter *T* of the detected particle.

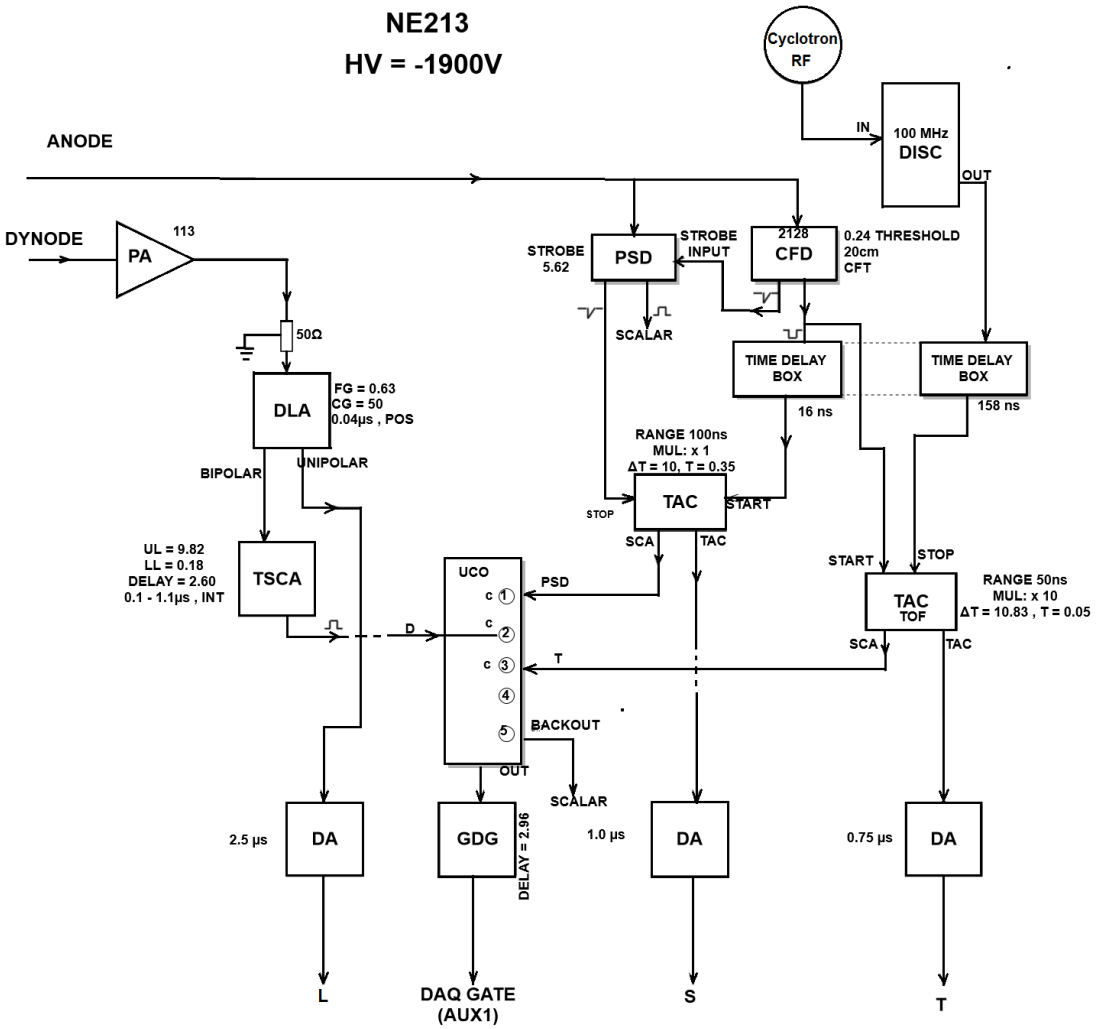

Figure 23: *A schematic arrangement of electronic modules of the NE213 detector assembly.*

The anode signal triggers a CFD and produces a logic pulse which is used in various parts of the circuit. It is used to measure the time-of-flight (*T*) of the radiation by starting a TAC which is stopped by the Cyclotron Radio Frequency signal (RF).

The CFD output is also used in connection with the PSD unit. It is used to gate (strobe) the PSD unit to release the bipolar signal to the stop input of a TAC, and the CFD output is used to start the TAC, thereby affecting a measurement of the zero-crossover time of the particle identity (PID) signal. The UCO compares the coincidence of ALL three (3) parameters *L, S* and *T* and then gates three ADCs to acquire these parameters. The signal from NE213 results in three signals which are registered by the ADCs as three numbers attributed to one event.

The event data is recorded in sequential list mode using the FAST ComTec multiparameter data acquisition system (MPA-3) [Fa10] and a computer to process event information. This list mode allows for later re-analysis and replay of data when considering neutron / ɣ-ray

cuts; pulse height thresholds and ToF windows [No11]. MPA-3 allows full neutron and ɣ-ray spectra making it an ideal candidate for ToF versus PSD matrix analysis [Ch13].

3.2.6 Operation of the NE102 detector

During the experiment, the neutron beam at 0° passed through the gain-stabilised plastic scintillator, NE102A detector, which is optically coupled to an XP2020 photomultiplier tube. This detector was operated in transmission mode as a fluence rate monitor. Both the fast anode signal and the slow dynode signal are constantly monitored to observe any changes.

The NE102 detector was used to identify proton beam current fluctuations by observing fluctuations in the neutron flux. The monitor may also be used to compare the relative neutron fluence measured by the NE213 detectors [Ha11].

Beam current stability is important for data quality. To validate beam stability, the spectrum and the ratio between a total number of neutrons in the ToF spectra to the total charge accumulated must be consistent throughout the measurement. Considerable beam current fluctuations will reflect on these parameters, declaring data to be inconsistent and thus invalid.

The monitor is also equipped with an LED-based gain stabilisation system which compensates for gain changes resulting from beam fluctuations. The user must routinely trip the gain in the stabiliser module during the experiment to restore desired settings. The scintillations induced by neutrons and gamma-rays inside the detector are turned into electric pulses which are transmitted through the anode and dynode to the electronic modules and the DAQ system in the data room for further processing.

3.2.7 NE102 detector electronics setup

Figure 24 is the schematic circuit of the NE102 detector electronics. The signal from the anode triggers a CFD to produce a logic pulse which is sent to start a TAC in the timing circuit. The TAC is stopped by the Cyclotron RF signal for a time-of-flight (T) measurement. The dynode output gives the pulse height signal (L) which is related to the energy deposited by the incoming particle. The high voltage (HV) is set such that NE102 suppresses gamma-rays passing through the detector and count neutrons only. The UCO compares the coincidence of valid anode and dynode signals to accept the event. Each event from the

NE102 detector has two parameters attributed to it, i.e. the pulse height parameter *L* and time-of-flight *T*.

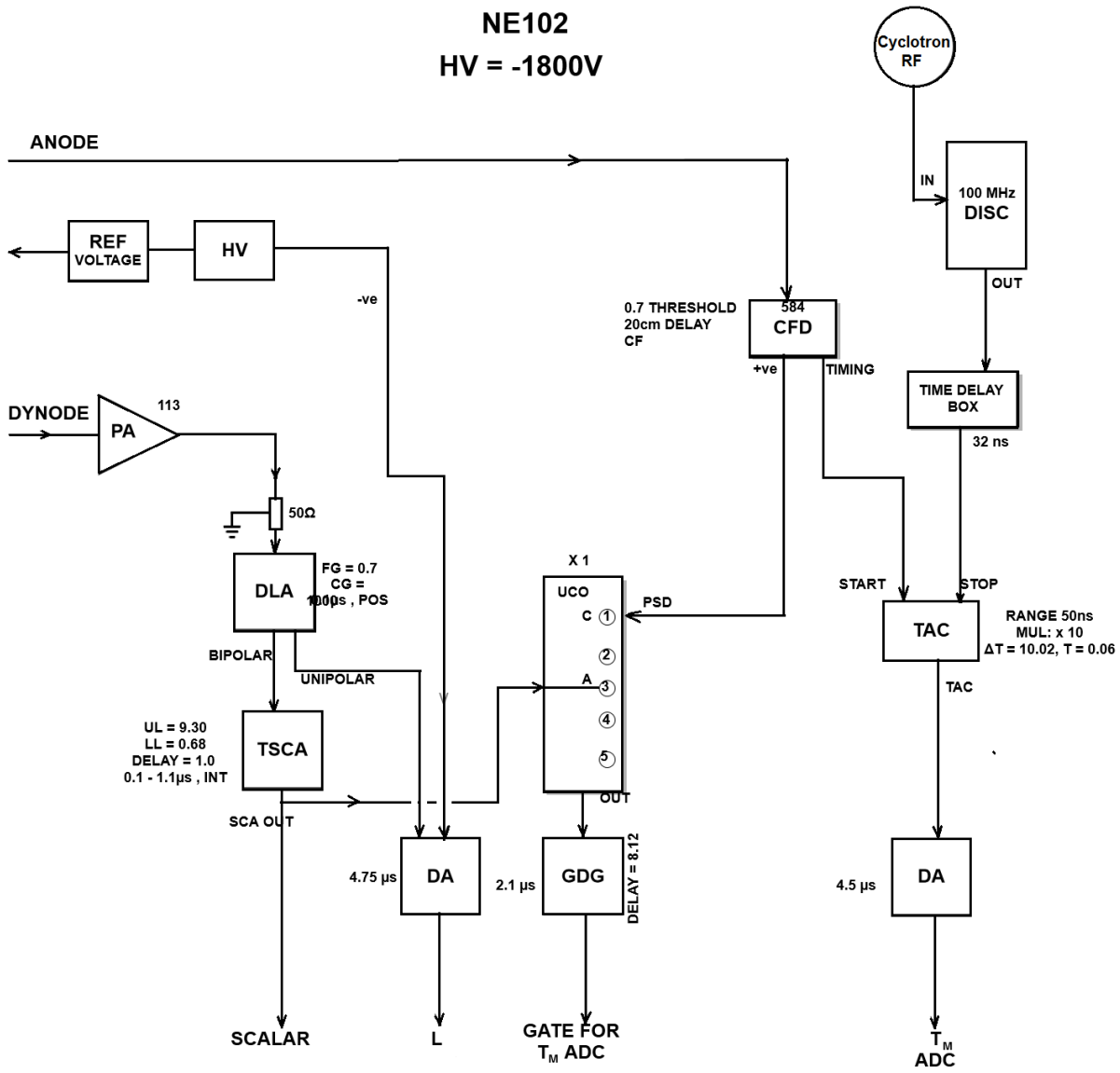

Figure 24: *A schematic arrangement of electronic modules of the NE102 detector assembly.*

3.2.8 Data Collection

There were three ADCs for the NE213 detector and two ADCs for NE102 detector through which the signals were fed and then recorded by the DAS. They are listed below:

i) ADC 1: Pulse Height, NE213

ii) ADC 2: Pulse Shape (*S*), NE213

iii) ADC 3: Time of Flight (*T*), NE213

iv) ADC 4: Time of Flight (*T*), NE102

Five scalars were recorded by the data acquisition system and saved in the event by event mode file (*lst) as well as the replayable multiparameter acquisition (*MPA) file. Scalars were set and named in the following order:

i) Scalar 2: total charge (Q)

ii) Scalar 3: NE102 gates: high threshold

iii) Scalar 4: NE102 gates: low threshold

iv) Scalar 6: PSD singles

v) Scalar 7: NE213 gates

3.3 Typical time-of-flight spectrum from the NE213 detector

The ToF technique is based on the principle that if neutrons and gamma-rays from the target traverse a fixed distance (*d*) to the detector, the measured flight time (t_{TOF}) allows their velocities, and hence their energies, to be calculated. The time-of-flight spectrum has a prompt ɣ-ray peak which is used to measure the total time resolution of the system by measuring its full width at half maximum. The width of the peak depends on the target thickness as well the width of the pulsed beam bunches. The neutron ToF measurements were completed using the fast-neutron detector (NE213) at angles of 0˚ and 16˚ relative to the incoming proton beam, with the detector placed at a distance of 8m from the target for both angles.

3.3.1 Neutron production and the characterisation of the ToF spectrum

To understand the time-of-flight measurements, the characteristics of the neutron spectrum become important. A typical thin target, composed of a light element, will produce a ToF spectrum with a visible peak of monoenergetic neutrons and a continuous tail of lower-energy neutrons. Figure 25 shows a two-dimensional plot of counts as a function of the pulse height parameter *L* and the time-of-flight parameter *T*.

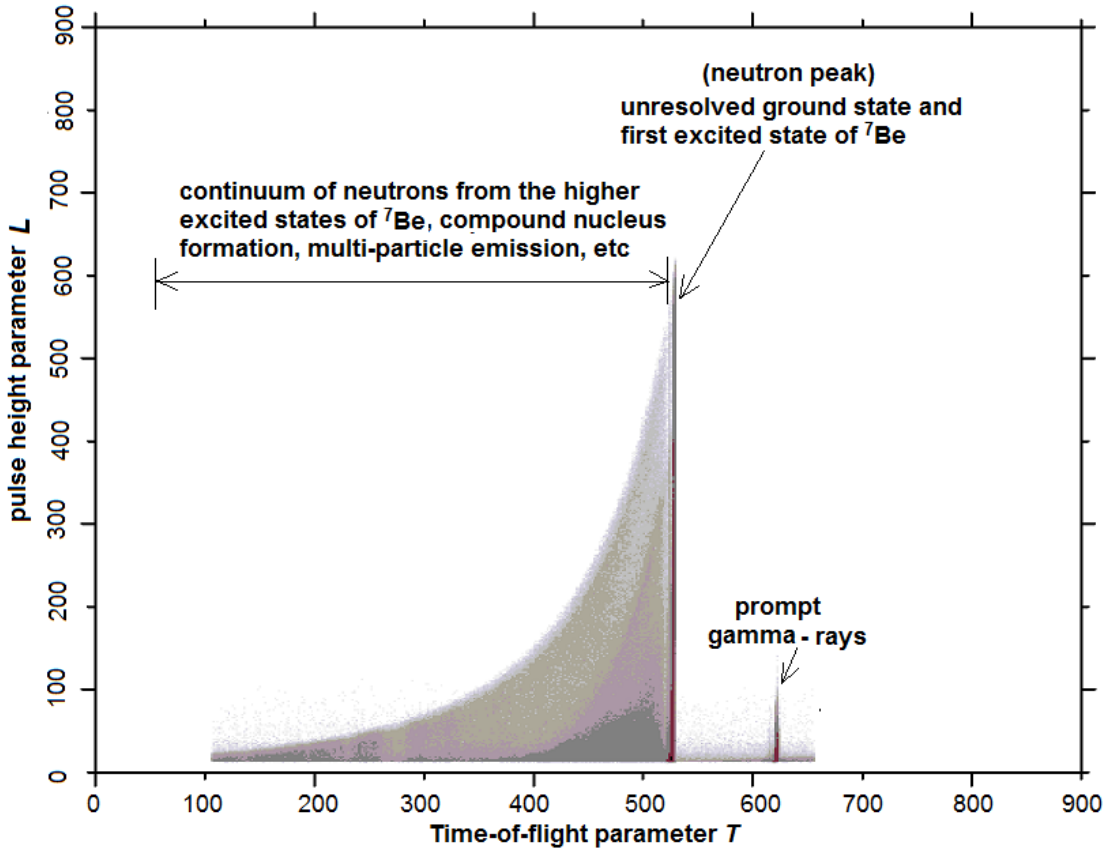

Figure 25: *Counts as a function of the pulse height parameter L and time-of-flight parameter T. This data was produced by a 66 MeV proton beam bombarding a 2.5 ± 0.5 mm thick Li target at 0°.*

These data were produced by a 66 MeV proton beam bombarding a 2.5 ± 0.5 mm thick Li target at 0°. The distribution indicated as the neutron peak is associated with the unresolved ground state and first excited states of beryllium (^{7}Be) which are separated by 0.429 MeV. Therefore, with a detector energy resolution of about 1.5 MeV in the peak region, these two states cannot be resolved. The continuum tail is from other complex processes including the neutrons leaving ^{7}Be in higher excited states, compound nucleus formation in the target, multi-particle emission, etc. which is characterised by a statistical energy distribution of nucleons, hence the continuum [Vr12]. The distribution of the prompt gamma-rays is also evident.

Figure 26 shows the time-of-flight spectrum which is a projection of counts in Figure 25 on to the time-of-flight axis. The features described above are clearly visible.

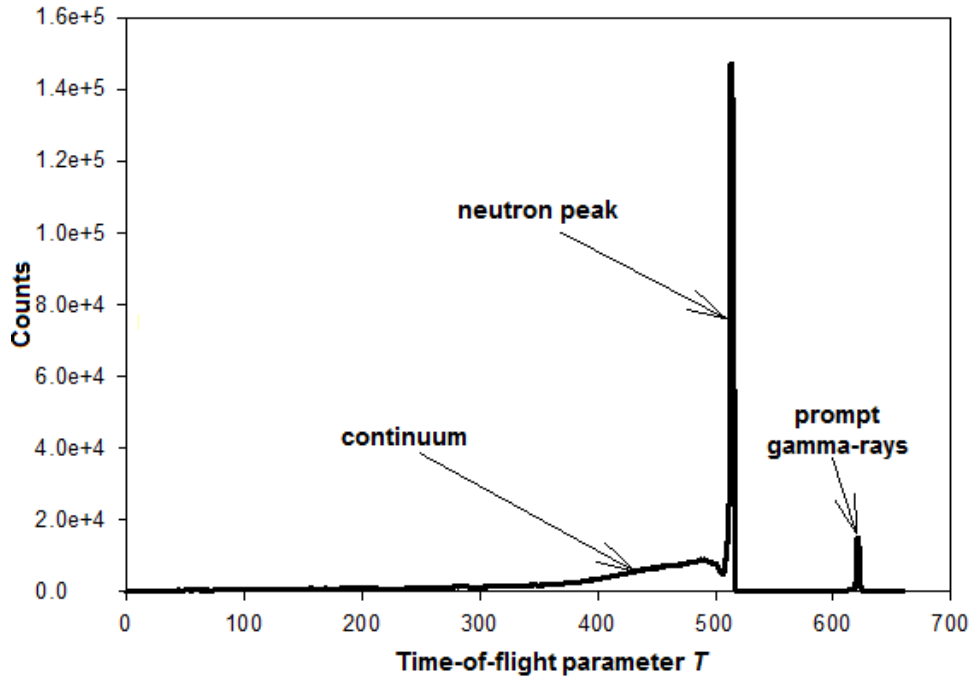

Figure 26: *The time-of-flight spectrum of both neutrons and gamma-rays produced by 66 MeV protons on 2.5 ± 0.5 mm thick ^{7}Li target.*

3.4 Monitoring the experiment

The time-of flight spectrum was observed and used to monitor the experiment, to check the data quality and target integrity.

3.4.1 Checking structural scatterings & background: “target-out” run (empty)

The need to do an empty frame run was explained in section 2.2.2. Procedurally, this was also done before every run so as to observe background spectra and save them for future reference during data analysis. In all runs, no adjustments were necessary resulting from this test. Below is Figure 27 showing a typical ungated background spectrum. The level of the background was about 3% of the counts in a corresponding ^{7}Li spectrum. This spectrum has no peaks showing no evidence of the beam striking components, thus implying a "clean" neutron spectra during target runs.

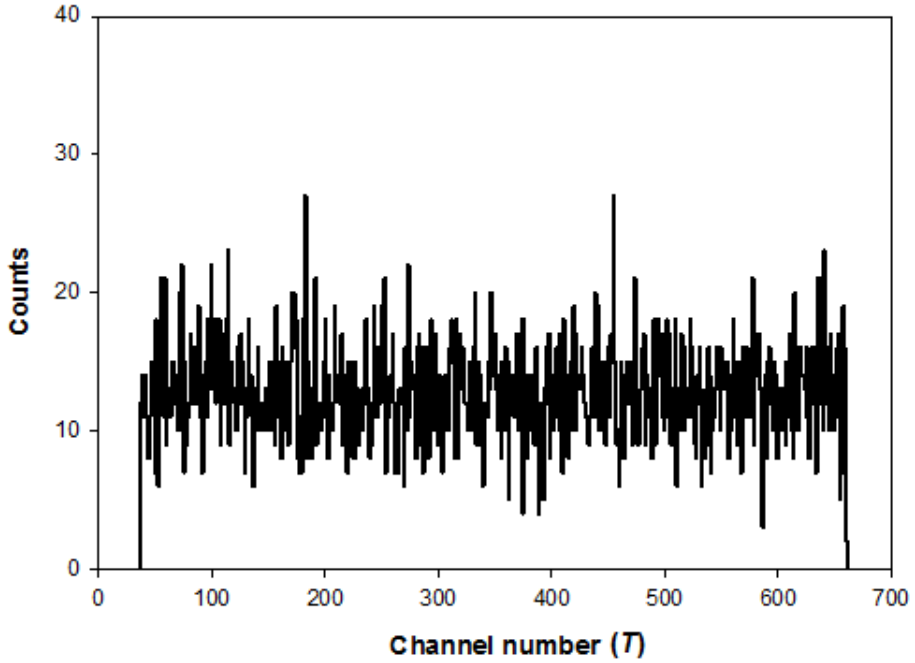

Figure 27: *The ungated ToF spectrum from a "target out" run.*

3.4.2 Beam current stability and neutron flux consistency

There was a need to validate the target stability during each run. This was to be sure that the ^{18}O-water did not boil away. Beam stability was checked by monitoring either the ratio of total counts to total charge Q or peak counts to total charge Q. Instead of a single long run, short runs were performed, ratios calculated and consistency checks were made. After these ratios confirmed consistency, longer runs were performed, which were also monitored.

The next chapter will explain the approach to the analysis of data collected.

CHAPTER 4: DATA ANALYSIS

The aim of the data analysis is to produce neutron energy spectra from the original experimental data. This procedure is illustrated using ^{7}Li data that was collected. Table 3 shows all the ^{7}Li measurements that were done with at different energies and corresponding beam parameters and settings.

Table 3: The summary of radio frequencies, beam profiles and beam energies; for the ^{7}Li measurement.

E_p (MeV)	Target	Pulse selector	Radio Frequency - RF (MHz)	5:1 Selected RF (MHz)	Pulse separation (ns)	Expected neutron peak energy (MeV)	Measured neutron peak energy (MeV)
66	^{7}Li (2.5 mm)	1:5	16.374	3.275	305.4	63.7	64.8 ± 0.5
54	^{7}Li (2.5 mm)	1:5	14.943	2.989	334.6	51.6	51.6 ± 0.5
42	^{7}Li (2.5 mm)	1:5	13.298	2.660	375.1	39.4	40.1 ± 0.5
30	^{7}Li (2.5 mm)	1:5	11.343	2.269	440.8	27.1	26.7 ± 0.5

4.1 Extracting neutron events

The first requirement is to extract events corresponding to neutrons only. Figure 28 shows the pulse height *L* versus pulse shape *S* spectrum of quasimonoenergetic neutrons from 66 MeV protons on 2.5 ± 0.5 mm thick ^{7}Li. The distribution is clearly separated into regions caused by different types of particles in the detector. For clear illustration, the regions are separated by black lines and correspond to recoiling electrons, protons, deuterons and alpha particles, respectively.

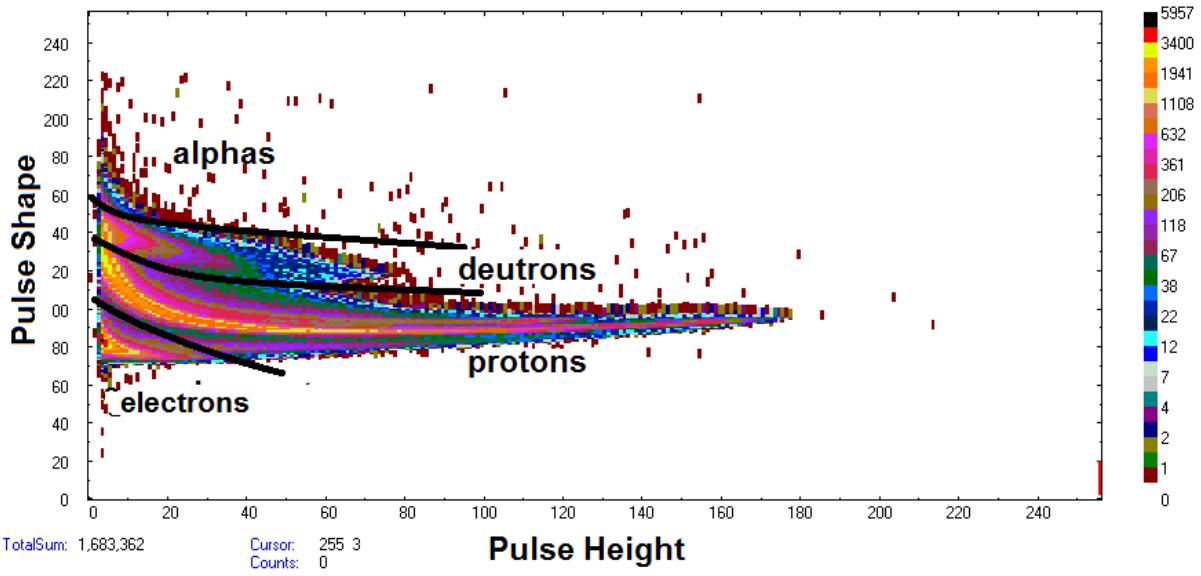

Figure 28: *The pulse height versus pulse shape event density matrix.*

The event density matrix (pulse height - *L* vs pulse shape *S*) contains events from neutrons and gamma-rays. It is necessary to gate on neutron only events and neutrons above 2.5 MeV and this required an NE213 detector calibration which relates channels to energies. Details of the procedure are explained in the next sections. For all energies and angles, the energy spectrum was normalised per charge and per unit angle as explained in section 4.3.1.

4.1.1 NE213 energy calibration

There is a relationship between the pulse height parameter and the response function of the NE213 detector. The response function depends on the type and energy of the radiation, as well as the shape and geometry of the detector [Bu90]. A pulse height calibration of the NE213 detector, as well as measurements of its response functions, was performed using ɣ-rays and neutron sources. This was done to find the detector pulse height threshold and experimental gain settings, as well as to obtain the measurement of the true zero of the MPA-3 pulse height parameter, *L*. The calibration is required to set a threshold of 2.5 MeV on the pulse height signal. This allows the neutron threshold energy for gating in the *LS* matrix when gating neutron only events.

The following radioisotopic sources were used for the calibration: ^{22}Na,^{137}Cs,^{207}Bi and ^{241}Am-^{9}Be. A typical spectrum of ^{207}Bi is shown in Figure 29.

A background spectrum was collected for spectrum correction purposes.

The responses of the NE213 detector to the 0.569 MeV and 1.065 MeV ɣ-rays of ^{207}Bi include the Compton edge and the pair production double escape edge, see Figure 29. The Compton edges were used as calibration points for the pulse height channel of the Compton peak being associated with 95% of the calculated maximum Compton electron energy [Ma78]. The energy of the Compton edge, E_c, was calculated using the following equation below [Kn00]:

$$E_c = \frac{2E_\gamma^2}{2E_\gamma + m_e c^2} \qquad (5)$$

where $m_e c^2$= 0.511 MeV, E_γ = 0.569 MeV and 1.065 MeV. Therefore, E_c for ^{207}Bi was calculated to be 0.394 MeV and 0.857 MeV.

The energy of Compton edge was estimated by fitting a Gaussian to the edge and adding the fitted FWHM to the fitted centroid.

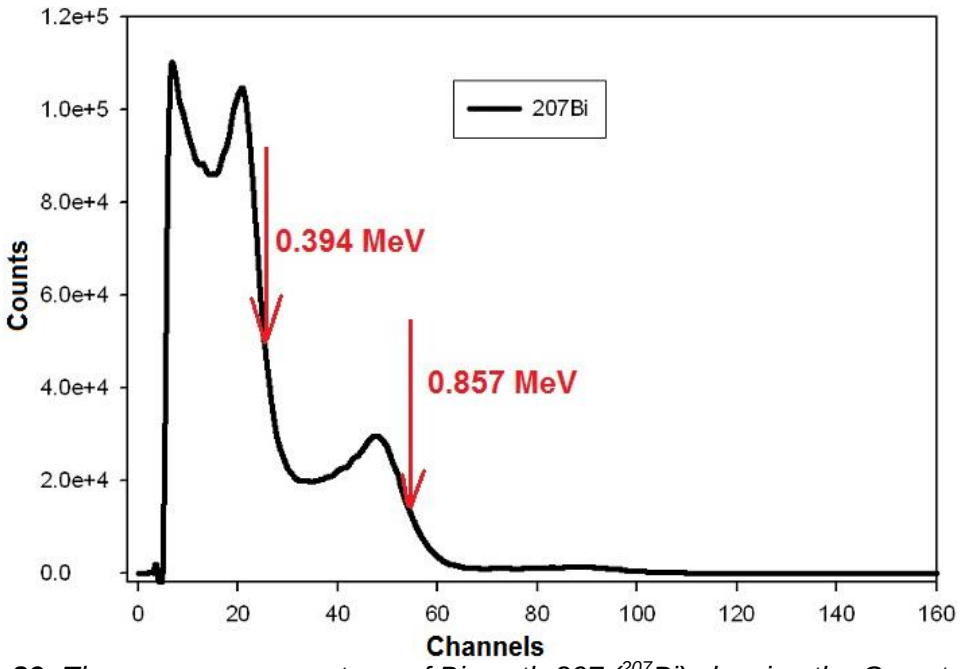

Figure 29: *The gamma-ray spectrum of Bismuth-207 (^{207}Bi) showing the Compton edge. The red arrows show the corresponding energies of the calculated Compton edge E_c.*

All other sources were also analysed and the plot of the energy of the Compton peak edge, in MeV, against the corresponding channel number, is shown in Figure 30. From this plot, we derived the calibration in channels per MeV. The zero offset from the linear equation was calculated to be zero, therefore no correction to the equation was deemed necessary. The calibration was used to correct the channels in the *LS* matrix when gating.

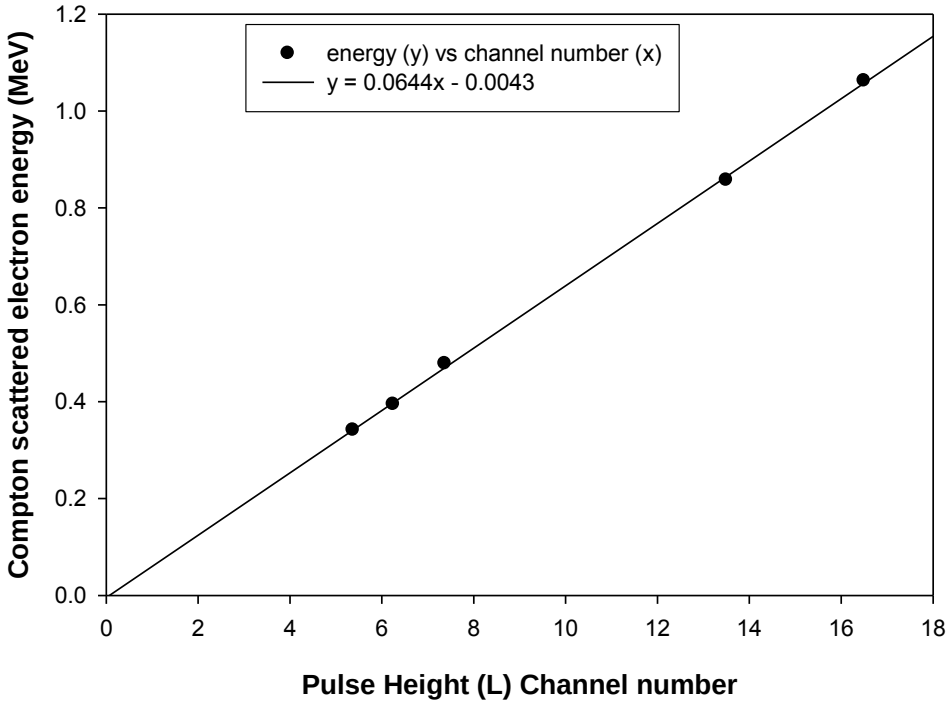

Figure 30: *The NE213 energy calibration curve.*

4.1.2 Manual procedure to reduce energy spectrum

After identifying neutron events from Figure 28, events of interest in the pulse shape – pulse height matrices were chosen using contours of loci as shown in Figure 31. A neutron cut-off energy of 2.5 MeV was calculated to match channel number 10, (38.9 ÷ 4 = 9.7), from the NE213 energy calibration, where the factor 4 is the coarse gain correction in the *LS* matrix below.

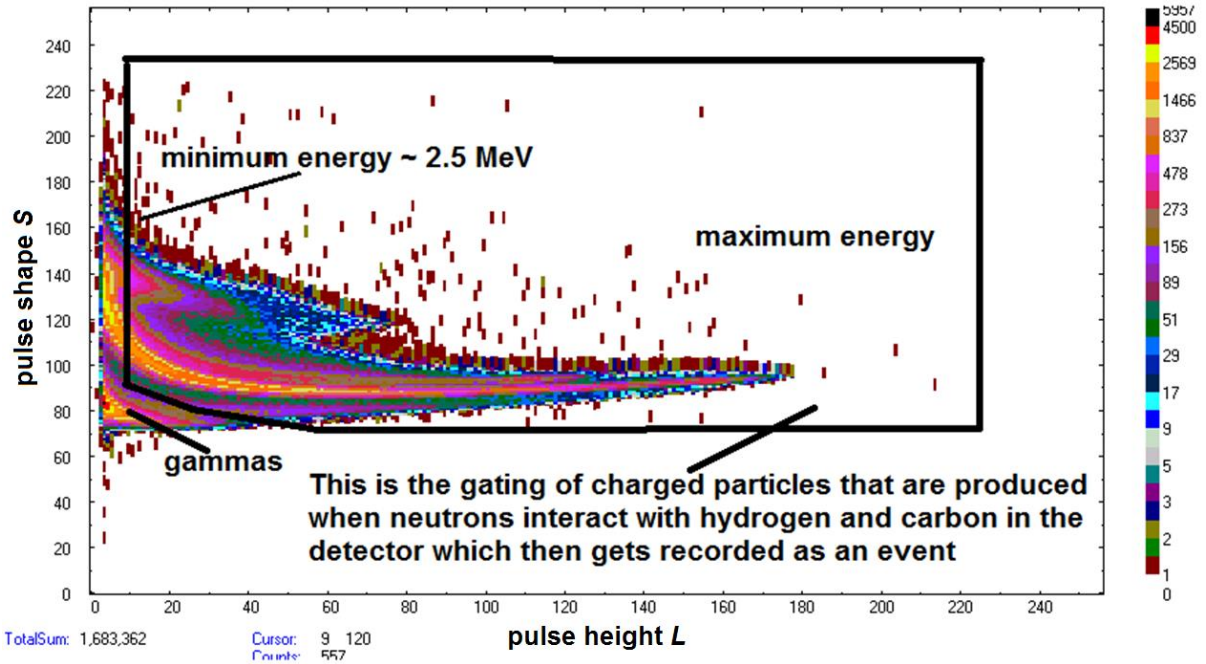

Figure 31: *The pulse height versus pulse shape event density matrix. It shows how the neutrons only condition is applied as well as the cut to remove low-energy neutrons.*

4.2 Neutrons and prompt gamma-rays in the ToF spectrum

Before the energy spectrum can be produced, the time spectrum needs to be calibrated.

4.2.1 NE213 Time to Amplitude Converter (TAC) calibration

To calibrate the ToF spectra, the ToF signal was delayed by cables of 100 ns length. Figure 32 shows how two 100 ns delay cables were used to shift the peak twice. The ratio between time shift and the number of channels between two centroids gave the time dispersion of the spectrum.

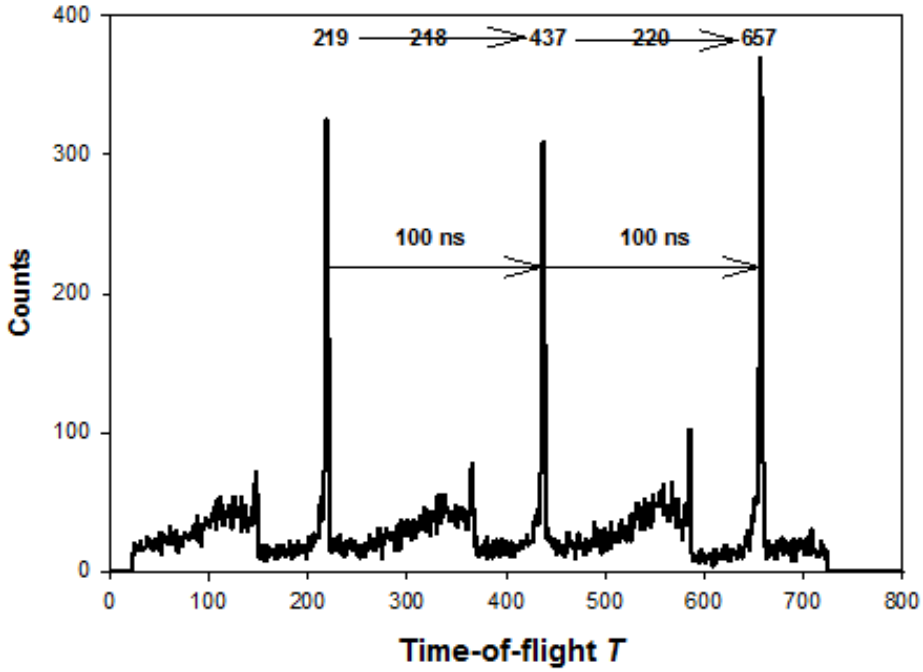

Figure 32: *The TAC calibration. The ToF spectrum is shifted by using a delayed cable of known time delay to establish a relationship between time in nanoseconds and each channel.*

The time-of-flight signal is converted from dimensionless channel number into time dimensions by calibrating the TAC using equation (6) below,

$$t_{TOF} = \frac{T_0 - Tn_{channel}}{F} \qquad (6)$$

where T_0 is the channel number corresponding to the reference time that the particle leaves the target; $Tn_{channel}$ is the channel that is converted into a time-of-flight in nanoseconds; and F is the channel to time TAC calibration (channels per nanoseconds).

For this experiment, the TAC calibration was 0.46 nanoseconds per channel (ns/ch) which may also be expressed as 2.17 channels per ns.

In our measurement, the total time resolution was measured from the prompt gamma-ray peak and varied with energy. The broadest ɣ-ray peak was produced in the 30 MeV measurement with a width of about 1.3 ns. This width includes a contribution from the proton beam bunches which were 1.0 ns wide. The intrinsic time resolution of the detector, Δt_γ, was found to be not more than 0.8 ns, after subtracting the beam bunch width in quadrature:

$$\Delta t_\gamma = \sqrt{(1.3)^2 - (1)^2} \qquad (7)$$

The energy resolution in the peak region of the neutron energy spectrum corresponding to this time resolution of 0.8 ns was estimated using equation (3) to be about 1.5 MeV.

The pulsed beam minimised overlaps where slow neutrons of the previous pulse would arrive at the detector after fastest neutrons from the current pulse.

4.3 Transforming time to energy

The aim is to convert this ToF spectrum into an energy spectrum. The original data were replayed and “neutrons only” events were selected by applying a two-dimensional gate shown in Figure 31. The ToF spectra were saved as a *CSV file for further analysis in a spreadsheet. These ToF spectra spanned 1024 channels. Each channel was then converted into the corresponding time-of-flight using the TAC calibration. Using the so-called “manual” energy spectrum reduction, the ToF spectrum was transformed into an energy spectrum by using the energy formula inserted in a spreadsheet. However this procedure is not straightforward, as many time channels may fall into a single energy channel. As can be seen in Figure 33, the relationship between neutron energies and their corresponding time-of-flight meant that several time channels corresponded to one 1 MeV bin, requiring tedious manual rebinning of the energy spectrum into uniform 1 MeV bins.

This time-energy relationship can be very sensitive if we consider the inverse square relationship between neutron time-of-flight and its energy. At high energies particularly in the peak region, the energy is very sensitive to a slight change in TAC channel distribution. Therefore the time resolution is important as it affects the energy resolution and the peak shape. The sensitivity of the TAC is illustrated in Figure 33.

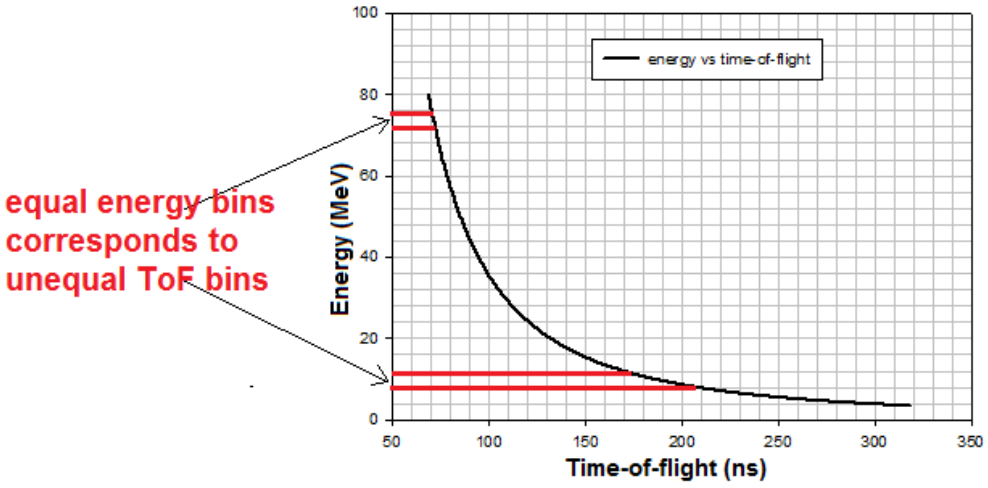

Figure 33: *A typical relationship between the energy of all neutrons reaching the detector and their corresponding time-of-flight.*

4.3.1 Experimental data reduction to energy spectrum using the C++ (Neutron Energy Spectrum Reduction – NESR code)

Because the re-binning is a tedious work to do, the already available c++ code used for sorting the data on an event-by-event basis was modified to "automatically" transform the ToF to energy in 1 MeV bins. To prove the correctness of the code, the idea was to reduce the energy spectrum of ^{7}Li at 66 MeV at angle 0° in both manual and automatic ways.

This automated method used an existing NESR code that reads the experimental (event-by-event) data file used for extracting a ToF spectrum, (see Appendix 3). The intention was to improve it further and embed the relativistic energy formula and rebinning process so as to produce neutron energy spectra in 1 MeV bins quickly and reliably. This code was used for both thin targets of ^{7}Li and ^{18}O-water measured at 66; 54; 42 & 30 MeV at angles of 0° & 16°**,** as well as the thick target of ^{18}O-water measured at 62 MeV at angles of 0° & 16°**.** Data were reduced from the raw event-by-event data file and converted into neutron time-of-flight spectra and then to energy spectra.

During the execution of this interactive code, the user needed to enter input parameters required to validate the raw data file by reading its file header, to give the number of ADCs in the data file the centroid of the prompt gamma-ray peak, detector distance and TAC calibration. Also, neutron events of interest were selected using coordinates that are appropriately written in a text file called "data cuts". They are selected such that they gate neutrons only, as well as those above 2.5 MeV.
For correct energy binning of each neutron event, the time-of-flight (t) must be turned into a real number by adding a random value between 0 and 1 and corrected for the possible shifting of the spectrum by subtracting 0.5. The neutron energy was calculated as a real number using the relativistic formula of the variable 'e' as illustrated in Appendix 5. The result was turned back into an integer so that the neutron energy spectra were in 1.0 MeV bins.

Before the final spectra were produced, the neutron counts were corrected for detector efficiency, (see section 4.3.2). The neutron energy spectrum, *N(E)* was normalised to the total beam charge (in microcoulombs) and the solid angle of NE213 detector into the conventional units of 10^{7}n.sr^{-1}.μC^{-1}, which reads as neutrons per steradians per micro coulombs, see equation (8). The solid angle Ω was calculated as that subtended by the face of the NE213 cell, which has the diameter of 0.051 m at 8.00 m distance from the target, to be 3.068x10^{-5} steradians, see Appendix 1.

$$N(E) = \frac{k_{dt} k_{att} N}{\varepsilon(E)} . \frac{10^{-7}}{Q\Omega} \quad \text{n.sr}^{-1}.\mu\text{C}^{-1} \qquad (8)$$

where N is the number of counts per MeV, k_{dt} is the correction factor for the dead time losses, k_{att} is the correction factor for neutron attenuation in air from the target to the detector; $\varepsilon(E)$ is the NE213 detector efficiency per MeV; Q is the total beam charge in microcoulomb (μC).

4.3.2 Discussion on correction factors on neutron yields

It is necessary to take into account the counts lost due to, for example, the detector efficiency. Corrections required are:

i) Detector efficiency: $\varepsilon(E)$

ii) Dead time: k_{dt}

iii) Neutron beam attenuation: k_{att}

iv) The slewing effect (time walk)

i) Neutron detection efficiency

There is a need to understand the efficiency of scintillator detector in the 10 – 70 MeV region covered by this work. The response function becomes complex as the neutron energy increases. As mentioned previously, the incoming neutron will either interact with hydrogen or carbon in the liquid scintillator. High energy neutrons will produce high energy proton recoils that are more likely to escape the detector. Madey *et al*. speculated that the scintillator light response was affected by charged particle escape [Ma78], so that the detector efficiency will also depend on the type, size, shape and geometry of the detector.
Reduced neutron spectra are corrected for NE213 detector efficiency using the efficiency function which has been calculated using Monte Carlo codes [Pe08]; MCNPX and SCINFUL [Di88]. The efficiency has been calculated for neutrons for the pulse height threshold of 2.5 MeV up to 250 MeV and has been empirically corrected between 20 MeV and 60 MeV [No11]. NE213 has an estimated 5% uncertainty in its calculated efficiencies [Bu14].

At low energies, the NE213 detector efficiencies are not accurate thus the spectrum is suggested to be cut below 10 MeV [Bu14]. Fortunately, the energies of interest are above 10 MeV.
As shown in Figure 34, efficiency rises rapidly in the threshold region and makes a low energy peak around 10 MeV. This region is dominated by n-p scattering and as its cross section decreases so does the detector efficiency. The second peak around 30 MeV

corresponds to the rising cross sections of neutrons on carbon. Afterwards, the fall of the efficiency corresponds to the fall of the total cross sections [Ce79]. There is reasonable agreement between the calculated efficiencies using different codes as shown in Figure 34.

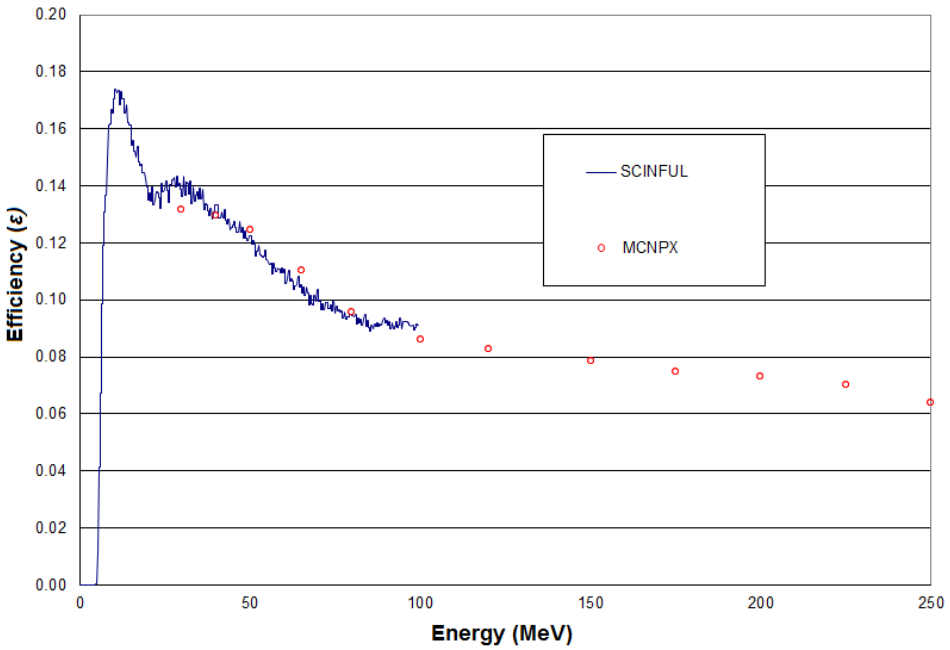

Figure 34: *Efficiency of the NE213 detector for a detection threshold of 2.5 MeV, calculated using SCINFUL and MCNPX.*

The efficiency of the NE213 detector was calculated [Bu14] using both the codes SCINFUL and MCNPX (see Figure 34) in order to cover the full energy range of interest. These data were combined to provide the recommend curve for the efficiency of the detector (Figure 35). The calculations include the most recent cross sections of neutron interactions on carbon [Bu14], relativistic kinematics, and the correct determination of energy deposited by charged-particle recoils which escape the detector.

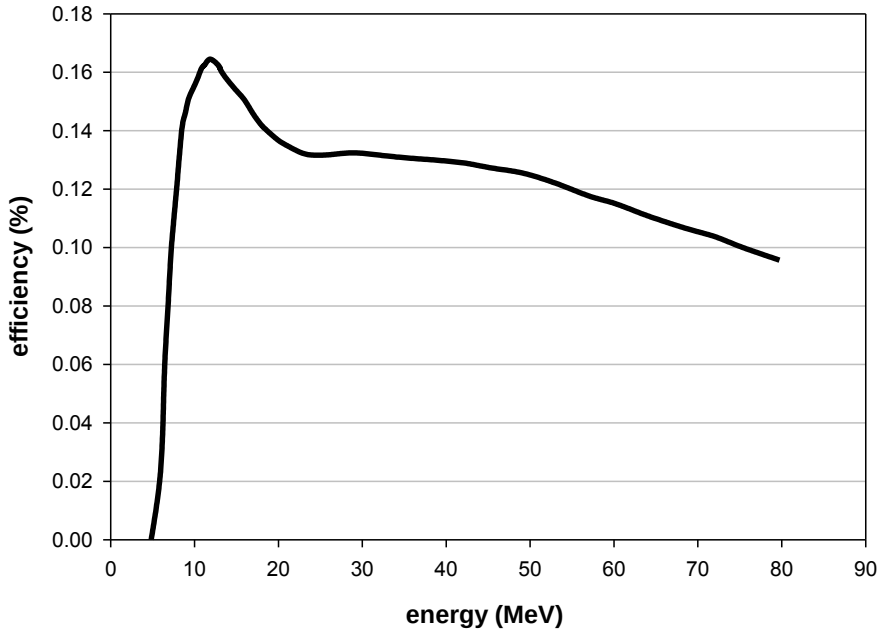

Figure 35: *Efficiency of the NE213 detector for a detection threshold of 2.5 MeV, determined from the combined SCINFUL and MCNPX data in Figure 34.*

ii) Dead time correction.

For very high neutron fluxes, the average times between pulses will be smaller than the time required by the system to process the pulses. So it is desirable that the system is turned off once the event is detected and being analysed. This means other true events will be rejected making the measured counts less than the actual counts. In this particular experiment, the total dead time had contributions from different components. The NE213 detector, the PSD system and the ADC conversion time, all contribute to the dead time effects. The number of CFD events and the number of DAQ trigger were recorded on scalers, therefore the total dead time (DT) could be estimated during the experimental run and displayed as a percentage of the live time of the system in the data acquisition system. The maximum was about 0.25%, which is 0.0025, this value makes the correction negligible.

iii) Neutron beam attenuation

The neutron beam attenuation factor k_{att} is defined as $k_{att} = \exp(\Sigma_a(d - d_{ref}))$, where d is the distance traversed by the neutron from the actual point to the actual point of the detector, and d_{ref} is the distance from the centre of the target to the detector. For a 1 mm (0.001 m) thin target, neutrons are traversing from the same point in the target and therefore d - d_{ref} is close to 0 then k_{att} correction is negligible.

For a thick target; neutrons scatter and lose energy as they traverse through the target towards the detector. The neutron attenuation correction is explained in section 5.2.1.

iv) The slewing effect (time walk)

The rise time of the CFD pulses was measured to be less than 1 ns. No slewing effect was evident in the time-amplitude distributions, and thus no correction was necessary.

4.3.3 The comparison of manual ^{7}Li spectrum to the spectrum reduced using the c++ (Neutron Energy Spectrum Reduction - NESR) code

In section 3.3.1, energy spectra were produced in two ways, manually and automatically respectively. Having corrected these spectra for detector efficiency and normalised them as per charge and angle, it was necessary to compare the two methods and, in particular, to validate the reduction method using the NESR code. Figure 36 demonstrate these two methods. There is a good agreement especially in the low-energy tail. In the peak region, the slight difference comes from rebinning.

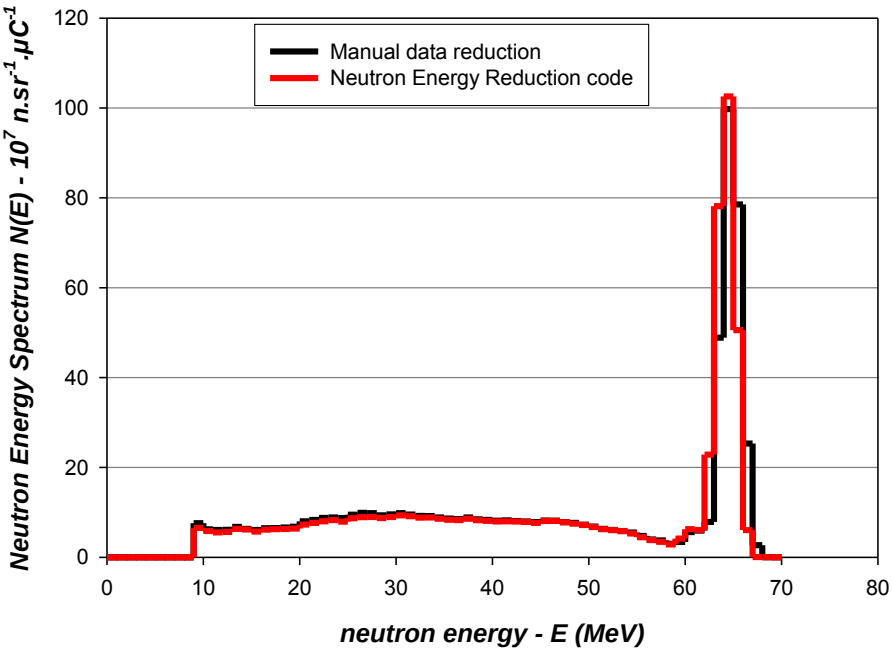

Figure 36: *The two spectra reduced manually and automatically using the Neutron Energy Reduction code are compared.*

4.3.4 The comparison of this work's ^{7}Li spectrum to the previous work

The spectral fluence of ^{7}Li measured in this work at 0° is compared to the measurement of relative spectral fluence of Mosconi *et al*. [Mo10], who used a similar target and energy, but

a different thickness of 5 mm. For proper comparison, the measured ^{7}Li spectrum of 2.5 ± 0.5 mm thickness was scaled to 5 mm thickness. This was achieved by adding the measured 2.5 ± 0.5 mm thickness of ^{7}Li spectrum to an interpolated ^{7}Li spectrum of 2.5 mm thickness. The interpolation was carefully done using the measured spectrum from the ^{7}Li target of 2.5 ± 0.5 mm thickness at 66 MeV and 54 MeV. The total spectrum (2.5 mm + 2.5 mm) was corrected for the proton energy losses as well as the 1% neutron losses due to scattering. See the comparison in Figure 37. The agreement in spectral shape is clear, as well as in the low energy tail. In the peak region, the difference is, amongst other things, due to the slight differences in proton beam energy, determination of the position of the prompt gamma-ray peak and target thickness. The peak-to-total ratio for Mosconi *et al*. was measured to be 0.41 ± 0.04 whereas for this work's peak-to-total ratio was measured to be 0.44 ± 0.02. The agreement in the shape of the spectra, in particular the peak-to-total ratio is encouraging. The absolute spectral fluence is compared with earlier measurements in section 4.5.

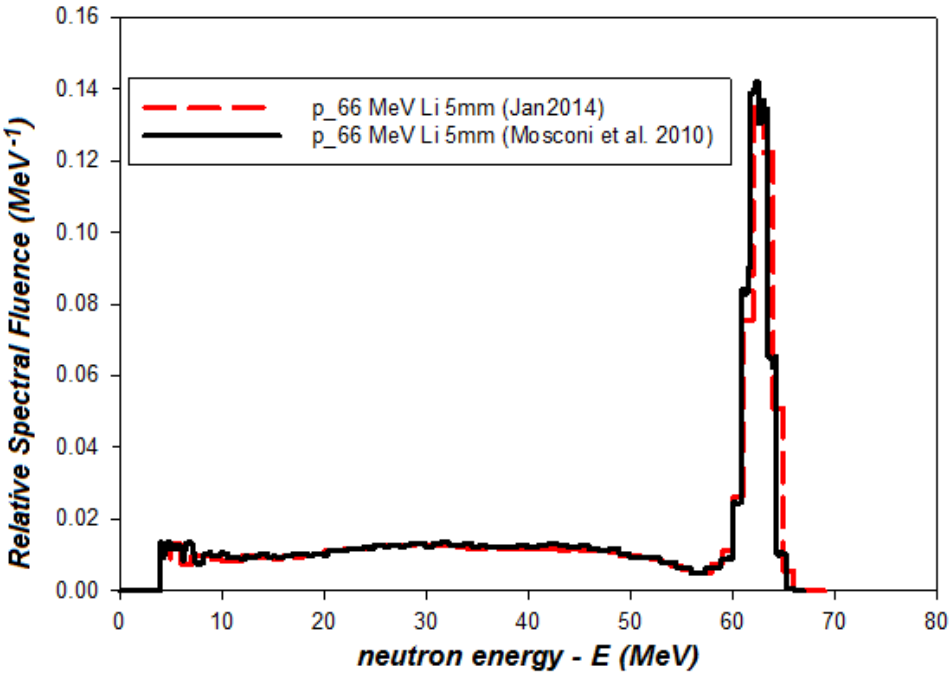

Figure 37: *The experimental relative neutron spectral fluence of 66 MeV protons on 5 mm thick ^{7}Li target is compared to a 66 MeV protons on 5 mm thick ^{7}Li target by Mosconi et al. [Mo10].*

4.4 Measured neutron spectra from thin targets (^{7}Li).

For both targets, the energy spectra of four energies at angles of 0° and 16° are compared to demonstrate the dependence of the spectrum on incoming proton energy. Figure 38 and

Figure 39 shows the measured neutron spectra from proton beam energies of 66; 54; 42 and 30 MeV on the 2.5 ± 0.5 mm ^{7}Li target at angles of 0° and 16° respectively.

The relative uncertainties in these neutron energy spectra are calculated using equation (9) and are found to be 18%, mostly due to the NE213 detector which has an estimated 5% uncertainty on its efficiency calibrations [Bu14] and from the target thickness of ^{7}Li which was estimated to be 17%. The uncertainties that are contributed by other corrections and normalisations are relatively small. They include i) the total charge (Q) from the Charge Integrator which has an estimated 0.1% relative uncertainty [Sm16]; ii) the solid angle has an estimated 0.32% relative uncertainty; iii) and the number of counts N per bin has a relative uncertainty given by $1/\sqrt{N}$. Also, since ^{7}Li data will later be compared to Baba *et al*. [Ba99], which means equation (8) needs to be corrected to the desired target thickness of comparison, therefore lithium target thickness uncertainty needs to be factored in.

$$\frac{\delta N(E)}{N(E)} = \sqrt{\left(\frac{\delta\varepsilon}{\varepsilon}\right)^2 + \left(\frac{\delta Q}{Q}\right)^2 + \left(\frac{\delta N}{N}\right)^2 + \left(\frac{\delta\Omega}{\Omega}\right)^2 + \left(\frac{\delta Li_t}{Li_t}\right)^2 + \left(\frac{\delta k_{dt}}{k_{dt}}\right)^2 + \left(\frac{\delta k_{att}}{k_{att}}\right)^2} \quad (9)$$

where $\frac{\delta N(E)}{N(E)}$ is the relative uncertainty of normalised counts in the neutron energy spectrum; $\frac{\delta\varepsilon}{\varepsilon}$ is the relative uncertainty of the NE213 detector efficiency values; $\frac{\delta Q}{Q}$ is the uncertainty of the total beam charge; $\frac{\delta N}{N}$ is the relative uncertainty of counts in the neutron energy spectrum before normalisation; $\frac{\delta\Omega}{\Omega}$ is the relative uncertainty of the solid angle and $\frac{\delta Li_t}{Li_t}$ is the relative uncertainty of the lithium target thickness; $\frac{\delta k_{dt}}{k_{dt}}$ is the relative uncertainty of the dead time factor; and $\frac{\delta k_{att}}{k_{att}}$ is the relative uncertainty of the neutron attenuation. The dead time correction and neutron attenuation are both negligible and therefore k_{dt} and k_{att} were not considered.

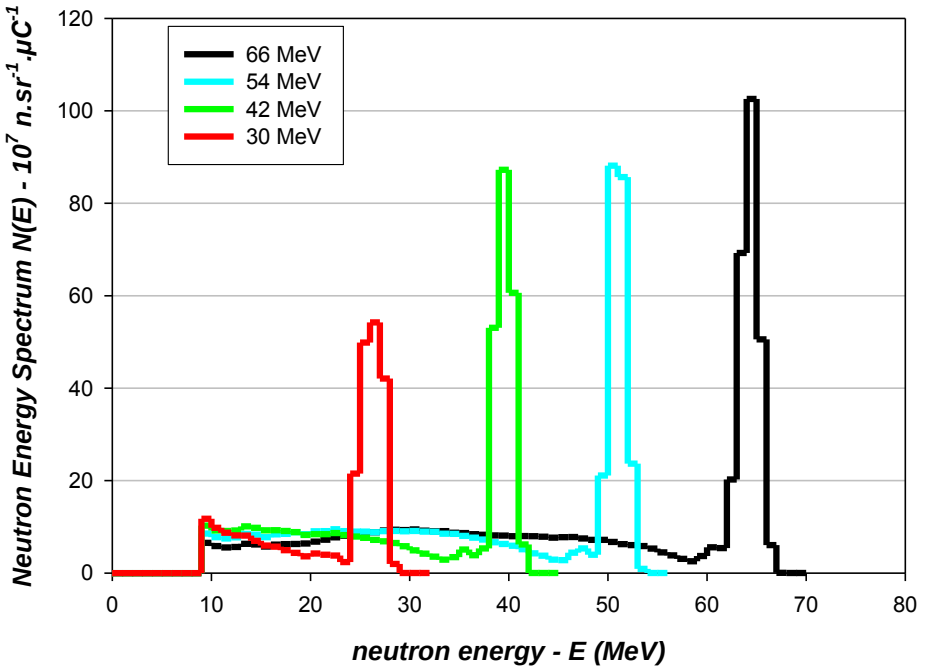

Figure 38: *The normalised neutron energy spectra of protons on 2.5 ± 0.5 mm thick ^{7}Li at 66; 54; 42 and 30 MeV energies at 0˚.*

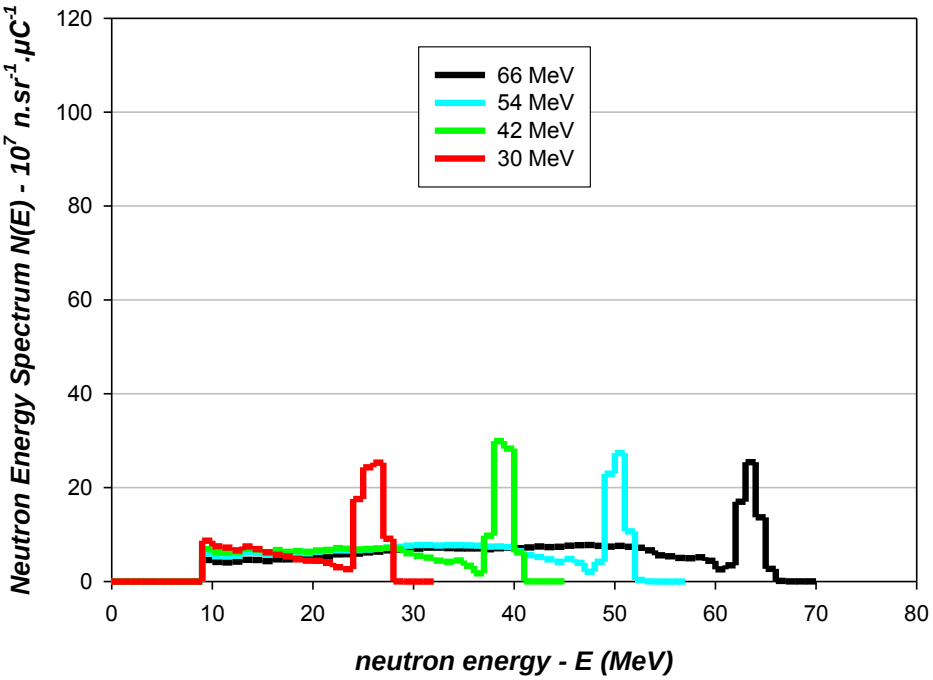

Figure 39: *The normalised neutron energy spectra of protons on 2.5 ± 0.5 mm thick ^{7}Li at 66; 54; 42 and 30 MeV energies at 16˚.*

4.5 Previous measurements of the ^{7}Li(p,n)^{7}Be cross section.

In the case of the ^{7}Li target, the peak in the spectrum has unresolved contributions from the ground state and first excited state at 0.478 MeV. The data for this combined peak was summarized by Baba *et al*. [Ba99]. Figure 40 shows data points of cross sections (dσ/dΩ) in mb/sr for the ^{7}Li(p,n)^{7}Be reaction between 0 and 100 MeV at 0°, measured at different facilities.

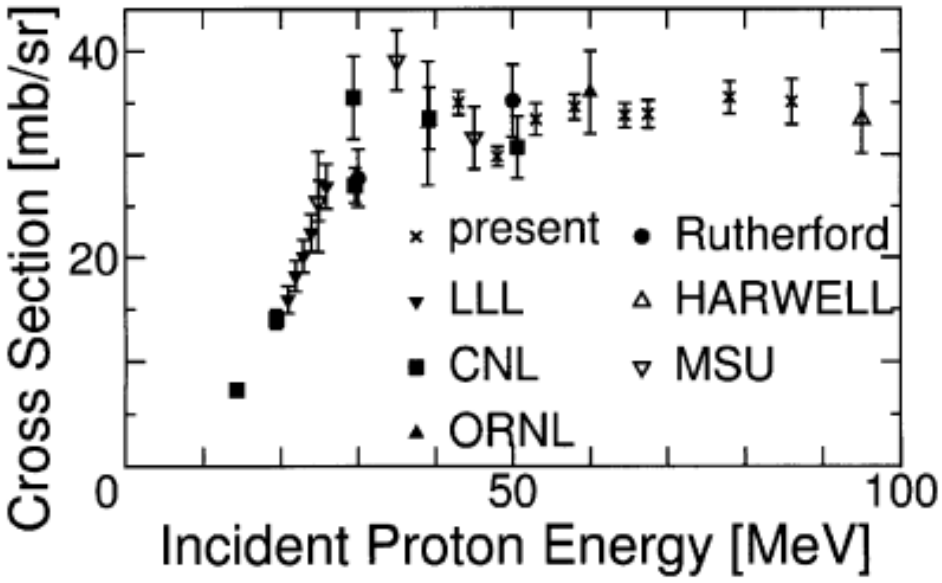

Figure 40: *From Baba et al. [Ba99]. Cross sections of the reaction ^{7}Li(p, n)^{7}Be for incident proton energies between10 MeV and 100 MeV as measured by Baba et al. ("present") and earlier workers. This reaction is observed from the unresolved ground state and first excited state.*

While the cross section of the ^{7}Li(p,n)^{7}Be reaction at zero degrees increases sharply up to about 35 millibarns by 30 MeV, beyond this, the cross section does not change significantly as the proton beam energy increases. At 70 MeV, the cross section is still below 40 millibarns. At low energies, the (p, n) reaction dominates the (p, 2n) and (p, 3n) channels. The kinematics of the two or more released neutrons means the energy is shared amongst them. Thus, at higher energies, the (p,2n) and (p,3n) reactions contribute to the low energy tail in the neutron spectrum [Vr12].

In the present measurements, the (p,n) cross sections of ^{7}Li, (dσ*(E)*/dΩ) in mb/sr, were deduced from the thin target neutron fluence spectrum. This was done for the four energies (66, 54, 42 and 30 MeV) that were measured. The RadWare program [Ra95] was used to fit the area under the peaks. Therefore four values were obtained at 0°. For the purposes of

comparison with available data, these values were normalised to millibarns (mb) per unit angle in steradians (sr) using equation (10)

$$\frac{d\sigma(E)}{d\Omega} = A_{peak}\frac{10^{27}\times 1.602\times 10^{-19}}{N_a Q\Omega} \text{ mb} \qquad (10)$$

where A_{peak} is the area under the peak in the neutron energy spectrum; 10^{27} is a scaling factor (millibarns); 1.602X10^{-19} is the charge in coulombs; N_a is the number of atoms in the target per unit area in cm^2; Q is the total proton charge in the beam in coulombs and Ω is solid angle subtended by the NE213 detector (sr).

The relative uncertainties of the cross sections were calculated using equation (11).

$$\frac{\delta\sigma(E)}{\sigma(E)} = \sqrt{\left(\frac{\delta A_{peak}}{A_{peak}}\right)^2 + \left(\frac{\delta N_a}{N_a}\right)^2 + \left(\frac{\delta Q}{Q}\right)^2 + \left(\frac{\delta\Omega}{\Omega}\right)^2 + \left(\frac{\delta Li_t}{Li_t}\right)^2} \qquad (11)$$

Figure 41 presents the comparison of cross sections (laboratory frame) of this work to the work done by Baba *et al*. [Ba99]. The agreement is good within uncertainties. The uncertainties should in the plot arise predominantly from the uncertainty in the lithium target thickness (2.5 ± 0.5 mm).

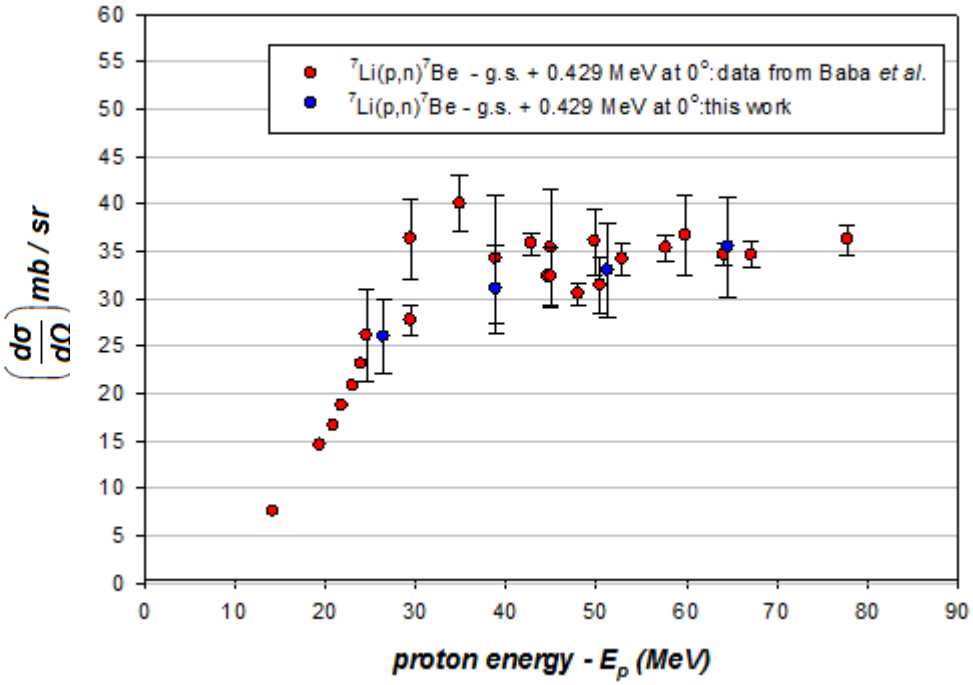

Figure 41: *Cross sections (laboratory frame) of ^{7}Li(p,n)^{7}Be reaction from this work are compared to those of Baba et al. Average proton energies are plotted here, see Table 5.*

The agreement with previous measurements gives confidence in the way the experiment was conducted as well as the correctness of the procedure of the data analysis.

The next chapter will present the measured ^{18}O results and will also explore whether the Monte Carlo codes can reproduce the measured spectra.

CHAPTER 5: RESULTS AND DISCUSSION

5.1 Neutron spectra measured from the thick and thin ^{18}O targets.

The measurements with the ^{18}O target that were performed at different energies, are summarized in Table 4, with the corresponding beam parameters and settings.

Table 4: Summary of beam energies, radio frequencies, beam profiles.

E_p (MeV)	Target	Pulse selector	Radio Frequency - RF (MHz)	Selected RF (MHz)	Pulse separation (ns)
66.0 ± 0.8	Thin ^{18}O-water	1:5	16.374	3.275	305.4
54.0 ± 0.8	Thin ^{18}O-water	1:5	14.943	2.989	334.6
42.0 ± 0.8	Thin ^{18}O-water	1:5	13.298	2.660	375.1
30.0 ± 0.8	Thin ^{18}O-water	1:5	11.343	2.269	440.8
62.0 ± 0.8	Thick ^{18}O-water	1:5	15.917	3.183	307.2

5.1.1 Results of measured neutron spectra from thin targets (^{18}O).

Table 5 shows the expected centroid of the monoenergetic peak in the neutron energy spectrum produced by proton beams of 66, 54, 42 and 30 MeV on an ^{18}O-water target of 1.9 ± 0.1 mm thickness. The centroid values agree within one standard uncertainty when compared to the centroid from the measured neutron energy spectra.

Table 5: Comparison of calculated centroids to the measured centroids of proton beams of 66, 54, 42 and 30 MeV on an ^{18}O-water target of 1.9 ± 0.1 mm in thickness.

E_p (MeV)	Target (1.9 mm)	Proton energy at the centre of the target (MeV)	Expected neutron peak energy (MeV) Q = - 2.4 MeV	Measured neutron peak energy (MeV)
66.0 ± 0.8	^{18}O-water	65.1 ± 0.8	62.6 ± 0.8	63.6 ± 0.5
54.0 ± 0.8	^{18}O-water	52.9 ± 0.8	50.5 ± 0.8	50.2 ± 0.5
42.0 ± 0.8	^{18}O-water	40.6 ± 0.8	38.2 ± 0.8	38.7 ± 0.5
30.0 ± 0.8	^{18}O-water	28.2 ± 0.8	25.8 ± 0.8	25.0 ± 0.5

Figures 42 and Figure 43 show the measured neutron spectra from proton beam energies of 66; 54; 42 and 30 MeV on the thin ^{18}O-water target at angles of 0° and 16° respectively.

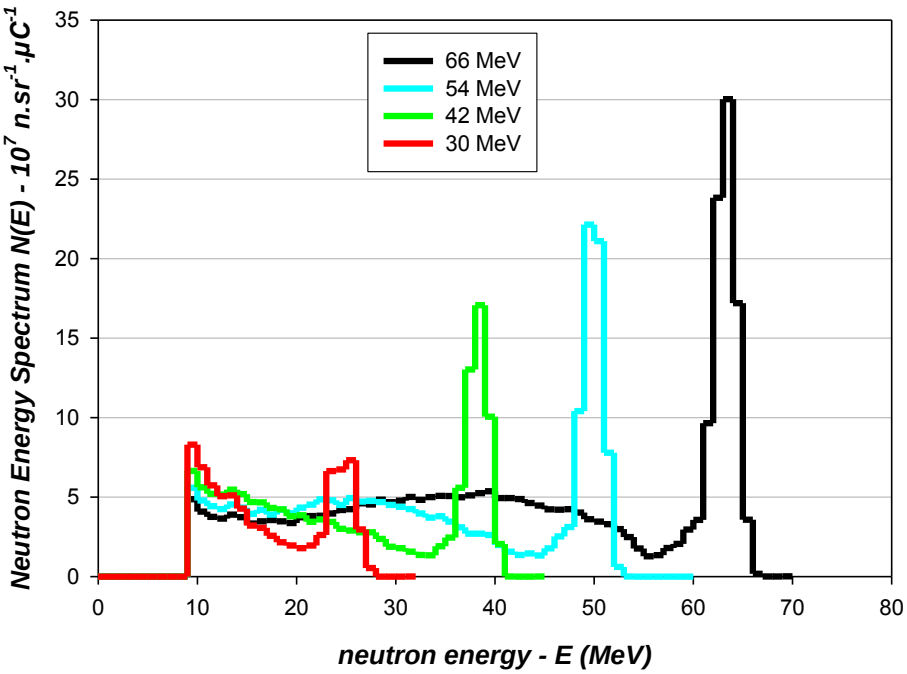

Figure 42: *The normalised neutron energy spectra of protons on a thin ^{18}O-water target at 66; 54; 42 and 30 MeV energies at 0˚.*

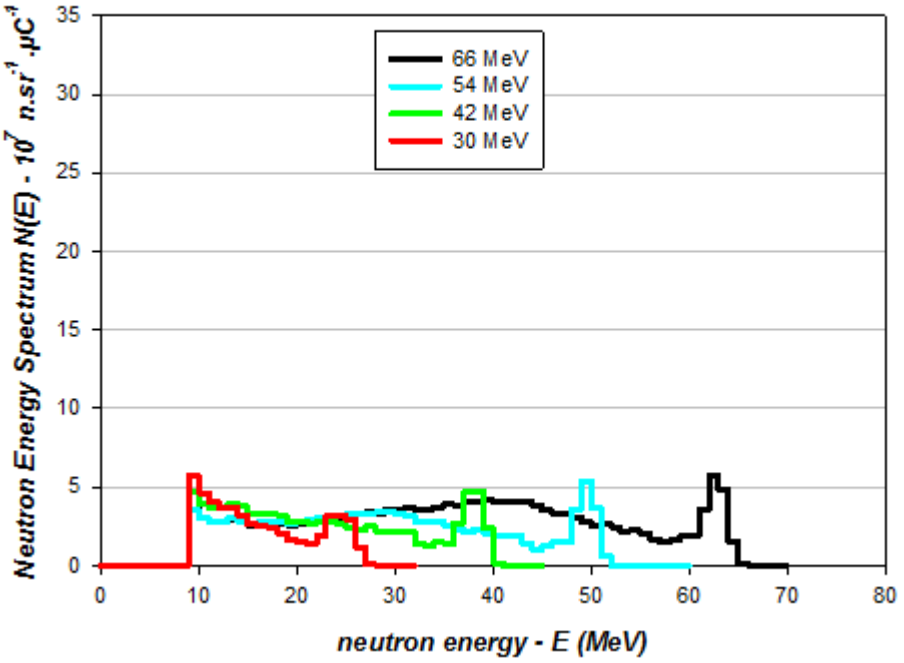

Figure 43: *The normalised neutron energy spectra of protons on a thin ^{18}O-water target at 66; 54; 42 and 30 MeV energies at 16˚. The actual target thickness is 2.03 mm (see section 5.2.3).*

5.1.2 Results of measured neutron spectra from a thick ^{18}O-water target.

Figure 44 shows the measured neutron spectra from the thick ^{18}O-water target measured at angles 0° and 16°. Unlike the thin target results, the spectra from the stopping-length thickness targets are continuous with no peaks evident.

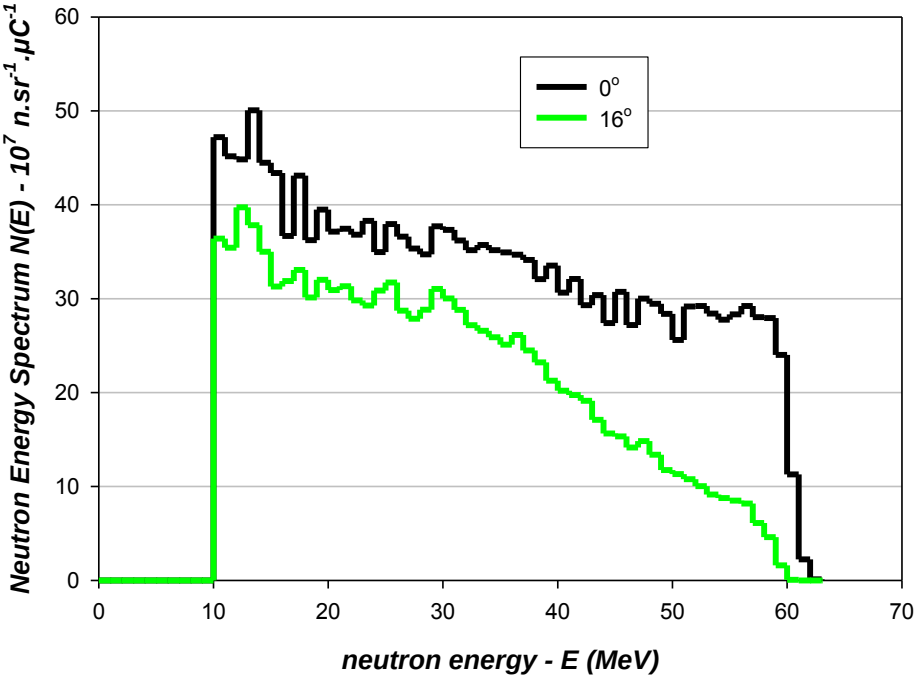

Figure 44: *The neutron energy spectra produced by 62 MeV protons on an ^{18}O-water target of thickness 40.0 ± 0.1 mm, measured at 0˚ and 16˚.*

5.2 Empirical simulation of thick target spectrum using thin target data.

In order to understand the shape of the thick target spectrum, and as a check of the thickness of the thin target, the thick target spectrum was simulated, empirically, using the thin target spectra. To do this, the thick target would ideally be divided into infinitesimal slices. Spectra corresponding to the appropriate proton energy would be allocated to each slice, and would be summed to produce the total spectrum.

In practice, we could only use a finite number of slices, and we had only measured thin target yields at four energies. As a result, for the purpose of the simulation, the target was divided into twenty slices of 2.0 mm thickness (approximately the same as the thin target thickness). Interpolated (and extrapolated) neutron energy spectra were generated based on

the four measured thin target yields. These energy spectra obtained by interpolation and extrapolation will be referred to as “empirically simulated” spectra.

5.2.1 Detailed description of interpolation and extrapolation procedure.

The thick target spectra for both angles of 0° and 16° were simulated by summing interpolated or extrapolated spectra derived from the measured spectra of thin targets, which are shown in Figure 45, for 66, 54, 24 and 30 MeV.

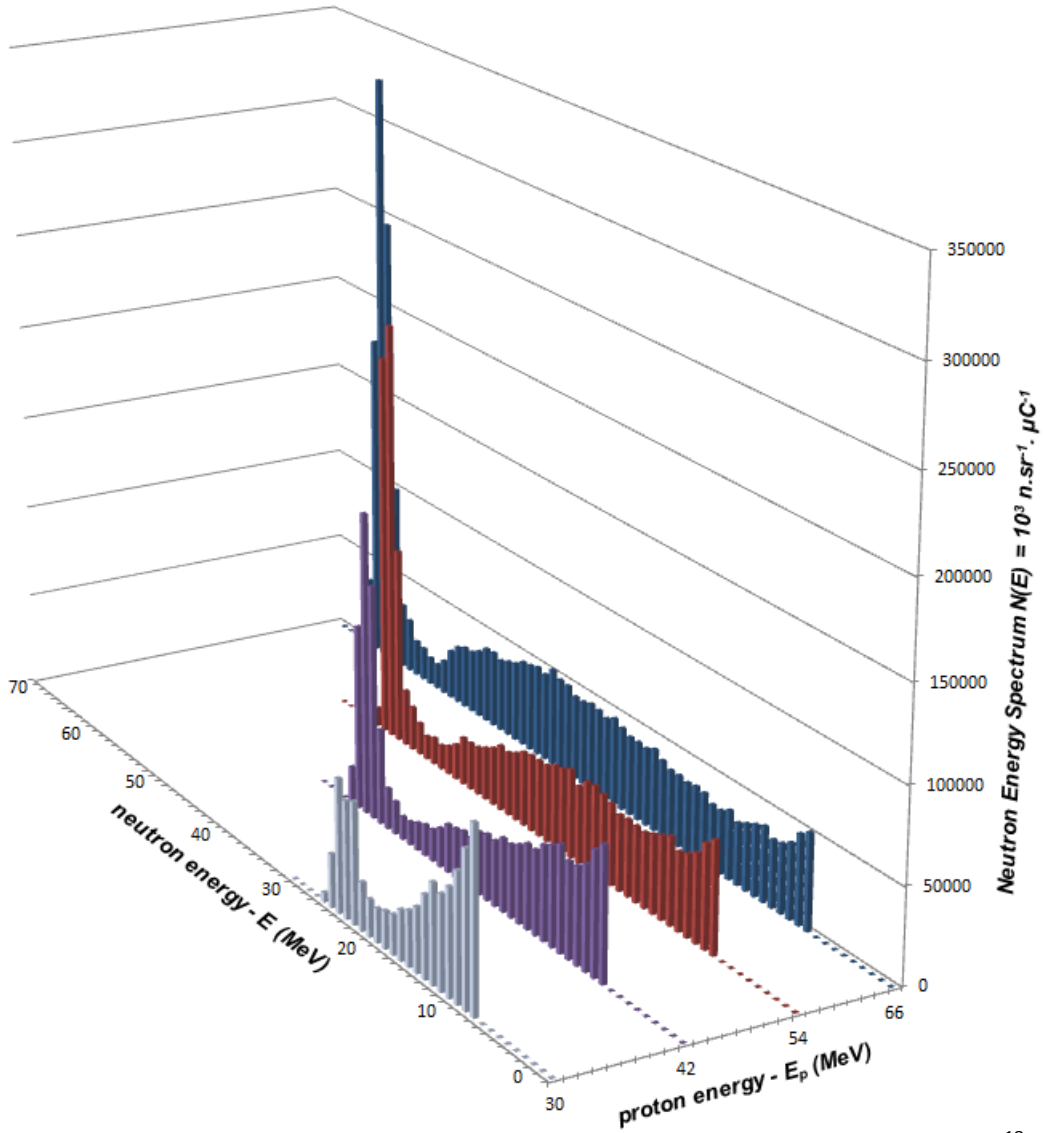

Figure 45: *The four neutron energy spectra shown are produced by protons on a ^{18}O-water target of thickness 2 mm at 66; 54; 42 and 30 MeV energies at 0°. They were used to interpolate and extrapolate new spectra for a thick target of 40.0 ± 0.1 mm subdivided into 2.0 mm slices.*

All the neutron spectra from the four different energies, shown in Figure 45, have an unequal number of channels between the peak and the 10 MeV cut-off, which does not allow the channels of the 66, 54, 42 and 30 MeV spectra to match for the purposes of interpolation. Therefore, the energy spectra were rebinned for them to have an equal number of channels up to the peak. The number of required bins for each of the four spectra was set to 66 bins. This was achieved by introducing factors to stretch and rebin the energy spectrum in the kinetic energy formula in the NESR code. This factor is the ratio of required number bins (66) to neutron maximum energy in that measurement. For example, a factor 66/50.2 was used to rebin the 54 MeV energy spectra; 66/38.7 was used for the 42 MeV spectra and 66/25 for 30 MeV. Intervening spectra were then linearly interpolated on a channel by channel basis. They were then compressed back to their original energy dispersion to produce a complete set of spectra, in steps of 1.0 MeV beam energy.

Since the measured thin targets were 1.9 ± 0.1 mm thick, the modelled thick target of 40 mm was subdivided into 20 slices of 2 mm in thickness. Average beam energies calculated with the SRIM2008 code [Zi08], for each subdivision, are written in red in Figure 46.

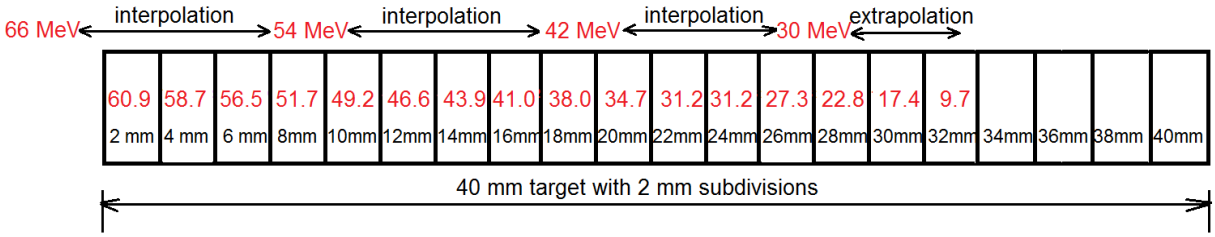

Figure 46: *The schematic diagram of the thick ^{18}O-water target with 2 mm subdivision. The red numbers show the calculated average proton energy loss in each disk as protons traverse from disk 1 towards disk 40.*

These average energy calculations are presented in Table 6. The average energy values were used to match and select the neutron spectra which were summed.

For the thick target, neutrons scatter and lose energy as they traverse through the target towards the detector. According to the target geometry, neutrons detected at 16˚ are understood to have traversed through the side of the target and through same thickness of target regardless of their origin along the beam direction in the target. This is different for neutrons detected at 0˚, as neutrons created at different points in the target will traverse through different target thickness, making the correction more complex.

Table 6: The average energy (E_{ave}) calculated for the 2 mm subdivisions of the thick target.

Subdivision (mm)	E_{in} (MeV)	E_{out} (MeV)	E_{ave} (MeV)
2	62.00	59.84	60.92
4	59.84	57.62	58.73
6	57.62	55.33	56.48
8	55.33	52.97	54.15
10	52.97	50.51	51.74
12	50.51	47.96	49.24
14	47.96	45.29	46.63
16	45.29	42.49	43.89
18	42.49	39.53	41.01
20	39.53	36.39	37.96
22	36.39	33.00	34.70
24	33.00	29.31	31.16
26	29.31	25.19	27.25
28	25.19	20.41	22.80
30	20.41	14.46	17.44
32	14.46	4.95	9.71

The four measured neutron spectra were matched to the average thickness of the remaining subdivisions in the thick target. The energy-dependent attenuation of the neutrons through the remaining target material was estimated using MCNPX, and the neutron spectra were modified accordingly.

There were four neutron energy spectra measured at 66; 54; 42 and 30 MeV for both angles of 0° and 16°. For the 66, 54, 42 and 30 MeV neutron spectra, the energy ranges of neutrons to transmit are 10 MeV up to 66 MeV, 10 MeV up to 54 MeV, 10 MeV up to 42 MeV and 10 MeV up to 30 MeV respectively. Linear transmission functions were formulated for both 0° and 16°. They are an estimate of the neutron loss through the water target for each energy bin through a given target thickness. These functions were used firstly to correct for neutron losses due to in-target scattering, before linear interpolation and extrapolation was performed.

Once the linear interpolations were completed, all the spectra were rebinned into MeV bins using the RadWare program [Ra95]. All selected spectra as per energies in Table 6 for the 0° angle are shown in Figure 47.

The uncertainties in these calculations are 12%, and come mainly from the ^{18}O-water target thickness which has an estimated uncertainty of 10.5 %. The rest of the uncertainties are propagated, as explained previously, using equation (13).

$$\frac{\delta N(E)}{N(E)} = \sqrt{\left(\frac{\delta d}{d}\right)^2 + \left(\frac{\delta Q}{Q}\right)^2 + \left(\frac{\delta N}{N}\right)^2 + \left(\frac{\delta \Omega}{\Omega}\right)^2 + \left(\frac{\delta O_t}{O_t}\right)^2} \qquad (13)$$

where $\frac{\delta O_t}{O_t}$ is the relative uncertainty of the ^{18}O-water target thickness.

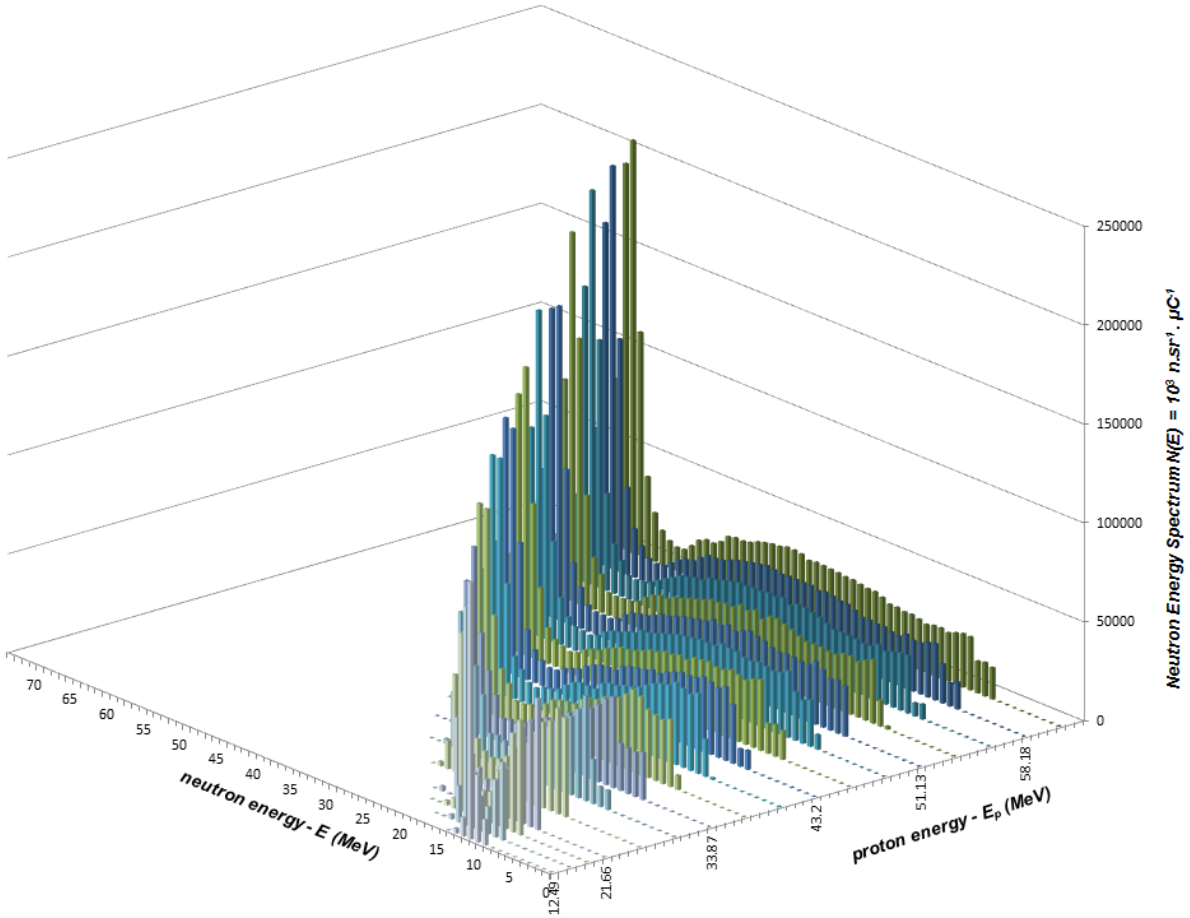

Figure 47: *The simulated neutron energy spectra using spectra from protons on a 2 mm thick ^{18}O-water target at 66; 54; 42 and 30 MeV energies at angle 0°.*

5.2.2 Neutron loss correction due to absorption and scattering.

i) Correction due to the ^{18}O-water target.

According to Figure 46, neutrons produced at different positions along the target will have to traverse through the target and will be scattered or absorbed by the $H_2{}^{18}O$ water. This effect is expected at both angles of 0° and 16°. In an MCNPX simulation (using $H_2{}^{16}O$ instead of $H_2{}^{18}O$) monoenergetic neutrons of 10, 20, 30, 40, 50 and 60 MeV were passed through different thicknesses, corresponding to the position of slices in Figure 46 to obtain the transmission fractions of these neutrons. To obtain transmission ratio in 1 MeV steps, an interpolation of these values was performed.

ii) Corrections due to the NE102 detector placed at an angle of 0°.

The NE102 scintillator is a hydrocarbon material of thickness 2.0 mm. MCNPX was used to estimate the neutron losses of monoenergetic neutrons of 10, 20, and 30 MeV passing through this material. The neutron losses at 10, 20, and 30 MeV were estimated to be 3%, 2% and 1% respectively. A linear interpolation was used to estimate the neutron losses for energies between 10 MeV and 40 MeV in the steps of 1 MeV as beyond 40 MeV the neutron loses were not as significant.

5.2.3 Comparison of the empirically simulated thick target spectra with measured spectra

This section will compare the spectra using the thickness as measured with a laser (1.9 ± 0.1 mm). Since the agreement is not accurate, the true thickness of the thin targets will be derived by fitting a normalization constant (thickness) that gives the best overlap of the measured and simulated spectra. It is this thickness that will be adopted, since the assumption cannot be made that the water pressure used for the laser measurements was precisely the same as in the in-beam measurement.

The spectra shown in Figure 47 for an angle of 0° were summed up as per corresponding energy bins. The same procedure was followed for an angle of 16°. The spectra in “red” in Figure 48 and Figure 49 are the spectra without the correction of neutron loss in the ^{18}O-water target. Results with neutron loss correction are also shown in the same Figures 48 and 49, in green. The simulated values with neutron loss correction have a total of 11% uncertainty, from which the contribution substantially is from the ^{18}O-water target thickness which has an estimated uncertainty of 10.5%.

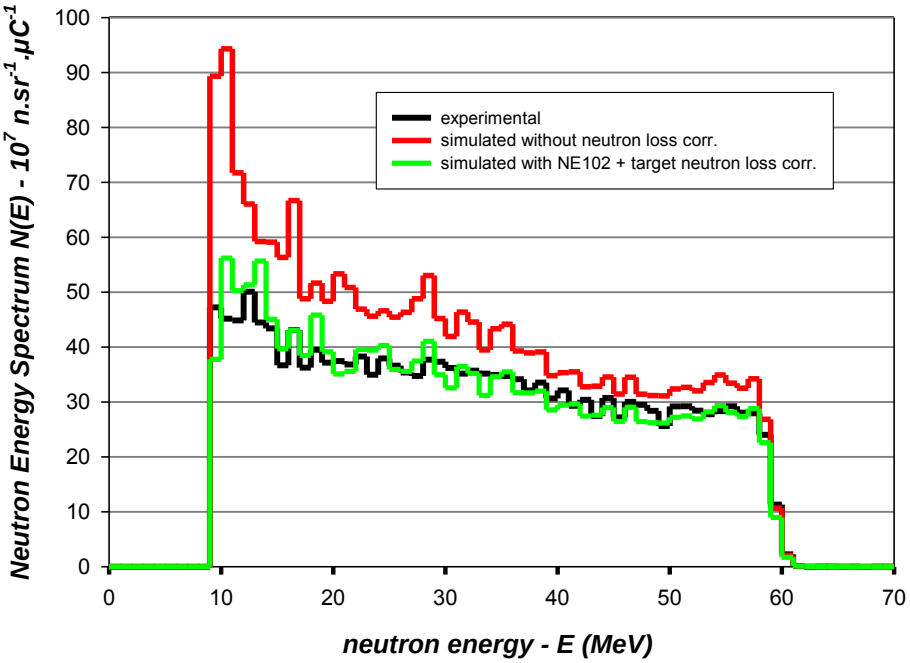

Figure 48: *Experimental ^{18}O-water thick target spectrum at 0˚ is compared to empirically simulated spectra derived from ^{18}O-water thin target data.*

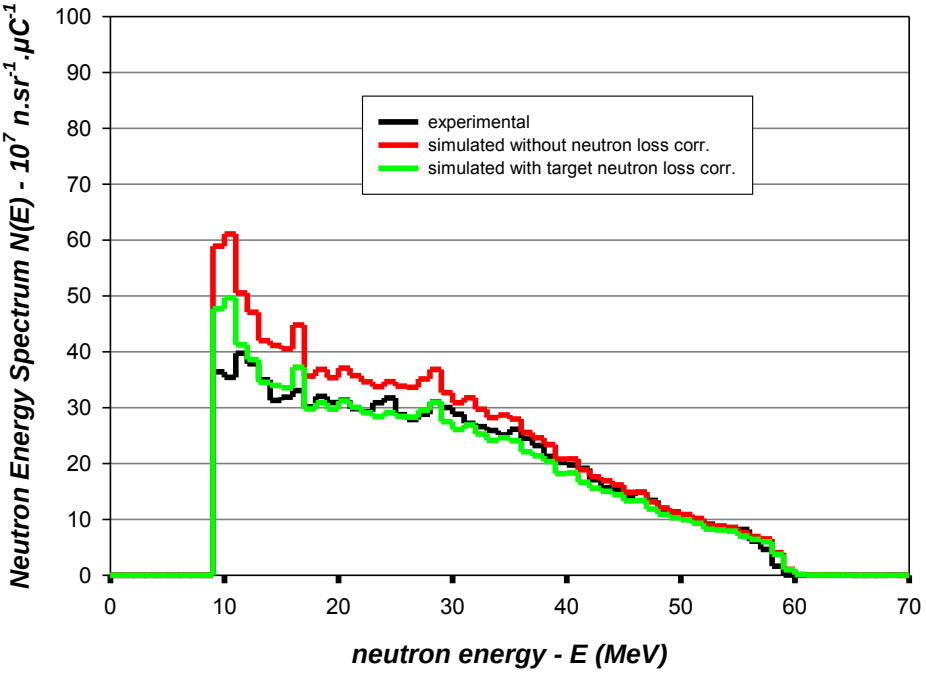

Figure 49: *Experimental ^{18}O-water thick target spectrum at 16˚ is compared to empirically simulated spectra derived from ^{18}O-water thin target data.*

Between 25 MeV and 58 MeV, a least-squares fit was undertaken, using MS Excel program, for both empirically simulated and measured spectra for both angles of 0° and 16°. The least-squares fit of the spectra at 0° gave the value 1.025 as the correction factor for the

simulated values. The least squares fit of the spectra at 16° gave the value 1.069 as the correction factor for the simulated values. The neutron-loss correction of the 16° was less complicated than the one at 0°. By kinematics analysis, neutrons at 16° did not go through much more material compared to those at 0°, which makes 16° subject to less systematic uncertainty. Therefore, the correction factor for 16° was used to correct the simulated values at both angles as it was more reliable. Therefore, the thickness of the ^{18}O-water target was determined to be 2.03 ± 0.01 mm. The corrected spectra are shown in Figure 50 and Figure 51.

The measured results of the thick ^{18}O target at 0° (Figure 50) show a good agreement with the empirically simulated spectrum above 30 MeV. Below 20 MeV, the calculated values are higher, which is likely a result of the extrapolation of spectra between 30 and 10 MeV. In this region below 30 MeV, the measured spectrum could be improved by increasing statistics, but unfortunately that will require more beam time.

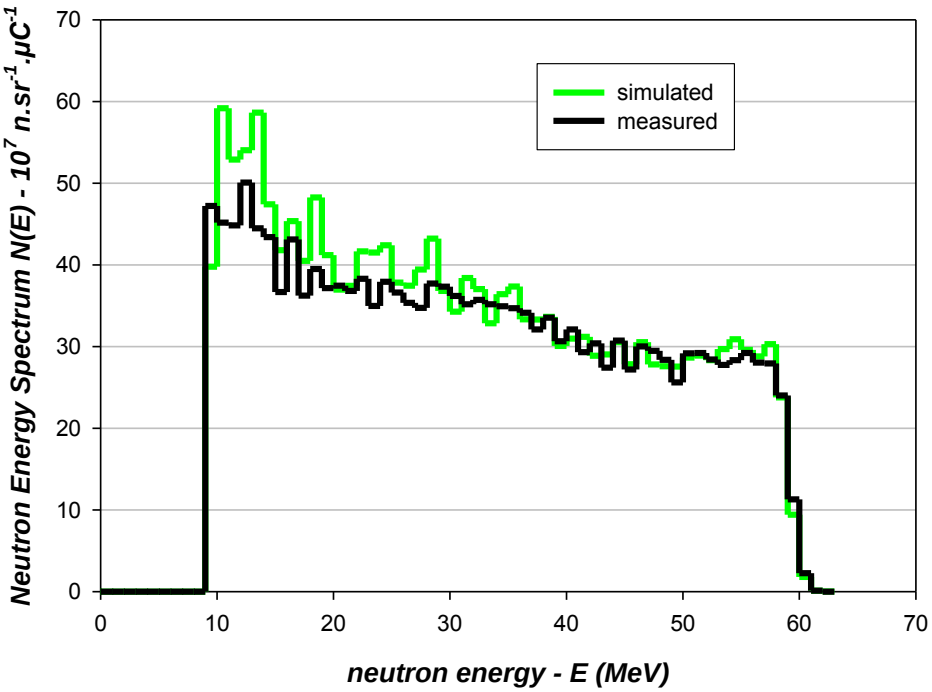

Figure 50: *The comparison of experimental neutron energy spectra of 62 MeV protons on ^{18}O-water target of thickness 40.0 ± 0.1 mm to the empirically simulated spectrum at an angle of 0˚.*

The measured spectrum of the thick ^{18}O-water target at 16° is compared to the empirically simulated spectrum in Figure 51. Above 15 MeV, the values overlap in good agreement. Below 15 MeV, again the disagreement is visible and could have the same origins as that for the 0° spectra. While at 0°, a good agreement begins above 30 MeV, at 16° it begins at 15 MeV. This better agreement is likely due to the less complex neutron loss corrections required at 16°, as neutrons emitted at 16° are transported through less target material, and of a constant thickness, compared to those emitted 0°, making corrections less complex.

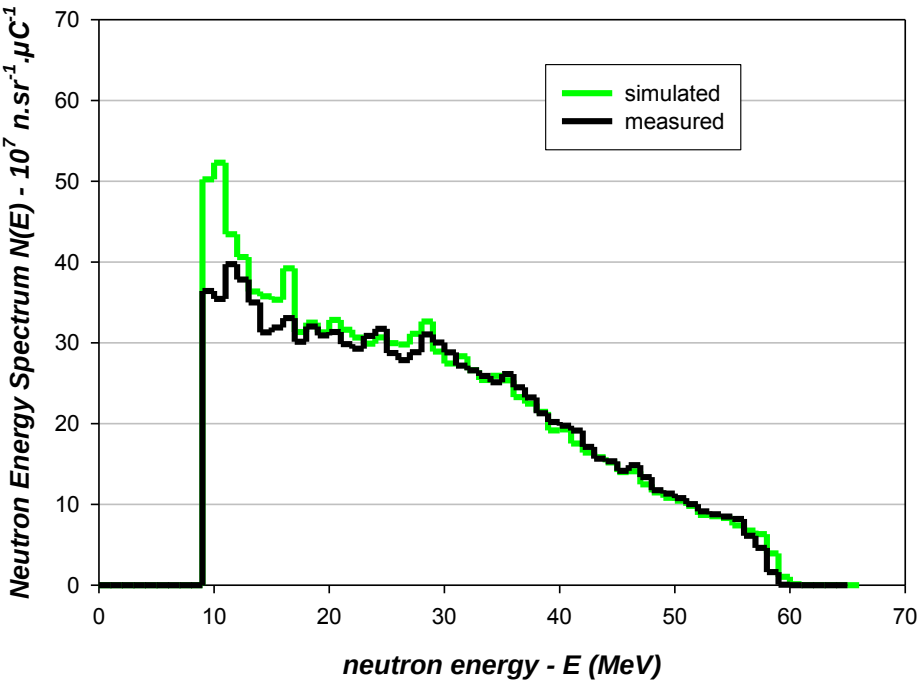

Figure 51: *The experimental neutron energy spectra for 62 MeV protons on 40 ± 0.1 mm thick $H_2{}^{18}O$ to the empirically simulated spectrum at an angle of 16˚.*

5.3 Comparison of measured spectra with FLUKA and MCNPX simulations

5.3.1 Results of calculated neutron spectra from (^{7}Li) targets using FLUKA and MCNPX code.

Since FLUKA and MCNPX are standard tools for solving radiation transport problems, including the production of neutrons, we here benchmark these codes against our results. Figure 52 shows calculations using FLUKA to predict the neutron spectra from the thin 2.5 ± 0.5 mm ^{7}Li target at 66; 54; 42 and 30 MeV at 0˚. The spectra are normalised as per the measured spectra for comparison, that is, neutrons per steradians per microcoulombs (10^7n.sr^{-1}.μC^{-1}). While the calculation does not reproduce the detailed shape of the

experimental data, there is a distinct monoenergetic peak and low energy tail. The height of the simulated peak is lower than the experimentally measured peak. The experimental data show that the peak cross sections increase with increasing energy from 30 to 66 MeV while the FLUKA results increase with increasing energy from 30 and 42 MeV and decrease with energy from 54 and 66 MeV.

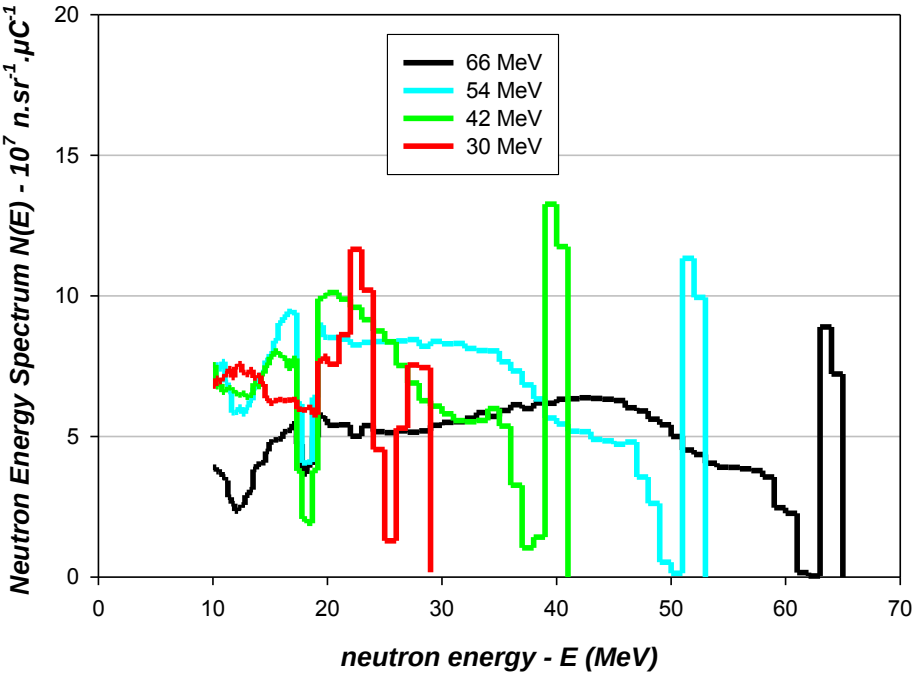

Figure 52: *Neutron energy spectra of protons on 2.5 mm thick ^{7}Li target at E_p = 66; 54; 42 and 30 MeV calculated by FLUKA at 0˚.*

Figure 53 shows calculations using FLUKA to predict the neutron spectra from the thin 2.5 ± 0.5 mm ^{7}Li target at proton energies of 66; 54; 42 and 30 MeV at 16˚. Once again the calculated and measured spectra agree with respect to the overall shape of the high energy peak and low energy tail. However, the yields of the measured neutron spectra are about six times higher than that calculated by FLUKA (see Figures 38 and Figure 39).

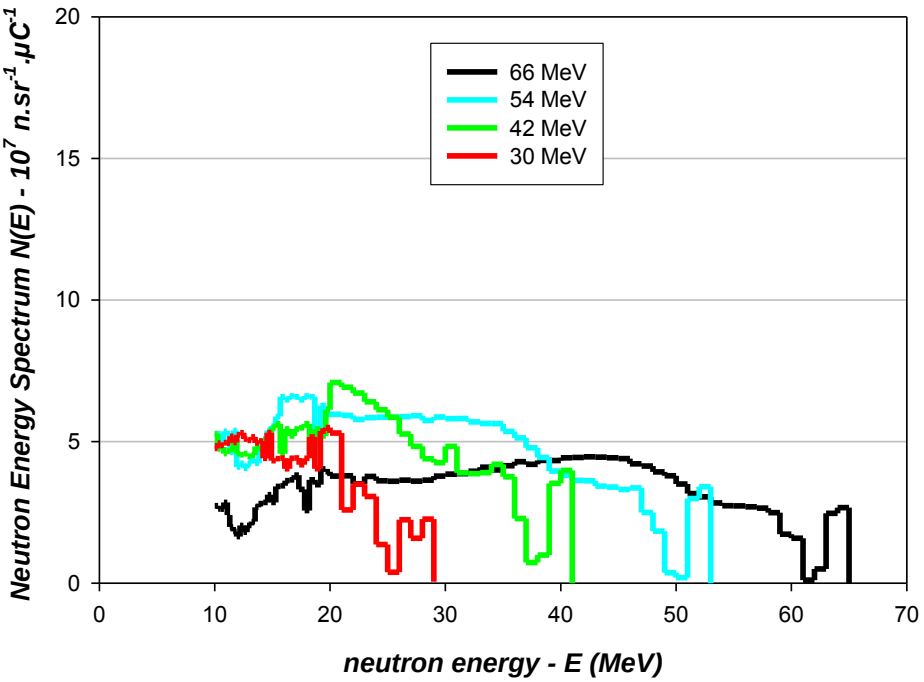

Figure 53: *Neutron energy spectra for protons on 2.5 mm thick ^{7}Li target at E_p = 66; 54; 42 and 30 MeV calculated by FLUKA at 16˚.*

The disagreement between experiment and FLUKA, see Figures 38 and Figure 52, is similar to the comparison between the MCNPX calculated ^{7}Li(p,xn) yield and the experimental ^{7}Li(p,xn) yield by Amols *et al*. (see figure 12), in the sense that FLUKA and MCNPX codes are not reliable in the energy region of interest between 30 and 66 MeV. This confirms the need for these measurements for $H_2{}^{18}O$.

Figures 54 and Figure 55 show the MCNPX calculated neutron energy spectra for protons on a 2.5 mm thick ^{7}Li target at 66; 54; 42 and 30 MeV energies at angles of 0˚ and 16˚, respectively. The spectra at angle 0˚ (Figure 54) produced an expected peak; however, contrary to the measurement, the peak heights did not increase with increasing proton energy. The spectra at angle 16˚ did not produce the distinct peak but a broad bump that decreased with energy thus failing to reproduce the measurement (see Figure 38 and Figure 39).

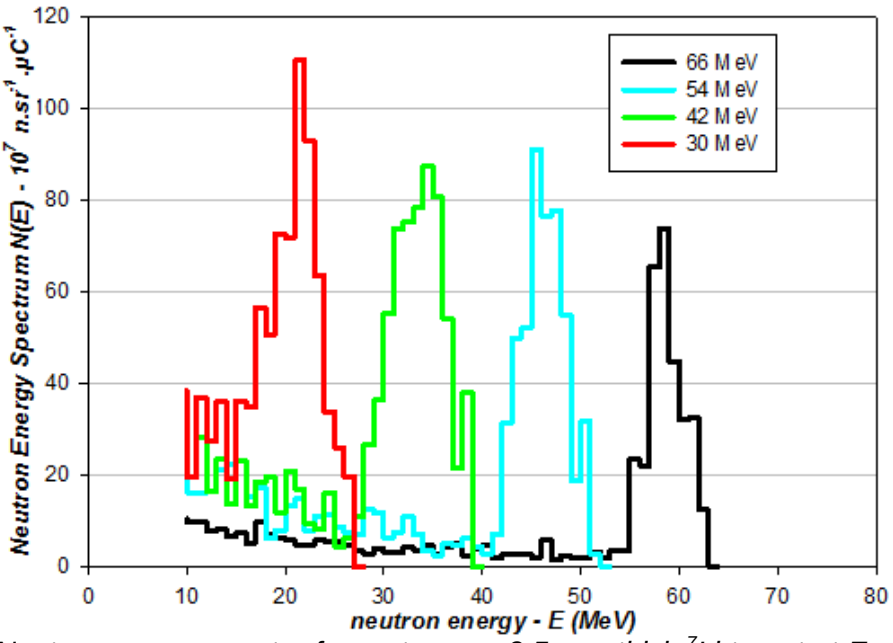

Figure 54: *Neutron energy spectra for protons on 2.5 mm thick ^{7}Li target at E_p = 66; 54; 42 and 30 MeV calculated by MCNPX at 0˚.*

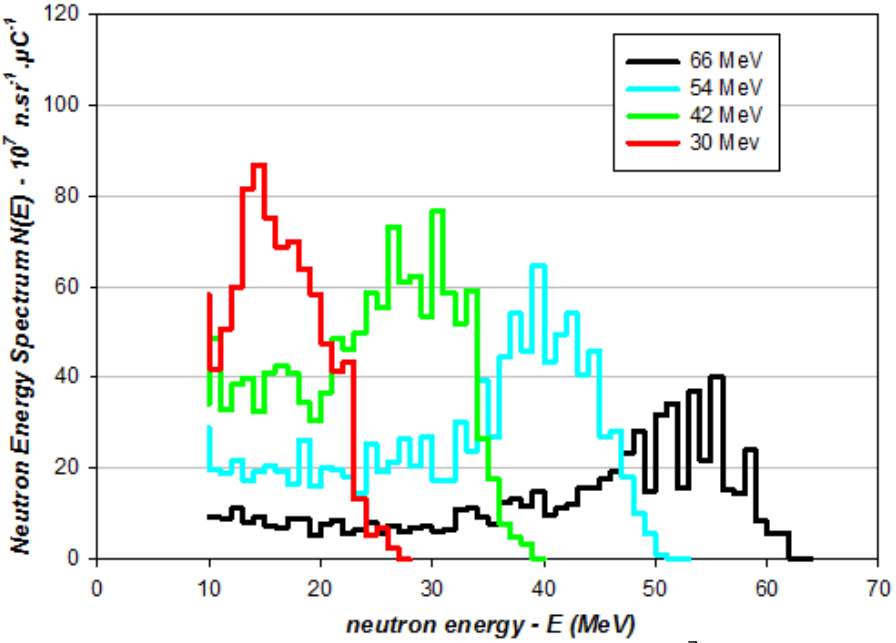

Figure 55: *Neutron energy spectra for protons on 2.5 mm thick ^{7}Li target at E_p = 66; 54; 42 and 30 MeV calculated by MCNPX at 16˚.*

5.3.2 Results of calculated neutron spectra from $H_2{}^{18}O$ thin targets using the FLUKA code.

Figures 56 and Figure 57 show calculations using FLUKA of the neutron spectra from the thin 1.9 mm ^{18}O-water target at 66; 54; 42 and 30 MeV at angles of 0˚ and 16˚ respectively. Once again, the calculation does not agree well with the measured spectra as seen in Figure

42 and Figure 43. This is probably a consequence of the unavailability of ^{18}O cross section data above 25 MeV.

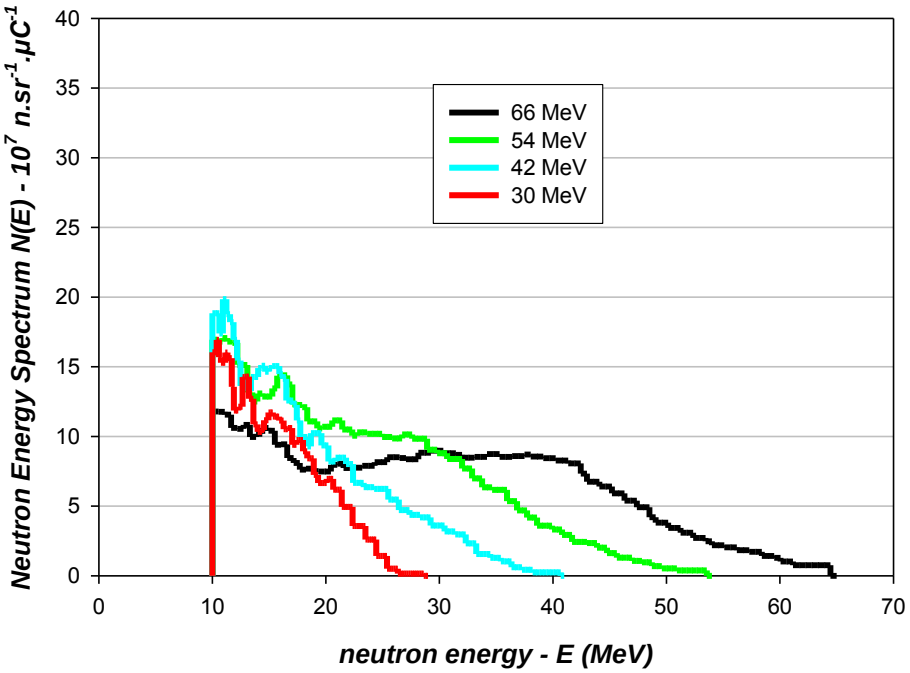

Figure 56: *Neutron energy spectra of protons on 2 mm thick $H_2{}^{18}O$ target at E_p = 66; 54; 42 and 30 MeV, calculated using FLUKA at 0˚.*

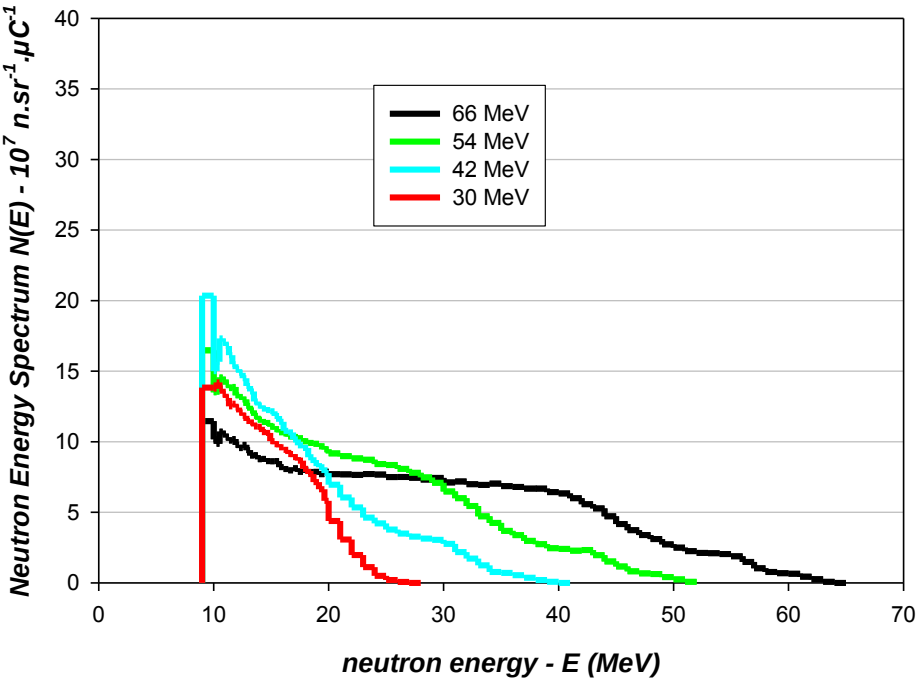

Figure 57: *Neutron energy spectra of protons on 2 mm thick ^{18}O-water target at E_p = 66; 54; 42 and 30 MeV, calculated using FLUKA at 16˚.*

The spectra that are shown in Figure 58 are calculations using FLUKA to predict the neutron spectra from E_p = 62 MeV on a 40 mm thick ^{18}O target at angle 0˚ and 16˚. Comparing these spectra to the measured spectra in Figure 44, FLUKA failed to predict the experimental data. This is, as a result, FLUKA not being able to produce peaks in the ^{18}O-water thin target spectra at both angles 0˚ and 16˚, as seen in the Figure 56 and Figure 57. Therefore, Figure 58 represents a thick spectrum that is a sum of the tail only spectrum.

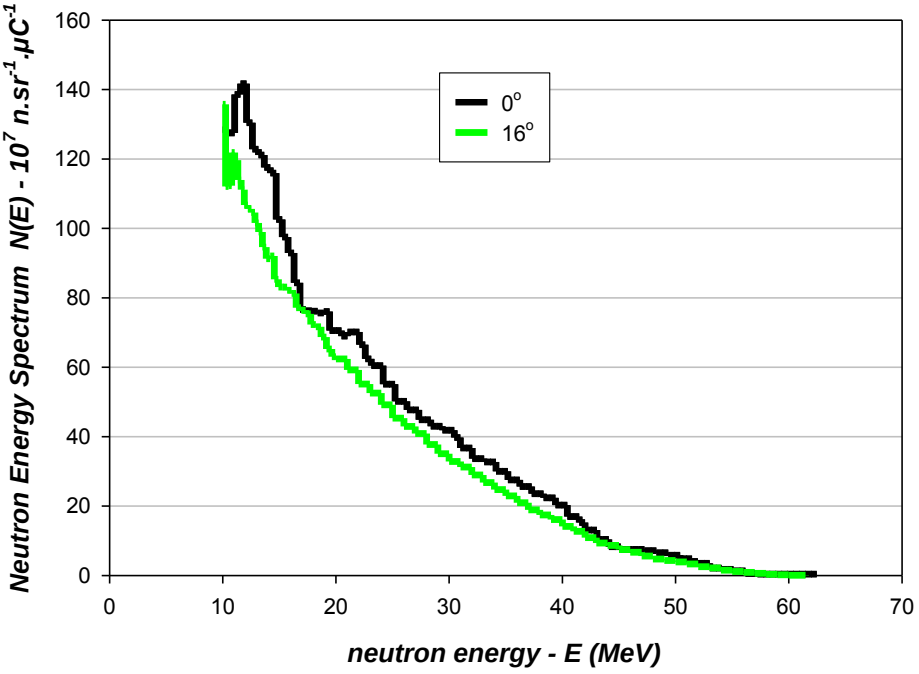

Figure 58: *The normalised neutron energy spectra for protons on 40 mm thick ^{18}O-water at E_p = 62 MeV, calculated using FLUKA at 0˚ and 16˚.*

5.4 Comparison of ^{18}O, ^{7}Li and ^{9}Be cross sections and stopping-length yields

In this section we compare ^{18}O with traditional neutron converters like ^{7}Li and ^{9}Be in terms of cross sections and stopping-length yields.

5.4.1 The (p,n) cross section spectra of ^{18}O and ^{7}Li are compared at 0° and 16°

The (p,n) cross sections (dσ/dΩ) in mb/sr of the ^{18}O peak were deduced from the thin neutron fluence spectrum the same way the (p,n) cross sections of ^{7}Li were derived (section 4.5). Here the cross sections of both angles of 0° and 16° are deduced.

Our measured cross sections for ^{18}O and ^{7}Li are compared to the cross sections for ^{7}Li and ^{9}Be from previous work. In Figure 59, this work is compared to the work compiled by Baba *et al.* [Ba99] and measurements by Jungerman *et al*. [Ju71]. Between 20 MeV and 50 MeV, the $^{18}O(p,n)$ cross sections are well below those of $^{7}Li(p,n)$ and $^{9}Be(p,n)$. In section 1.6, a reference was made to using ^{9}Be as an ideal thick target to produce neutrons with desired properties. It is then worthwhile to compare the available experimental data from ^{9}Be and ^{18}O. The $^{18}O(p,n)$ cross sections increase with increasing proton energy whereas the $^{9}Be(p,n)$ cross sections decrease with increasing proton energy, such that at the energy of interest for the iThemba LABS SAIF project, i.e. above 60 MeV, ^{18}O performs better than ^{9}Be. This is consistent with Figure 61 which shows the ^{18}O to have higher cross sections in this region. The data point of the $^{9}Be(p,n)$ cross section at 65 MeV by Kamada *et al.* [Ka11] was determined by integrating peak differential cross sections in the beryllium neutron spectrum in Figure 61.

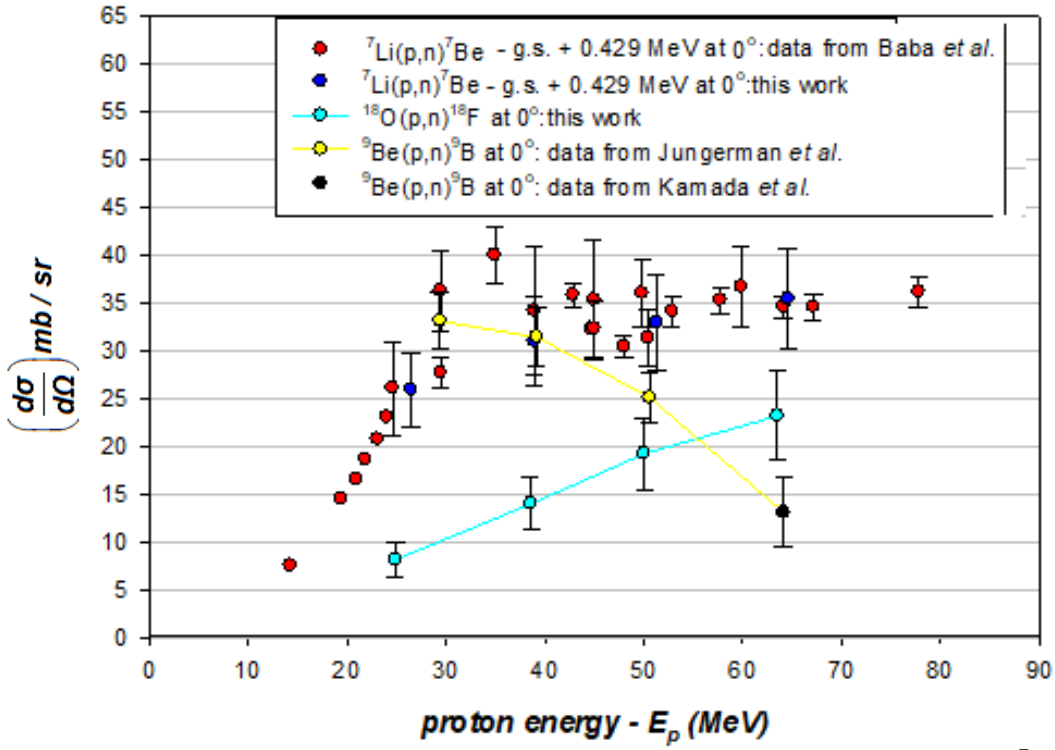

Figure 59: *Cross sections (laboratory frame) of the neutron peak for the reaction $^{7}Li(p,n)^{7}Be$ by Baba et al. [Ba99] and the reaction $^{9}Be(p,n)^{9}B$ by Jungerman et al. [Ju71] and Kamada et al. [Ka11] at angle 0° are compared to the reactions $^{7}Li(p,n)^{7}Be$ and $^{18}O(p,n)^{18}F$ at 0° of this work.*

The nominal proton energies were plotted instead of incoming proton beam energies, i.e. 25 MeV (30 MeV), 38.7 MeV (42 MeV), 50.2 (54 MeV) and 63.6 MeV (66 MeV) for the ^{18}O-water target as this is a differential cross section measurement but for the ^{7}Li target, incoming proton energies were plotted.

Figure 60 compares the $^{18}O(p,n)$ cross sections to $^{7}Li(p,n)$ cross sections, both from this work. Again, the cross sections for ^{7}Li are consistently larger than ^{18}O by a factor of about two, although both do not vary much with energy.

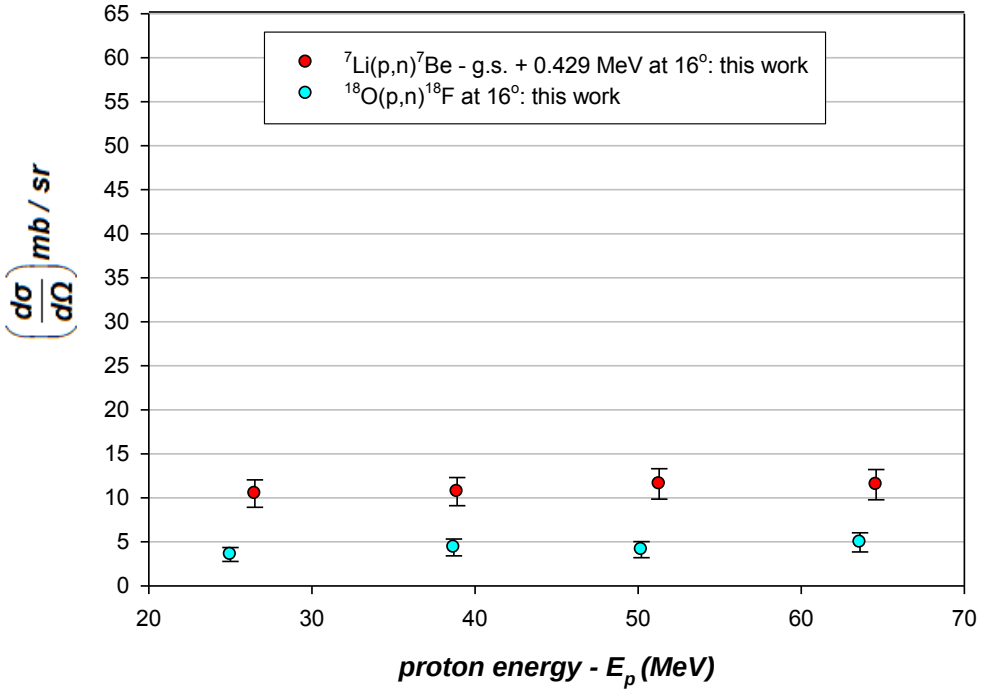

Figure 60: *Cross sections (laboratory frame) of the peak neutron production reaction $^{7}Li(p,n)^{7}Be$ at angle 16° are compared to the reactions $^{18}O(p,n)^{18}F$ at 16°, measured in this work.*

5.4.2 The comparison of the stopping length target spectrum of ^{9}Be and ^{18}O-water at 0° and 16°

The previous section compared the cross sections (dσ/dΩ) in mb/sr of ^{9}Be and ^{18}O. This section compares the stopping lengths of ^{9}Be and ^{18}O-water.

The corrected neutron energy spectrum from 62 MeV protons on 4 mm of ^{18}O-water is compared to the spectrum of 70 MeV protons on 4 mm ^{9}Be [Ka11]. The neutron spectra of 62 MeV protons on 4 mm of ^{18}O-water were calculated using the interpolation explained in the previous section. The measured spectrum from 62 MeV on 2 mm thickness was corrected into a spectrum of 4 mm by adding on to it the spectrum obtained from the interpolation of the subsequent 2 mm slice, making a total of 4 mm. Protons of 62 MeV lose an average of 4.3 MeV through 4 mm thickness of water whereas protons of 70 MeV lose an

average of 6 MeV through 4 mm thickness of beryllium [Zi08]. This larger energy loss in ^{9}Be compared to water produces the ^{9}Be spectrum with a broad monoenergetic peak.

Figure 61 shows that the cross sections ($d^2\sigma/d\Omega dE$) in mb/MeV/sr of ^{18}O are higher than those of ^{9}Be above 60 MeV.

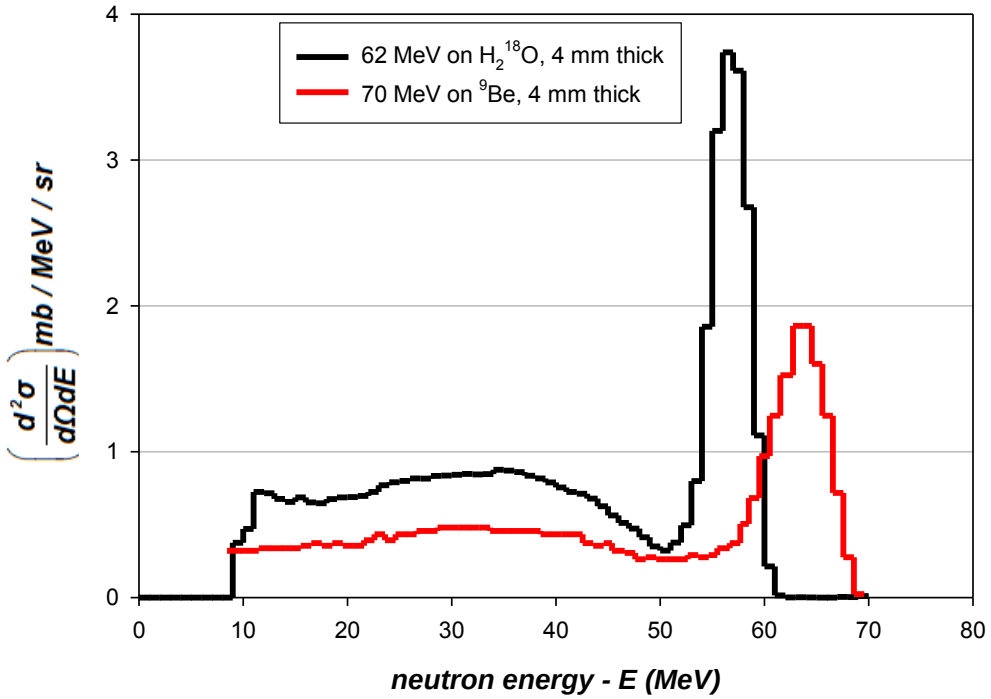

Figure 61: *Cross section (laboratory frame) spectrum of 70 MeV protons on 4 mm thick ^{9}Be [Ka11] compared with the cross section spectrum of 62 MeV protons on 4 mm thick ^{18}O-water target at 0°, measured in this work.*

Figure 62 shows the comparison of the neutron yields from the $H_2{}^{18}O$ and ^{9}Be. The fluence from ^{9}Be is higher than that from ^{18}O, which is the opposite of what we observe with cross sections, since cross sections take into consideration the material density of the target when calculated.

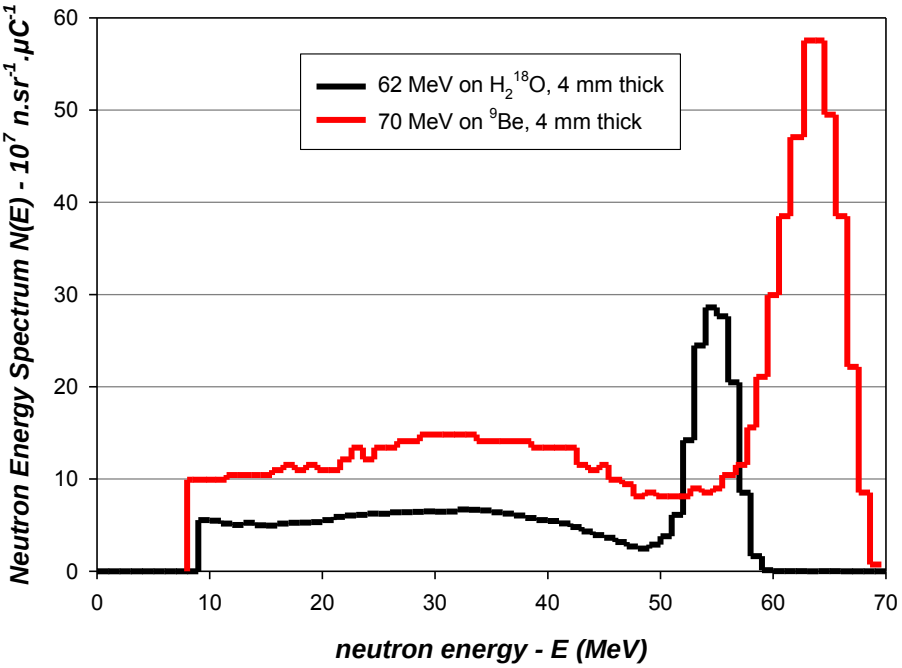

Figure 62: *Neutron energy spectrum of 70 MeV protons on 4 mm thick ^{9}Be [Ka11] compared with the neutron energy spectrum of 62 MeV protons on 4 mm thick ^{18}O-water at angle 0°, measured in this work.*

5.4.3 The comparison of neutron spectra from thick targets of ^{9}Be and ^{18}O-water at 0°

The thick target of ^{18}O-water was designed for 66 MeV protons, however, this target was actually measured with a 61.79 MeV beam which has a corresponding stopping-length of 32 mm, which means at least 8 mm of the target will be shielding all the neutrons produced.

The comparison of the thick stopping-length ^{18}O-water target to a ^{9}Be thick stopping-length target as measured by Amols *et al*. [Am77] is presented in Figure 63. Other measurements for the ^{9}Be target, compiled and performed by Alba *et al.* [Al13] are plotted in the same figure. The comparison shows that a stopping-length ^{9}Be target produces more neutrons than a stopping-length ^{18}O-water target. Higher counts are in the lower energy region of the ^{9}Be spectrum with a peak at 25 MeV. The difference in neutron production is due not only to the fact that the ^{9}Be cross sections are higher at energies below 50 MeV (see Figure 59) but also due to the density of ^{9}Be and ^{18}O-water atoms in the two materials. A 24 mm thick target of ^{9}Be has 3 x 10^{24} atoms/cm^{2}, while a 32 mm target of ^{18}O-water has 1 x 10^{24} atoms/cm^{2} of ^{18}O.

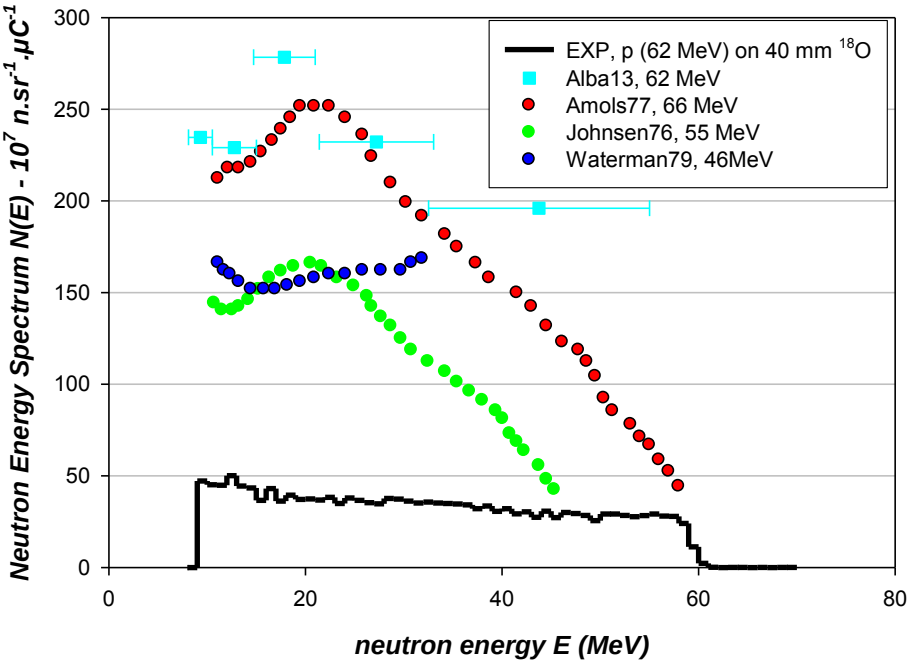

Figure 63: *The neutron energy spectrum of 62 MeV protons on 40 mm thick ^{18}O-water at 0˚ is compared to the experimental data of protons on ^{9}Be, compiled by Alba et al. [Al13].*

When corrected for density, the difference is smaller. Figure 64 shows cross sections ($d^2\sigma/d\Omega dE$) in mb/MeV/sr of the stopping-length targets of ^{18}O-water (this work) and ^{9}Be [Al13]. The averaged neutron cross section of ^{18}O-water is half of that of ^{9}Be. (This average was determined by summing all the counts of the cross section spectrum in each 1 MeV bin and dividing by the total number of bins).

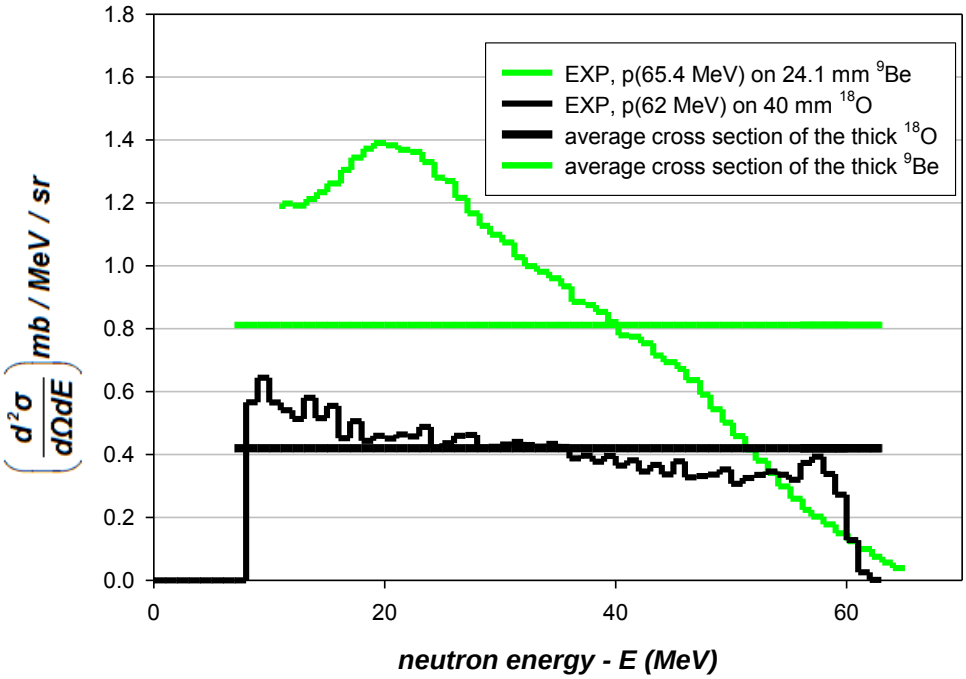

Figure 64: *The neutron energy spectra of the cross sections (laboratory frame) of 62 MeV protons on 40 ± 0.1 mm thick $H_2{}^{18}O$ at 0˚ with Amols' experimental neutron energy spectra of 65.4 MeV protons on 24.1 mm thick ^{9}Be at 0˚ [Am77]. The respective flat lines are an average cross section values.*

This chapter has presented the neutron energy spectrum measurements of the ^{18}O-water for both thin and thick targets as well as measured ^{18}O neutron cross sections. The next chapter will summarise and conclude this work and in particular the discussion on the performance of ^{18}O-water in relation to ^{7}Li and ^{9}Be targets.

CHAPTER 6: CONCLUSION & RECOMMENDATIONS

6.1 Summary of this research work

The main aim of this work was to explore ^{18}O as a potential high neutron flux producer when bombarded by protons. This was within the context of the plan for iThemba LABS to manufacture neutron-rich beams by fissioning uranium. The proposal [Ba12] for iThemba LABS is that a commercial 70 MeV negative-ion cyclotron, allowing simultaneous extraction of two H^- beams, be installed both for the production of radioactive-ion beams and for the simultaneous production of medical isotopes. The interest is to enhance the production yields of the neutron-rich ions by means of neutron-induced fission, U(n,f), which requires a method to convert protons from the cyclotron into neutrons.

The present measurements were carried out using the existing fast neutron beam facility at iThemba LABS. Neutrons were produced from the (p,xn) reactions using ^{7}Li and thin targets of ^{18}O-water at proton energies of 30, 42, 54 and 66 MeV. Neutrons were also produced from a thick target of ^{18}O-water at proton energy of 62 MeV. Measurements of the neutron spectra were made at 0° and 16°.

Since the neutron measurements were conducted in fields where both ɣ-rays and neutrons were present, pulse shape discrimination was employed in an NE213 liquid scintillator detector. Time-of-flight spectra were measured and converted to energy spectra. An existing NESR code was adopted and upgraded for this task.

The measured cross sections for $^{7}Li(p,n)^{7}Be$ at 30, 42, 54 and 66 MeV at 0° compared well with those reported by Baba *et al.* [Ba99] and Mosconi *et al*. [Mo10], within experimental uncertainties.

For the ^{18}O measurements with the thin target of ^{18}O-water, the centroids of the ground state peaks in the neutron spectra were calculated for proton beams of 66, 54, 42 and 30 MeV on an ^{18}O-water target of 1.9 ± 0.1mm thickness. These were compared to the centroids of the peaks in the measured spectra and were found to agree within uncertainties (Table 5).

At 62 MeV, the thick (stopping-length) ^{18}O-water target produced neutron energy spectra with few features at 0° and 16°, see Figure 44. Using the thin ^{18}O-water target spectra at 30, 42, 54 and 66 MeV for both angles, the thick target spectrum was empirically simulated by

interpolating between 62 and 30 MeV and extrapolating between 30 and 10 MeV. This enabled us to come to an understanding of the shape of the thick ^{18}O-water target spectrum.

The windows of the thin^{18}O-water target were constructed of thin plastic, resulting in the windows bulging under vacuum. The (bulged) target thickness was measured to be 1.9(1) mm but the adopted thickness was derived by fitting a normalization constant that gave the best agreement between the measured and empirically simulated spectra at 16°. The thickness of the thin ^{18}O-water target was determined in this way to be 2.03 ± 0.01 mm, and all spectra and cross sections were corrected to this thickness.

The thin targets of ^{18}O-water produced quasi-monoenergetic neutron spectra that are similar in shape to those of ^{7}Li, see Figures 38, Figure 39, Figure 42 and Figure 43. Neutron cross sections, ($d\sigma(E)/d\Omega$ in mb/sr), for the ground state neutrons produced by the ^{18}O(p,n)^{18}F reaction are presented against the average proton beam in the target, see Table 7.

Table 7: The neutron cross sections (σ) of the ^{18}O(p,n)^{18}F reaction at 25, 39, 50 and 64 MeV

Average proton energy E_p (MeV)	***Cross sections $d\sigma(E)/d\Omega$ (mb/sr), laboratory frame***
25.0	8.3 ± 1.7
38.7	14.1 ± 2.8
50.2	19.3 ± 3.9
63.6	23.3 ± 4.7

However, when the neutron cross sections measured for the thin ^{18}O-water target for the ^{18}O(p,n) reaction at 0° were compared to the neutron cross sections of ^{7}Li and ^{9}Be target for the same reaction, they were found to be significantly lower than those of ^{7}Li and ^{9}Be except above 60 MeV, where the ^{9}Be cross-section is below that of ^{18}O.

The Monte Carlo code, FLUKA was used to simulate the neutron spectra produced from the thin 2.5 mm ^{7}Li target at all of the measured energies and angles. FLUKA calculations do not produce peaks and do not reproduce the detailed shape of the experimental data in general. As an example, the experimental data has a distinct monoenergetic peak and a low energy tail. FLUKA was also used to simulate the neutron spectra produced by the thin (1.9 ± 0.1 mm) ^{18}O-water target at all the measured energies and angles, and from the thick (40 mm) ^{18}O-water target. The FLUKA spectra did not agree well with the measured spectra for any of these cases.

The Monte Carlo code MCNPX was also used to simulate the neutron spectra from the thin 2.5 mm ^{7}Li target. The simulated and measured spectra agree better at 0° than at 16°.

6.2 Evaluating research objectives

The averaged neutron cross sections from the thick stopping-length targets of ^{18}O-water did not live up to the promise of the ALICE-ASH code predictions. They were found to be half of that of ^{9}Be, see Figure 64. A stopping-length target of ^{9}Be produces more neutrons than ^{18}O in the form of water, in large part due to the effect of atomic densities.

6.3 Future research

If ^{18}O is to be used as a converter, then one possibility is the compound Be^{18}O (enriched beryllium oxide) which would produce a greater yield of neutrons than ^{18}O-water. This compound has the potential advantage to perform similarly to ^{7}Li above 60 MeV. Be^{18}O is a compound with high melting point compared to ^{7}Li and thus will be able to withstand power deposited by high beam currents.

Another possibility is to use deuterated ^{18}O-water ($D_2{}^{18}O$), where neutrons would also be produced by the deuterium. Neither of these materials were available for the present work.

REFERENCES

[Ad10] B. A. S. Adam, E. Z. Buthelezi, M. R. Nchodu, F. D. Smit, M. Herbert, *Monte Carlo simulations of the production of neutrons at iThemba LABS*, Radiation Measurements. 45(10), 1193-1196 (2010).

[Al13] R. Alba, M. Barbagallo, P. Boccaccio, A. Celentano, N. Colonna, G. Cosentino, A. Del Zoppo, A. Di Pietro, J. Esposito, P. Figuera, P. Finocchiaro, A. Kostyukov, C. Maiolino, M. Osipenko, G. Ricco, M. Ripani, C.M. Viberti,D. Santonocito, M. Schillaci, *Measurement of neutron yield by 62 MeV proton beam on a thick Beryllium target,* Journal of Physics: Conference Series 420, 2013.

[Am77] H. I. Amols, J. F. Dicello, M. Awschalom, L. Coulson, S. W. Johnsen and R. B. Theus, *Physical characterization of neutron beams produced by protons and deuterons of various energies bombarding beryllium and lithium targets of several thicknesses*, Med. Phys. 4, 486 (1977).

[An62] I. O. Anderson, S. Malmskog, *Investigation of the Pulse Height Distribution of Boron Trifluoride Proportional Counters*, *AE-84* (1962).

[Ba12] R. A. Bark, J. C. Cornell, *Proposal for a Radioactive-Ion Beam Facility at iThemba LABS*, August 2012.

[Ba99] M. Baba, Y. Nauchi, T. Iwasaki, T. Kiyosumi, M. Yoshioka, S. Matsuyama, N. Hirakawa, T. Nakamura, Su. Tanaka, S. Meigo, H. Nakashima, Sh. Tanaka, N. Nakao, *Characterization of a 40 - 90 MeV ^{7}Li(p,n) neutron source at TIARA using a proton recoil telescope and a TOF method,* Nucl. Instr. Meth. A428 (1999) 454 - 465.

[Bi64] J. B. Birks, *The Theory and Practice of Scintillation Counting*, Pergamon Press, Oxford, (1964).

[Bl82] M. Blann, J. Bisplinghoff., Code ALICE/LIVERMORE 82, Livermore Lawrence Laboratory, UCID-19614, 1982.

[Br06] C. H. M. Broeders, A. Yu. Konobeyev, Yu. A. Korovin, V. P. Lunev, M. Blann, *Pre-compound and Evaporation Model Code System for Calculation of Excitation Functions, Energy and Angular Distributions of Emitted Particles in Nuclear Reactions at Intermediate energies*, German, May 2006.

[Br02] F.D. Brooks, H. Klein, *Neutron spectrometry - historical review and present status*, Nucl. Instr. and Meth A 476 (2002) 1.

[Br79] F.D. Brooks, *Development of Organic Scintillators*, Nucl. Instr. and Meth. 162 (1979) 477.

[Bu02] A. Buffler, F.D. Brooks, M.S. Allie, P.J. Binns, V. Dangendorf, K.M. Langen, R. Nolte, H. Schuhmacher, *Measurement of neutron energy spectra from 15 to 150 MeV using stacked liquid scintillators*, Nucl. Instr. Meth. A476 (2002) 181-185.

[Bu14] A. Buffler, private communication 2014.12.08

[Bu69] W. R. Burrus and V. V. Verbinski, *Fast-Neutron Spectroscopy with Thick Organic Scintillators,* Nucl. Instr. and Meth. 67 (1969) 181.

[Ce79] R. A. Cecil,* B. D. Anderson,* and R. Madey*, *Improved predictions of neutron detection efficiency for hydrocarbon scintillators from 1 MeV to about 300 MeV*, Nucl. Instr. and Meth. 161 (1979) 439-447.

[Ch13] A. Chandra, *Neutron Detection by Pulse Shape Discrimination*, Summer Research Project Report, National Institute of Technology, Trichy, August 2013.

[Co15] A.C. Comrie, A. Buffler, F.D. Smit, H.J. Wörtche, *Digital neutron/gamma-ray discrimination with an organic scintillator at energies between 1 MeV and 100 MeV,* Nucl. Instr. Meth. A772 (2015) 43-49.

[Co86] P. N. Cooper, *Introduction to Nuclear Radiation Detectors*, University of Cambridge Press, (1986)

[Di88] J. K. Dickens, Oak Ridge National Laboratory Report, ORNL-6642 (1998).

[Du06] P. Van Duppen, *Isotope Separation On Line and Post Acceleration*, Lect. Notes Phys. 700, 37–77 (2006).

[Fa10] FAST ComTec MPA-3 Multiparameter Data Acquisition System User Manual Version 1.87, Grünwalder Weg 28a, D-82041 Oberhaching Germany, July 21, 2010 (http://www3.nd.edu/~wzech/mpa3doc.pdf: 06/12/2016).

[Fe05] A. Ferrari, P. R. Sala, A. Fassò, and J. Ranft, *FLUKA: a multi-particle transport code* (http://www.fluka.org/content/manuals/FM.pdf: 06/07/2016).

[Ha11] H. Harano and R. Nolte: *Quasi-monoenergetic neutron standards above 20 MeV*. *Metrologia* 48 S292-S303 (2011).

[Ho08] *Holifield Radioactive Ion Beam Facility Cyclotron Driver White Paper*, Oak Ridge National Laboratory, USA, 2-3 June 2008.

[Jo92] D. T. L. Jones, J. E. Symons, T. J. Fulcher, F. D. Brooks, M. R. Nchodu, M. S. Allie, A. Buffler, and M. J. Oliver, *Neutron fluence and kerma spectra of a p(66)/Be(40) clinical source*, Medical Physics 19, 1285 (1992).

[Ju71] J. A. Jungerman, F. P. Brady, W. J. Knox, T. Montgometry, M. R. McGie, J. L. Romero and Y. Ishizaki, *Production of medium-energy neutrons from proton bombardment of light elements,* Nucl. Instr. Meth. A94 (1971) 421-427.

[Ka11] S. Kamada, T. Itoga, Y. Unno, W. Takahashi, T. Oishi, M. Baba, *Measurement of Energy-angular Neutron Distribution for ^{7}Li, $^{9}Be(p,xn)$ Reaction at E_p = 70 MeV and 11 MeV,* Journal of the Korean Physical Society, Vol. 59, No. 2, pp. 1676 – 1680, August 2011.

[Ke08] K. W. Kemper, *Current and new facilities for radioactive beam physics*, 5th International Conference on Exotic Nuclei and Atomic Masses (ENAM '08), 7-14 September 2008, Ryn, Poland.

[Kl02] H. Klein, S. Neumann, *Neutron and photon spectrometry with liquid scintillation detectors in mixed fields*, Nucl. Instr. and Meth. A 476 (2002) 132.

[Kn00] G. F. Knoll, *Radiation Detection and Measurement*, 3rd edition, Wiley, New York, (2000).

[Kr88] K. S. Krane, *Introductory Nuclear Physics*. John Wiley & Sons, New York, USA, (1988).

[Lo77] M. A. Lone, C. B. Bigham, J. S. Fraser, H. R. Schneider, T. K. Alexander, A. J. Ferguson, and A. B. McDonald, *Thick target neutron yields from the $^{7}Li\left(^{d}_{p}n\right)$ and $^{9}Be\left(^{d}_{p}n\right)$ reactions*. Nuc. Instr. and Meth. 143 (1977) 331-344.

[Ma78] R. Madey, B. Anderson, A. Baldwin, J. Knudson, and T. Witten, *Large-Volume Neutron Counters with Subnanosecond Time Dispersion,* Annual Scientific and Technical Report, Indiana University Cyclotron Facility 1978, p. 131-132.

[Me89] M. W. Meier, W. B. Amian, D. A. Clark, C. A. Goulding, J. B. McClelland, G. L. Morgan and C. E. Moss, *Differential Neutron Production Cross Sections and Neutron Yields from stopping-Length Targets at 113 MeV Protons,* Report LA-11518-MS, Los Alamos National Laboratory, USA, (1989).

[Mo10] M. Mosconi, E. Musonza, A. Buffler, R. Nolte, S. Rottger, F. D. Smit, *Characterisation of the high-energy neutron beam at iThemba LABS,* Radiation Measurements, 45: 1342-1345, 14 June 2010.

[Ng12] Z. Ngcobo, O. M. Ndwandwe, R. Bark, J. Van Rooyen, Z. Zibi, *Radiation shielding calculations using MCNPX transport code for cost optimization of the shielding material to be used at iThemba LABS*, MSc dissertation, University of Zululand, South Africa, April 2012.

[No11] R. Nolte, S. Rottger, *Guidelines for Neutron Fluence Measurement at the TLABS Neutron Beam Facility* Physikalisch-Technische Bundesanstalt, Bundesalle 100, D-38116 Braunschweig, Germany, unpublished, 01 October 2011.

[Ob12] V. Oberacker, *Nuclear and Heavy-Ion Theory*, unpublished Physics 340A Lecture notes, Spring 2012, USA.

[Pe08] D. B. Pelowitz, editor. *MCNPX Version 2.6.0 User's Manual*, Report LA-CP-07-1473, Los Alamos National Laboratory, USA, April 2008.

[Pi96] J. V. Pilcher, *"The NAC MBD to VME Conversion Guide"*, 1996.

[Pl76] P. Plischke, V. Schröder, W. Scobel, L. Wilde, M. Bormann, *An electronic circuit for pulse shape discrimination in organic scintillators,* Nuc. Instr. and Meth. 136 (1976) 579.

[Ra95] Radford D, *ESCL8R and LEVIT8R: Software for interactive graphical analysis of HPGe coincidence data set*, Nucl. Instr. & Meth. A, 361 (1995) 297-305.

[Ri91] P. Rinard, *"Neutron Interactions with Matter. In Passive Nondestructive Assay of Nuclear Materials"*, (ed. D. Reilly, N. Ensslin, and H. Smith Jr), Nuclear Regulatory Commission, NUREG/CR- 5550. Pp. 357-377, (1991).

[Ri98] D. Ridikas and W. Mittig, *Neutron and Energy Production by Energetic Projectiles: Protons or Deuterons? Nuclear Instruments and Methods in Physics Research Section A: Accelerators, Spectrometers, Detectors and Associated Equipment, Elsevier, 1998, 418, pp.449-457.*

[Se48] R. Serber, *Nuclear Reactions at High Energies*, Phys. Rev. 72, 1948.

[Si18] Sigma-Aldrich, product specification for ^{18}O-water for PET, 97 atom % ^{18}O, (https://sigmaaldrich.com/catalog/product/aldrich/329878?lang=en&region=ZA: 23/05/2018)

[Sm16] F. D. Smit, private communication 2016.04.21

[Sp74] P. Sperr, H. Spieler, M.R. Maier, D. Evers, *A simple pulse-shape discrimination circuit*, Nucl. Instr. Meth. 116 (1974) 55-59.

[To14] F. Tovesson, A. Laptev, T.S. Hill, *Fast Neutron-Induced Fission Cross Sections of $^{233,234,236,238}U$* up to 200 MeV, Nuclear Science and Engineering journal, 178:1, 57-65 (2014).

[Ts83] N. Tsoulfanidis, *Measurement and Detection of Radiation*. McGraw-Hill, New York, (1983).

[Vr12] J. Vrzalová, O. Svoboda, A. Kugler, M. Suchopár, V. Wagner, *Measurements of cross-sections of (n,xn) threshold reactions in various materials*, EPJ Web of Conferences 21 10007 (2012).

[Wa73] J. W. Wachter, R. T. Santoro, T. A. Love, W. Zobel, *Fast forward neutron production in the 7Li(p,n)7Be reaction for 41 and 64 MeV protons*, Nucl. Instr. & Meth. A, 113 (1973) 185-187.

[Wo91] C. L. Wood, *Construction, Calibration and Use of a Neutron Time-of-Flight Spectrometer*. No. AFIT/GNE/ENP/91M-12. AIR FORCE INST OF TECH WRIGHT-PATTERSON AFB OH SCHOOL OF ENGINEERING, 1991.

[Yo06] P. G. Young, M. B. Chadwick, P. Talou, D. G. Madland, and L.C. Leal, *"Evaluated Nuclear Data File, U-235."*, June 2006. Cross Section Data for U-235, accessed January 18, 2016.

[You06] P. G. Young, M. B. Chadwick, H. Derrien and A. Courcelle, *"Evaluated Nuclear Data File, U-235."*, December 2006. Cross Section Data for U-235, accessed January 18, 2016.

[Zi08] J. F. Ziegler, *The Stopping and Range of Ions in Matter software*, (http://www.srim.org :11/08/2014).

[Zi09] J.F. Ziegler, J.P. Biersack, M.D. Ziegler, *SRIM – The Stopping and Range of Ions in Matter*", Ion Implantation Press (2009).

[Zi10] J.F. Ziegler, M.D. Ziegler, J.P. Biersack, *SRIM – The Stopping and Range of Ions in Matter*, Nucl. Instr. & Meth. B, 268 (2010) 1818-1823.

APPENDICES

Appendix 1: The calculation of the solid angle

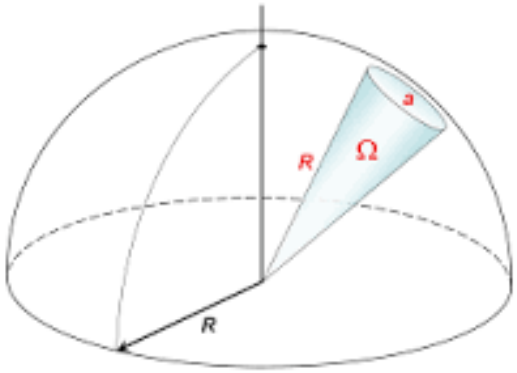

Figure 65: *The demonstration of a three – dimensional solid angle.*

Figure 65 illustrates the solid angle Ω, which is a dimensionless quantity that the sphere of radius R, which is the distance between the target and the face of the detector, subtends to the sphere's segment area a, which is the surface area of the face of the detector. The solid angle is the ration between the area a and the square of the sphere's radius R, $\Omega = a/R^2$

Let us calculate the solid angle subtended by the sphere centred at the position of the target that is 8 m (800 cm) from the cylindrical detector with a radius of 2.5 cm.

i) Sphere radius (R) = 800 cm;

ii) subtended area a, on the detector with a radius r =2.5 cm, = πr^2 = 19.635 cm^2.

$\Omega(sr)=a/R^2$ = 3.06797E-05

Appendix 2: The measurement of the $H_2{}^{18}O$ target thickness using laser.

Figure 66 shows the top view of the schematics developed for measuring the target thickness. The symbols used are described below.

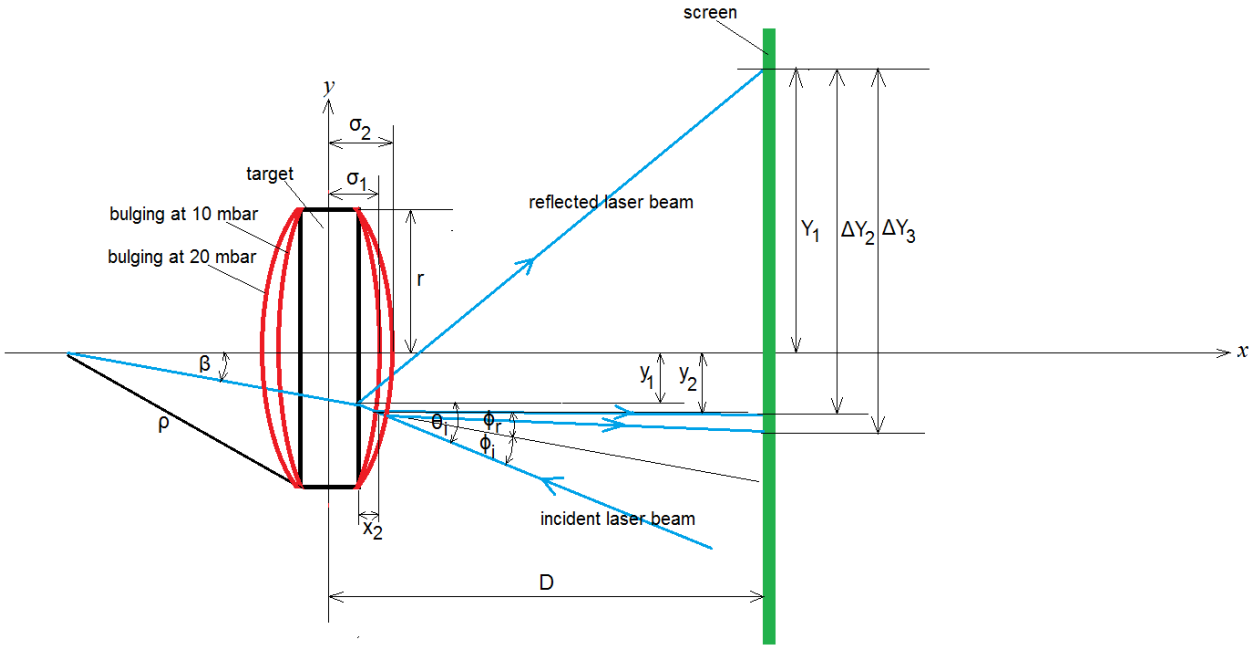

Figure 66: *The top view of the schematics of the bulging target under the 10 mbar and 20 mbar.*

y_1: laser pos. from the centre of the target in mm.

Y_1: initial reflected laser pos. on the screen w.r.t the centre of target.

Y_2: new reflected laser pos. on the screen at 10 mbar w.r.t the centre of target.

Y_3: new reflected laser pos. on the screen at 20 mbar.

ΔY_2: change in pos. on the screen at 10 mbar.

ΔY_3: change in pos. on the screen at 20 mbar.

σ_1: change in thickness on one side of the target at 10 mbar in mm.

σ_2: change in thickness on one side of the target at 20 mbar in mm.

$$x_2 = \frac{-\left(\tan\theta_i y_1 + \frac{\sigma}{2} - \frac{r^2}{2\sigma}\right) \pm \sqrt{\tan\theta_i y_1 + \frac{\sigma}{2} - \frac{r^2}{2\sigma} - \left(1+\tan^2\theta_i\right)\left(y_1^2 - r^2\right)}}{\left(1+\tan^2\theta_i\right)}$$

$$y_2 = \sqrt{\rho^2 - (x_2 + (\rho - \sigma))^2}$$

$$\rho = \frac{\sigma^2 + r^2}{2\sigma}$$

$$\Delta Y = D\tan\theta_i + (D - x_2)\tan(\theta_i - 2\phi_i) + \frac{x_2}{\tan\theta_i}$$

$$\sin\beta = \frac{y_2}{\rho}$$

$$\phi_i = \theta_i - \beta$$

During the measurement the target chamber was pumped down to 10 mbar and so the corresponding change in thickness was σ_1 = 0.44 ± 0.07 mm using Figure 67.

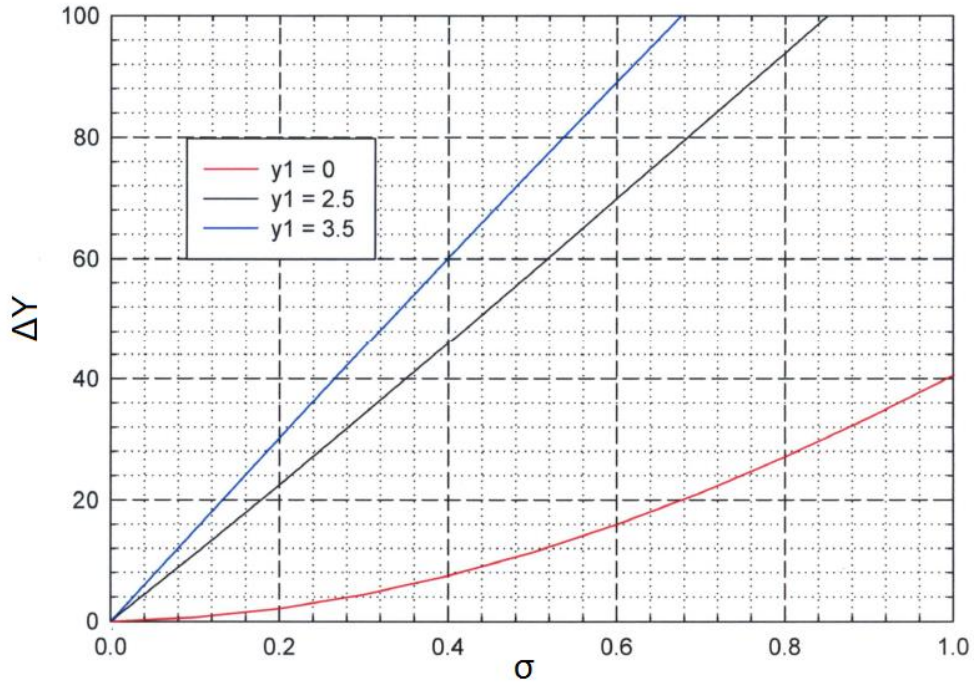

Figure 67: *The relationship between the change in position on the screen (ΔY) to the change in thickness (σ) on one side of the target.*

Total change in thickness on both sides was measured to be ≈ 0.9 ± 0.1 mm.

Appendix 3: The section of the Neutron Energy Spectrum Reduction code that converted time-of-flight spectrum into neutron energy spectrum.

```
////////////////////////////////////////////////////////
// Zipho
short int  ErgCalc(short int i)  // energy calculation routine
{
float vel, vel2, m = 931.573, rm; // velocity, velocity squared, neutron mass, random number
float c0 = 0.3 ;   // speed of light
int e;    // neutron energy variable


rm=((float) rand() / (RAND_MAX)); // random number between 0 and 1

if (i <2 )    // neutron low energy cut - 2 MeV
        e = 0.0;  // this should count with neutrons with e = 0 MeV
else
        {
                vel = d*f / c0/ (T0-(rm+i-0.5));    // transform time of a neutron into velocity
                vel2 = pow(vel,2);      // squaring the velocity
                e = (int) (m * (1.0/sqrt(1-vel2) - 1)+0.5);  //  relativistic energy formula
        };
return e;   // compute the energy value 'e'

}
// end Zipho
////////////////////////////////////////////////////////
```

Appendix 4: MCNPX input files

```
c 65 MEV PROTON ON TO THE LITHIUM TARGET
c Cell Cards:
01  2  -1.848      -1     imp:h=1   imp:n=1     imp:p=1     $ lithium as the target
02  0             -2 +1   imp:h=1   imp:n=1     imp:p=1     $ Vacuum
c
03  1  -1.205E-3   -5 +2 +3 +4   imp:h=0  imp:n=1  imp:p=1    $ air inside vault
c
04  1  -1.205E-3   -3      imp:h=0   imp:n=1     imp:p=1     $ air inside the sphere
05  1  -1.205E-3   -4      imp:h=0   imp:n=1     imp:p=1     $ air inside the sphere
c
06  0            +5      imp:h=0   imp:n=0     imp:p=0     $ UmWelt = External Void
c ==========================================

c ==========================================
c Surface Cards
01  RCC       0  0  120      5.33   0   0    +1              $ lithium target surface
02  RPP      -5    +6       -2    +2   117  +123            $ vacuum surface
c
03  SPH      805       0        120    +2.5                $ spherical surface
04  SPH      773.815  -221.888  120    +2.5                $ spherical surface
c
05   RPP    -9000    +9000     -9000    +9000     -9000    +9000     $ External Void = UmWelt
Boundary
c ==========================================

c ==========================================
c Data Cards:
MODE H N P
CUT:H J 3 J J J
c
c PHYSICS CARDS:
c **** Physics Table FOR MCNPX 2.6.0 *****
phys:h    70
          0
        -1
```

```
        J
        0
        J
        0
phys:n    70
          0
          0
       -1001
         -1
          0
          0
phys:p    70
          0
          0
         -1
          1
          0
C
SDEF    PAR = H
       ERG = 65
       pos = -2  0  120
       axs = 1  0   0
       vec = 1  0   0
       dir = +1
       ext = 0
       rad = d1
si1 h  0.0  0.5      $ Sampling of source point along radial coordinate from R.min to R.max
sp1  -21   1        $ Probability of sampling of source point in radial dimension: power law: r**1
(disk/cyl)
c
c =====
c Materials:
c AIR at STP:
m1     6000   -1.24E-4          $ Air, dry.  Density = 1.205E-03 g/cc
       7014   -0.755267         $ Air, dry.  Density = 1.205E-03 g/cc
       8016   -0.231781         $ Air, dry.  Density = 1.205E-03 g/cc
      18000   -0.012827         $ Air, dry.  Density = 1.205E-03 g/cc
```

```
c lithium target
 m2    3007.74c  -1.0
c =====
c TALLY DEFINITIONS:
c current rate through the surface:
F12:n  3
FM12  6.423E10
c
F22:n  4
FM22  6.423E10
c
E0 0  1    2   3  4  5  6   7   8    9 &
   10  11  12  13  14 15  16  17  18  19  20 21  22  23 24  25 &
   26  27  28  29  30 31  32  33 34   35  36  37  38  39  40 &
   41  42   43  44  45  46  47  48   49  50  51  52  53  54  55&
   56  57  58  59  60  61  62   63   64 65  66 67  68  69  70
c =====
PRINT  10  40  50  60  72  100  110  120  128  170  200
c
NPS 10000000000000
```

Appendix 5: Energy spectral data tables

^{7}Li(p,xn) at 0°

Neutron energy – E(MeV)	*E_p = 66 MeV* *N(E) -10^{7}n.sr^{-1}.μC^{-1}*	*E_p = 54 MeV* *N(E) -10^{7}n.sr^{-1}.μC^{-1}*	*E_p = 42 MeV* *N(E) -10^{7}n.sr^{-1}.μC^{-1}*	*E_p = 30 MeV* *N(E) -10^{7}n.sr^{-1}.μC^{-1}*
0	0.00E+00	0.00E+00	0.00E+00	0.00E+00
1	0.00E+00	0.00E+00	0.00E+00	0.00E+00
2	0.00E+00	0.00E+00	0.00E+00	0.00E+00
3	0.00E+00	0.00E+00	0.00E+00	0.00E+00
4	0.00E+00	0.00E+00	0.00E+00	0.00E+00
5	0.00E+00	0.00E+00	0.00E+00	0.00E+00
6	0.00E+00	0.00E+00	0.00E+00	0.00E+00
7	0.00E+00	0.00E+00	0.00E+00	0.00E+00
8	0.00E+00	0.00E+00	0.00E+00	0.00E+00
9	0.00E+00	0.00E+00	0.00E+00	0.00E+00
10	6.53E+00	8.54E+00	1.03E+01	1.17E+01
11	5.83E+00	7.77E+00	9.19E+00	9.78E+00
12	5.54E+00	7.49E+00	9.10E+00	8.72E+00
13	5.65E+00	7.72E+00	9.20E+00	8.13E+00
14	6.31E+00	8.47E+00	1.01E+01	8.10E+00
15	6.19E+00	8.30E+00	9.79E+00	6.96E+00
16	5.74E+00	7.77E+00	9.23E+00	5.94E+00
17	6.15E+00	8.39E+00	9.28E+00	5.70E+00
18	6.25E+00	8.48E+00	9.09E+00	4.97E+00
19	6.29E+00	8.82E+00	8.88E+00	4.39E+00
20	6.39E+00	8.43E+00	8.25E+00	3.61E+00
21	6.81E+00	9.05E+00	8.40E+00	4.25E+00
22	7.22E+00	9.07E+00	8.41E+00	3.97E+00
23	7.74E+00	9.47E+00	8.67E+00	3.78E+00
24	8.09E+00	9.07E+00	8.22E+00	2.39E+00
25	8.17E+00	8.97E+00	7.91E+00	2.15E+01
26	8.50E+00	8.96E+00	7.64E+00	4.99E+01
27	8.82E+00	8.84E+00	7.17E+00	5.42E+01
28	9.21E+00	9.06E+00	6.88E+00	4.21E+01
29	9.38E+00	9.11E+00	6.50E+00	1.97E+00
30	9.30E+00	9.03E+00	5.83E+00	4.02E-03
31	9.45E+00	9.09E+00	4.91E+00	2.01E-03
32	9.17E+00	8.98E+00	4.19E+00	4.02E-03
33	9.04E+00	8.92E+00	3.56E+00	
34	9.08E+00	8.53E+00	2.91E+00	
35	8.74E+00	8.47E+00	3.46E+00	
36	8.79E+00	8.02E+00	5.08E+00	
37	8.56E+00	7.67E+00	3.86E+00	
38	8.42E+00	7.26E+00	5.31E+00	
39	8.26E+00	6.67E+00	5.30E+01	
40	8.12E+00	6.31E+00	8.72E+01	
41	7.98E+00	5.91E+00	6.06E+01	
42	8.01E+00	5.15E+00	6.19E+00	
43	7.96E+00	4.28E+00	3.54E-03	

44	7.86E+00	3.77E+00	1.18E-03	
45	7.67E+00	2.88E+00	1.77E-03	
46	8.08E+00	2.78E+00		
47	8.12E+00	4.40E+00		
48	7.79E+00	5.35E+00		
49	7.49E+00	3.96E+00		
50	7.19E+00	2.11E+01		
51	6.73E+00	8.81E+01		
52	6.25E+00	8.57E+01		
53	6.05E+00	2.37E+01		
54	5.83E+00	9.01E-01		
55	5.29E+00	1.33E-03		
56	4.48E+00	1.33E-03		
57	3.81E+00	6.63E-04		
58	3.45E+00	1.50E-03		
59	2.87E+00			
60	4.15E+00			
61	6.27E+00			
62	6.10E+00			
63	2.29E+01			
64	7.82E+01			
65	1.03E+02			
66	5.06E+01			
67	6.06E+00			
68	6.31E-02			
69	7.09E-04			
70	1.42E-03			

^{7}Li(p,xn) at 16°

Neutron energy – E(MeV)	E_p = 66 MeV N(E) -10^{7}n.sr^{-1}.μC^{-1}	E_p = 54 MeV N(E) -10^{7}n.sr^{-1}.μC^{-1}	E_p = 42 MeV N(E) -10^{7}n.sr^{-1}.μC^{-1}	E_p = 30 MeV N(E) -10^{7}n.sr^{-1}.μC^{-1}
0	0.00E+00	0.00E+00	0.00E+00	0.00E+00
1	0.00E+00	0.00E+00	0.00E+00	0.00E+00
2	0.00E+00	0.00E+00	0.00E+00	0.00E+00
3	0.00E+00	0.00E+00	0.00E+00	0.00E+00
4	0.00E+00	0.00E+00	0.00E+00	0.00E+00
5	0.00E+00	0.00E+00	0.00E+00	0.00E+00
6	0.00E+00	0.00E+00	0.00E+00	0.00E+00
7	0.00E+00	0.00E+00	0.00E+00	0.00E+00
8	0.00E+00	0.00E+00	0.00E+00	0.00E+00
9	0.00E+00	0.00E+00	0.00E+00	0.00E+00
10	4.58E+00	5.98E+00	6.90E+00	8.68E+00
11	4.17E+00	5.38E+00	6.16E+00	7.49E+00
12	4.07E+00	5.33E+00	6.17E+00	7.21E+00
13	4.24E+00	5.47E+00	6.25E+00	6.64E+00
14	4.61E+00	6.22E+00	6.99E+00	7.47E+00
15	4.57E+00	6.09E+00	6.79E+00	6.90E+00
16	4.34E+00	5.72E+00	6.20E+00	6.22E+00
17	4.72E+00	6.09E+00	6.70E+00	5.66E+00
18	4.71E+00	6.09E+00	6.33E+00	5.34E+00
19	4.85E+00	6.36E+00	6.47E+00	4.72E+00
20	4.74E+00	6.01E+00	6.32E+00	4.44E+00
21	5.07E+00	6.35E+00	6.61E+00	4.41E+00
22	5.32E+00	6.50E+00	6.75E+00	3.97E+00
23	5.77E+00	6.65E+00	7.12E+00	3.03E+00
24	5.82E+00	6.60E+00	6.97E+00	2.62E+00
25	5.95E+00	6.65E+00	6.84E+00	1.76E+01
26	6.19E+00	6.81E+00	6.94E+00	2.43E+01
27	6.35E+00	7.07E+00	6.93E+00	2.53E+01
28	6.63E+00	7.23E+00	7.18E+00	9.09E+00
29	6.79E+00	7.39E+00	6.89E+00	7.76E-03
30	6.93E+00	7.64E+00	6.03E+00	
31	7.03E+00	7.75E+00	5.46E+00	
32	7.20E+00	7.76E+00	5.10E+00	
33	7.20E+00	7.66E+00	4.45E+00	
34	7.11E+00	7.72E+00	4.21E+00	
35	7.03E+00	7.72E+00	4.47E+00	
36	7.04E+00	7.70E+00	3.33E+00	
37	7.05E+00	7.62E+00	1.72E+00	
38	6.87E+00	7.43E+00	9.76E+00	
39	7.08E+00	7.44E+00	2.99E+01	
40	7.17E+00	7.34E+00	2.83E+01	
41	7.06E+00	6.43E+00	6.19E+00	
42	7.25E+00	5.59E+00	2.90E-02	
43	7.46E+00	5.23E+00	2.72E-03	
44	7.34E+00	4.73E+00	3.63E-03	
45	7.40E+00	4.21E+00	1.81E-03	

46	7.64E+00	4.80E+00		
47	7.74E+00	3.95E+00		
48	7.78E+00	2.06E+00		
49	7.61E+00	4.20E+00		
50	7.44E+00	2.30E+01		
51	7.61E+00	2.73E+01		
52	7.40E+00	1.07E+01		
53	7.18E+00	3.11E-01		
54	6.64E+00	3.01E-03		
55	5.58E+00			
56	5.38E+00			
57	5.01E+00			
58	4.96E+00			
59	5.18E+00			
60	4.42E+00			
61	2.59E+00			
62	3.44E+00			
63	1.70E+01			
64	2.54E+01			
65	1.37E+01			
66	2.70E+00			
67	1.26E-01			
68	3.01E-03			
69	3.01E-03			
70	3.76E-03			

^{18}O(p,xn) at 0°

Neutron energy – E(MeV)	E_p = 66 MeV N(E) -10^7n.sr^{-1}.μC^{-1}	E_p = 54 MeV N(E) -10^7n.sr^{-1}.μC^{-1}	E_p = 42 MeV N(E) -10^7n.sr^{-1}.μC^{-1}	E_p = 30 MeV N(E) -10^7n.sr^{-1}.μC^{-1}
0	0.00E+00	0.00E+00	0.00E+00	0.00E+00
1	0.00E+00	0.00E+00	0.00E+00	0.00E+00
2	0.00E+00	0.00E+00	0.00E+00	0.00E+00
3	0.00E+00	0.00E+00	0.00E+00	0.00E+00
4	0.00E+00	0.00E+00	0.00E+00	0.00E+00
5	0.00E+00	0.00E+00	0.00E+00	0.00E+00
6	0.00E+00	0.00E+00	0.00E+00	0.00E+00
7	0.00E+00	0.00E+00	0.00E+00	0.00E+00
8	0.00E+00	0.00E+00	0.00E+00	0.00E+00
9	0.00E+00	0.00E+00	0.00E+00	0.00E+00
10	4.86E+00	5.58E+00	6.65E+00	8.29E+00
11	4.09E+00	4.79E+00	5.62E+00	6.87E+00
12	3.75E+00	4.43E+00	5.21E+00	5.73E+00
13	3.65E+00	4.24E+00	5.15E+00	5.06E+00
14	3.89E+00	4.53E+00	5.47E+00	5.11E+00
15	3.74E+00	4.34E+00	5.19E+00	4.27E+00
16	3.33E+00	3.94E+00	4.69E+00	3.20E+00
17	3.47E+00	4.20E+00	4.67E+00	3.06E+00
18	3.56E+00	3.89E+00	4.32E+00	2.56E+00
19	3.48E+00	4.20E+00	4.22E+00	2.15E+00
20	3.36E+00	3.98E+00	3.80E+00	1.95E+00
21	3.72E+00	4.33E+00	3.86E+00	1.78E+00
22	3.80E+00	4.53E+00	3.44E+00	1.96E+00
23	3.82E+00	4.86E+00	3.59E+00	2.62E+00
24	3.96E+00	4.79E+00	3.43E+00	6.63E+00
25	4.18E+00	4.50E+00	3.00E+00	6.73E+00
26	4.24E+00	4.93E+00	2.90E+00	7.31E+00
27	4.61E+00	4.71E+00	2.78E+00	2.96E+00
28	4.54E+00	4.76E+00	2.78E+00	5.39E-01
29	4.83E+00	4.69E+00	2.37E+00	
30	4.67E+00	4.51E+00	1.87E+00	
31	4.78E+00	4.38E+00	1.78E+00	
32	5.00E+00	4.24E+00	1.57E+00	
33	4.83E+00	3.97E+00	1.36E+00	
34	5.00E+00	3.70E+00	1.34E+00	
35	5.07E+00	3.79E+00	1.91E+00	
36	5.07E+00	3.45E+00	2.46E+00	
37	4.98E+00	3.09E+00	5.58E+00	
38	5.11E+00	2.70E+00	1.30E+01	
39	5.25E+00	2.70E+00	1.71E+01	
40	5.36E+00	2.62E+00	1.01E+01	
41	4.93E+00	1.99E+00	2.05E+00	
42	4.93E+00	1.57E+00	9.66E-03	
43	4.88E+00	1.35E+00		
44	4.63E+00	1.45E+00		
45	4.47E+00	1.32E+00		

46	4.23E+00	1.78E+00		
47	4.21E+00	2.53E+00		
48	4.24E+00	3.11E+00		
49	4.02E+00	1.04E+01		
50	3.61E+00	2.21E+01		
51	3.46E+00	2.11E+01		
52	3.29E+00	7.79E+00		
53	2.99E+00	6.03E-01		
54	2.49E+00	2.27E-03		
55	1.77E+00			
56	1.28E+00			
57	1.35E+00			
58	1.80E+00			
59	2.06E+00			
60	2.95E+00			
61	3.57E+00			
62	9.65E+00			
63	2.38E+01			
64	3.00E+01			
65	1.72E+01			
66	3.57E+00			
67	1.79E-01			
68	7.86E-03			
69	5.89E-03			
70	1.96E-02			

$^{18}O(p,xn)$ at 16°

Neutron energy – E(MeV)	*E_p = 66 MeV N(E) -10^7n.sr^{-1}.μC^{-1}*	*E_p = 54 MeV N(E) -10^7n.sr^{-1}.μC^{-1}*	*E_p = 42 MeV N(E) -10^7n.sr^{-1}.μC^{-1}*	*E_p = 30 MeV N(E) -10^7n.sr^{-1}.μC^{-1}*
0	0.00E+00	0.00E+00	0.00E+00	0.00E+00
1	0.00E+00	0.00E+00	0.00E+00	0.00E+00
2	0.00E+00	0.00E+00	0.00E+00	0.00E+00
3	0.00E+00	0.00E+00	0.00E+00	0.00E+00
4	0.00E+00	0.00E+00	0.00E+00	0.00E+00
5	0.00E+00	0.00E+00	0.00E+00	0.00E+00
6	0.00E+00	0.00E+00	0.00E+00	0.00E+00
7	0.00E+00	0.00E+00	0.00E+00	0.00E+00
8	0.00E+00	0.00E+00	0.00E+00	0.00E+00
9	0.00E+00	0.00E+00	0.00E+00	0.00E+00
10	3.58E+00	3.56E+00	4.66E+00	5.75E+00
11	3.01E+00	2.99E+00	3.88E+00	4.61E+00
12	2.77E+00	2.79E+00	3.71E+00	4.00E+00
13	2.77E+00	2.77E+00	3.73E+00	3.67E+00
14	2.96E+00	3.00E+00	3.89E+00	3.67E+00
15	2.79E+00	2.83E+00	3.77E+00	3.15E+00
16	2.50E+00	2.61E+00	3.35E+00	2.61E+00
17	2.58E+00	2.77E+00	3.32E+00	2.51E+00
18	2.61E+00	2.74E+00	3.26E+00	2.41E+00
19	2.65E+00	2.74E+00	3.17E+00	2.05E+00
20	2.56E+00	2.64E+00	2.76E+00	1.60E+00
21	2.61E+00	2.83E+00	2.84E+00	1.49E+00
22	2.75E+00	2.92E+00	2.71E+00	1.35E+00
23	2.99E+00	3.07E+00	2.80E+00	1.94E+00
24	2.98E+00	3.06E+00	2.75E+00	3.12E+00
25	3.01E+00	3.11E+00	2.63E+00	3.18E+00
26	3.09E+00	3.27E+00	2.43E+00	2.89E+00
27	3.36E+00	3.27E+00	2.25E+00	1.15E+00
28	3.38E+00	3.30E+00	2.52E+00	7.76E-02
29	3.34E+00	3.38E+00	2.21E+00	2.68E-03
30	3.57E+00	3.43E+00	2.11E+00	2.69E-03
31	3.53E+00	3.29E+00	2.14E+00	2.69E-03
32	3.64E+00	3.12E+00	2.09E+00	
33	3.59E+00	2.83E+00	1.44E+00	
34	3.60E+00	2.76E+00	1.23E+00	
35	3.74E+00	2.82E+00	1.46E+00	
36	3.88E+00	2.56E+00	1.39E+00	
37	3.85E+00	2.30E+00	2.69E+00	
38	4.05E+00	2.09E+00	4.64E+00	
39	4.05E+00	2.29E+00	4.72E+00	
40	4.14E+00	2.06E+00	2.35E+00	
41	4.04E+00	1.87E+00	1.64E-01	
42	4.09E+00	1.91E+00	1.91E-03	
43	4.06E+00	1.90E+00	9.53E-04	
44	4.02E+00	1.41E+00	9.53E-04	
45	3.79E+00	1.02E+00		

46	3.51E+00	1.24E+00		
47	3.33E+00	1.53E+00		
48	3.36E+00	1.50E+00		
49	3.08E+00	3.61E+00		
50	2.73E+00	5.39E+00		
51	2.49E+00	3.70E+00		
52	2.64E+00	5.93E-01		
53	2.45E+00	1.13E-02		
54	2.19E+00			
55	2.25E+00			
56	2.05E+00			
57	1.65E+00			
58	1.44E+00			
59	1.59E+00			
60	1.85E+00			
61	1.86E+00			
62	3.54E+00			
63	5.76E+00			
64	4.82E+00			
65	1.53E+00			
66	1.35E-01			
67	5.98E-03			
68	1.30E-02			
69	1.10E-02			
70	5.98E-03			

Thick $^{18}O(p,xn)$ at 0°

Neutron energy – E(MeV)	*E_p = 62 MeV* *N(E) -10^7n.sr^{-1}.μC^{-1}*
0	0.00E+00
1	0.00E+00
2	0.00E+00
3	0.00E+00
4	0.00E+00
5	0.00E+00
6	0.00E+00
7	0.00E+00
8	0.00E+00
9	0.00E+00
10	5.37E+01
11	4.72E+01
12	4.52E+01
13	4.48E+01
14	4.78E+01
15	4.50E+01
16	4.14E+01
17	4.10E+01
18	3.97E+01
19	3.85E+01
20	3.80E+01
21	3.75E+01
22	3.76E+01
23	3.79E+01
24	3.86E+01
25	3.69E+01
26	3.61E+01
27	3.69E+01
28	3.68E+01
29	3.64E+01
30	3.64E+01
31	3.63E+01
32	3.59E+01
33	3.60E+01
34	3.56E+01
35	3.50E+01
36	3.61E+01
37	3.40E+01
38	3.25E+01
39	3.27E+01
40	3.23E+01
41	3.13E+01
42	3.12E+01
43	2.99E+01
44	2.94E+01
45	2.86E+01

46	3.02E+01
47	2.84E+01
48	2.89E+01
49	2.82E+01
50	2.82E+01
51	2.67E+01
52	2.79E+01
53	2.84E+01
54	2.80E+01
55	2.86E+01
56	2.77E+01
57	2.82E+01
58	3.10E+01
59	2.96E+01
60	2.29E+01
61	1.12E+01
62	2.14E+00
63	1.04E-01

Thick $^{18}O(p,xn)$ at 16°

Neutron energy – E(MeV)	*E_p = 62 MeV* *N(E) -10^7n.sr^{-1}.μC^{-1}*
0	0.00E+00
1	0.00E+00
2	0.00E+00
3	0.00E+00
4	0.00E+00
5	0.00E+00
6	0.00E+00
7	0.00E+00
8	0.00E+00
9	0.00E+00
10	5.24E+01
11	4.77E+01
12	4.57E+01
13	4.45E+01
14	4.76E+01
15	4.60E+01
16	4.25E+01
17	4.20E+01
18	4.12E+01
19	4.07E+01
20	3.87E+01
21	3.90E+01
22	3.93E+01
23	4.07E+01
24	3.89E+01
25	3.91E+01
26	3.90E+01
27	3.82E+01
28	3.78E+01
29	3.82E+01
30	3.67E+01
31	3.66E+01
32	3.64E+01
33	3.67E+01
34	3.48E+01
35	3.32E+01
36	3.35E+01
37	3.20E+01
38	3.06E+01
39	2.98E+01
40	2.86E+01
41	2.63E+01
42	2.52E+01
43	2.46E+01
44	2.37E+01
45	2.16E+01

46	2.01E+01
47	1.98E+01
48	1.78E+01
49	1.72E+01
50	1.60E+01
51	1.53E+01
52	1.42E+01
53	1.26E+01
54	1.21E+01
55	1.17E+01
56	1.11E+01
57	1.01E+01
58	1.10E+01
59	8.99E+00
60	5.84E+00
61	1.91E+00
62	6.61E-02
63	